Measurement of Single-Top Cross Section and Test of Anomalous Wtb Coupling

Ji-Eun Jung

Under the supervision of
Professor Soo-Bong Kim

A Dissertation submitted to the Graduate
Faculty of Seoul National University
in partial fulfillment of the requirement
for the Degree of Doctor of Philosiphy

Department of Physics and Astronomy
The Graduate School of Natural Science
Seoul National University
Seoul, Korea

February 2010

Abstract

The top quark is most often produced in $t\bar{t}$ pairs via the strong interaction, however electroweak production of a singly-produced top quark is also possible. Electroweak single-top production is more difficult to observe than $t\bar{t}$ production.

Studying single-top production is important for the following reasons. It provides direct measurement of the CKM matrix element and also single-top events are a background to several searches for SM or non-SM signals, such as Higgs boson searches. The information of spin polarization of top-quark can be used to test anomalous W-t-b coupling.

This thesis describes the result of a measurement of single-top cross-section and a test of anomalous W-t-b coupling using 4.8 f b^{-1} of data collected by the CDF Run II experiment at the Fermilab Tevatron.

The measured cross-section is $1.83^{+0.7}_{-0.6}$ pb and measured limit of $|V\mathrm{tb}|$ is 0.41 at 95% CL. The fraction of $V+\mathbf{A}$ coupling is 0 ± 28 (%).

Contents

i

ii

List of Figures

iii

iv

v

vi

List of Tables

vii

Chapter 1

Introduction

1.1 The Standard Model of Particle Physics

The particle physics treat the constituents of matter and the nature of the interaction between them. The Standard Model(SM) explains successfully the particles and their interactions in universe by gauge theories. There are four interaction forces of the weak nuclear force, the electromagnetic force, the strong nuclear force, and gravitation. The weak, electomagnetic and strong forces are combined in Standard Model theory, but the gravitation is not yet described by the SM.

One model of the particles is the spin 1/2 fermions, that is the quarks and leptons. There are 6 quarks of up(u) and down(d), charm(c) and strange(s), and top(t) and bottom(b), with fractional charge of $+\frac{2}{3}$e and $-\frac{1}{3}$e. The baryons are bound states of three quarks and the mesons are composed of a quark and an antiquark; the quarks don't exist as a free particle. There are three leptons(electron, muon and tau) with the charge of -1e and three neutrinos(no charge) associated with its leptons. Originally, neutrino mass is assumed massless by SM, but from the recent experimental result, the evidence that neutrino has non-zero mass is provided. The neutrino interact only through the weak force and the leptons interact additionally through the electromagnetic force.

The another model of particles is boson, which has integral spin. The interactions between particles can be occured as two particles exchange a boson.

The list of elementary particles in Standard Model is shown in Table 1.1.

The weak interaction is mediated by the bosons, charged $W^{\pm}$ boson or neutral Z^0 boson. The weak interactions are processed in short distances because the bosons are massive; the Ws have measured mass of $80.4 \text{GeV}/\text{c}^2$ and Z^0 has a measured mass of 91.2 GeV/c^2. The transition between quarks of different flavors can occur via the weak interaction. Cabibbo-Kobayashi-Maskawa(CKM) matrix

Fermions				Charge	Spin
Quarks	$\begin{pmatrix} u \\ d \end{pmatrix}$	$\begin{pmatrix} c \\ s \end{pmatrix}$	$\begin{pmatrix} t \\ b \end{pmatrix}$	$+\frac{2}{3}e$ $-\frac{1}{3}e$	$\frac{1}{2}$ $\frac{1}{2}$
Leptons	$\begin{pmatrix} e \\ \nu_e \end{pmatrix}$	$\begin{pmatrix} \mu \\ \nu_\mu \end{pmatrix}$	$\begin{pmatrix} \tau \\ \nu_\tau \end{pmatrix}$	$-1e$ 0	$\frac{1}{2}$ $\frac{1}{2}$
Gauge Bosons				Charge	Spin
γ (photon)				0	1
$W^\pm$, Z (weak boson)				± 1	1
g (gluon)				0	1

Table 1.1. Elementary Particles in Standard Model

represents the strenth of this transition of quarks.

The CKM matrix, 3×3 unitary matrix, is represented.

$$\begin{pmatrix} d' \\ s' \\ b' \end{pmatrix} / \begin{pmatrix} V_{ud} & V_{us} & V_{ub} \\ V_{cd} & V_{cs} & V_{cb} \\ V_{td} & V_{ts} & V_{lb} \end{pmatrix} \begin{pmatrix} d \\ s \\ b \end{pmatrix}$$

where V_{CKM} is obtained using the method of Refs. [54, 55].

$$\begin{pmatrix} 0.97419 \pm 0.00022 & 0.2257 \pm 0.0010 & 0.00359 \pm 0.00016 \\ 0.2256 \pm 0.0010 & 0.97334 \pm 0.00023 & 0.0415^{+0.0010}_{-0.0011} \\ 0.00874^{+0.00026}_{-0.00037} & 0.0407 \pm 0.0010 & 0.999133^{+0.000044}_{-0.000043} \end{pmatrix}$$

Quantum Electrodynamics describes the electromagnetic interaction among the quarks and leptons through the exchange of massless spin-1 photons. This electomagnetic force reach to the infinite range due to the massless photon. The electroweak theory is the unification of the electromagnetic and weak interaction in the Standard Model.

Quantum Chromo Dynamics(QCD) describes the strong interaction via gluon exchange. The spin-1 gluons is massless and carries color charge(R,G,B) affecting gluon self-interaction. The quarks also have the color charge and they are bound via the strong interaction forming colorless states(baryon or meson). From this feature, the strong force increases at large distance and decreases at short distances, which is asymptotic freedom.

2

1.2 Singly-produced Top Quark

In proton-antiproton($p\bar{p}$) collisions at 1.96 TeV, top quarks are predominantly produced in $t\bar{t}$ pairs via strong interaction processes. The top quark in top pair production was discovered in 1995 at the Tevatron. Singly-produced-top quarks are also expected via the electroweak interaction involving a Wtb vertex in the Standard Model (SM).

The single-top-quarks can be produced through three partonic processes. the s-channel production $q\bar{q}'^0 \to t\bar{b}$, called W* production, the t-channel production $qg \to t\bar{b}q^0$, called Wg-fusion, and associated production with a W boson $bg \to tW$. At the Tevatron the t-channel and s-channel process are dominant, while associated tW production is negligible (σ_s / 0.88 = 0.05 pb (s-channel), σ_t / 1.98 $\pm$ 0.08 pb (t-channel) in SM). Therefore, the s-channel and t-channel are only considered in this analysis. The leading-order(LO) and the next-to-reading order(NLO) Feynman diagrams for the single-top production channels are shown in Figure 1.1 and Figure 1.2 respectively.
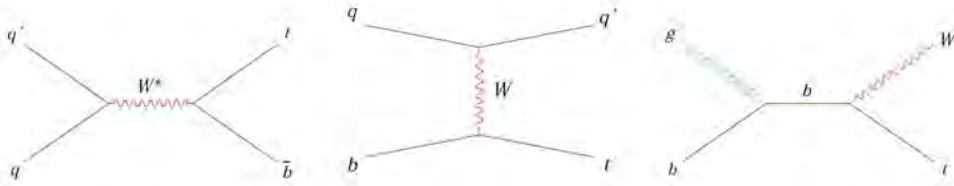
Figure 1.1. LO diagram for s-channel(left), t-channel(middle) and associated tW(right) single-top-quark production
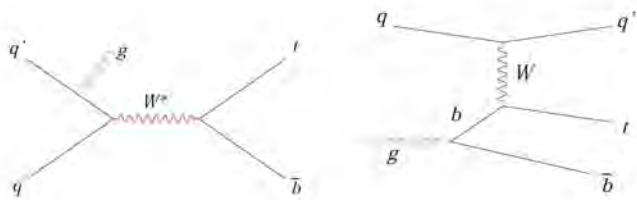
Figure 1.2. Examples of NLO diagrams for s-channel(left) and t-channel(right) single-top-quark production

3

Electroweak single-top-quark production via a Wtb vertex gives unique opportunity of the direct measurement of the CKM(Cabibbo-Kobayashi-Maskawa) matrix element $|V_{tb}|$. The cross section is proportional to the $|V_{tb}|^2$ and this value can be extracted from the measurement of single-top cross-section.

$|V_{tb}|$ characterizes the strength of transition of a top quark into a bottom quark when the two particles interact through the electroweak interaction. The quantity is currently not well measured and all previous results were under the assumption that the CKM matrix is unitary. In $t\bar{t}$ production (Fig. 1.3), the determination of $|V_{tb}|$ from top decays uses the ratio of braching fractions R / B(t → Wb)/B(t → Wq) / $|V_{tb}|^2/(\sum_q |V_{tq}|^2)$, where q / b, s, d. The CDF and D0 measurement performed on data collected during Run II of the Tevatron give $|V_{tb}| > 0.78$ [1] and $|V_{tb}| > 0.89$ [2]. For another examples, the result from top-loop contributions of ($\Gamma \to b\bar{b}$) is $|V_{tb}| / 0.77^{+0.18}_{-0.24}$ [3]. The Vertex diagram shown at the one-loop level in Fig. 1.4 which affects the Z partial width, $\Gamma_{b\bar{b}}$
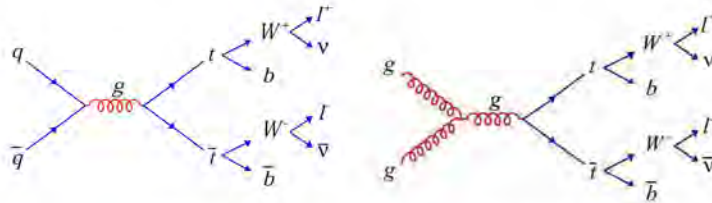
Figure 1.3. Top pair($t\bar{t}$) Production
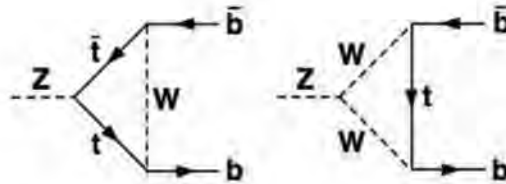
Figure 1.4. Vertex correction diagrams, at order of one-loop, which contribute to the partial width for $Z \to b\bar{b}$

Measuring the single top quark production cross section allows us to avoid the assumption of unitarity, to measure $|V_{tb}|$ precisely, and to draw conclusions about a hypothetical fourth generation of quarks. Studying the polarization in single top events will be a very important test of the weak interaction of the top

4

quark. Finally, measuring the single top process tests exotic models beyond the Standard Model, which predict anomalously altered single top producton rates like heavy right handed W' bosons, flavor changing neutral currents or large extra dimensions.

The CDF and D0 collaborations have sought single-top production for over a decade. Evidence of single-top production was published [8][9][10] and finally both collaborations observed single top production at the 5σ level of significance [6][7].

Table 1.2 shows expected cross section of single-top production at Tevatron(1.8 TeV (Run I), 1.96TeV (Run II)) and LHC(14 TeV).

Procerss	$\overset{\text{p}}{\underset{\text{S}}{\text{—}}}$	$\sigma_{LO}(\text{pb})$	$\sigma_{NLO}(\text{pb})$
s-channel	1.8 TeV pp̄ (t)	0.259	0.380 = 0.002
	1.96 TeV pp̄ (t)	0.304	0.447±0.002
	2 TeV pp̄ (t)	0.315	0.463±0.002
	14 TeV pp̄ (t)	4.53	6.55=0.03
	14 TeV pp̄ (t̄)	2.74	4.07=0.02
t-channel	1.8 TeV pp̄ (t)	0.648	0.702=0.003
	1.96 TeV pp̄ (t)	0.883	0.959±0.002
	2 TeV pp̄ (t)	0.948	1.029±0.004
	14 TeV pp̄ (t)	144.8	152.6 = 0.6
	14 TeV pp̄ (t)	83.4	90.0±0.5

Table 1.2. The cross section of single-top production at Tevatron and LHC

Figure 1.5 shows the graph of single-top cross section versus center of mass energy. The cross-section of both s-channel and t-channel are growing by increase of the center of mass energy. This is consistent with expectation that increase of initial energy corresponds to larger production cross section. The cross section of single-top production can be calculated as follows.

Consider the process $p_1 + p_2 \to p_3 + p_4$, where particle's momentum [4]. The partonic kinematical invariants are s / $(p_1 + p_2)^2$, t / $(p_1 - p_3)^2$, u / $(p_2 - p_3)^2$, s_4 / s+t+u−m_3−m_4. The hadronic kinematical invariants are S / $(p_{h1} + p_{h2})^2$, T / $(p_{h1} - p_3)^2$, U / $(p_{h2} - p_3)^2$, S_4 / S + T + U − m_3^2 − m_4^2, where h_1 and h_2 are the hadrons (protons and antiprotons at the Tevatron) corresponding to partons p_1 and p_2; thus, p_1 / $x_1 p_{h1}$ and p_2 / $x_2 p_{h2}$. The relations are as follows. s / $x_1 x_2 S$; t − m_3^2 / $x_1(T - m_3^2)$; u − m_3^2 / $x_2(U - m_3^2)$.

The hadron-level cross section σ is

$$\sigma \ / \ \int dx_1 dx_2 \phi(x_1)\phi(x_2)\hat{\sigma} \ /) \ \frac{d\sigma}{dTdU}$$

5
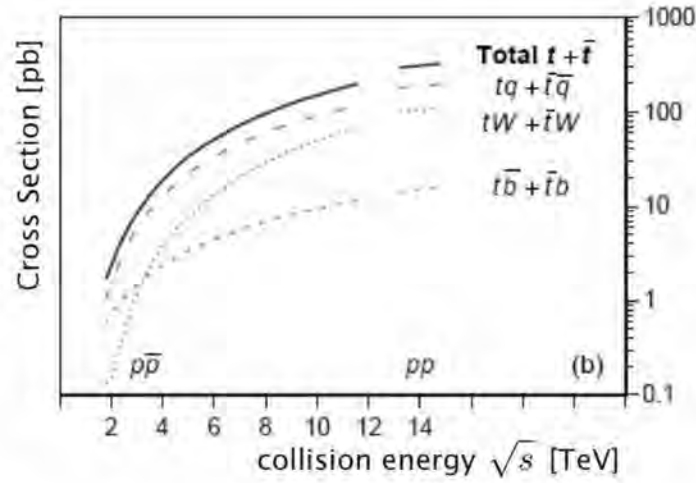
Figure 1.5. Single top quark cross section with center of mass energy

$$/ \quad \int dx_1 dx_2 \frac{dt}{dT}\frac{du}{dU}\phi(x_1)\phi(x_2)\frac{d\hat{\sigma}}{dtdu}$$

where $\hat{\sigma}$ is parton-level cross section, $\phi(x)$ is the parton distribution.
Now dt $/$ x_1dT and du $/$ x_2dU,

$$\frac{d\sigma}{dTdU} \quad / \quad \int dx_1 dx_2 x_1 x_2 \phi(x_1)\phi(x_2)\frac{d\hat{\sigma}}{dtdu} \; /) \quad \sigma$$

$$/ \quad \int dTdUdx_1 dx_2 ds_4 \frac{x_1 x_2}{x_2 S + T - m_3^2}\phi(x_1)\phi(x_2)\frac{d\bar{\sigma}}{dtdu}.$$

The Born-level differential partonic cross section is written as

$$\frac{d^2\hat{\sigma}_{p_1 p_2 \to p_3 p_4}^B}{dtdu} \; / \; F_{p_1 p_2 \to p_3 p_4}^B \delta(s_4) \; / \; \frac{|M_{p_1 p_2 p_3 p_4}|^2}{16\pi s^2}\delta(s_4).$$

For the t-channel process ub→ dt,

$$|M_{ub \to dt}|^2 \; / \; \frac{4\pi^2 \alpha^2 V_{tb}^2 V_{ud}^2}{\sin^4\theta_W}\frac{s(s - m_t^2)}{(t - m_W^2)^2}.$$

For the t-channel process d̄b → ūt,

$$|M_{\bar{d}b \to \bar{u}t}|^2 \; / \; \frac{4\phi^2 \alpha^2 V_{tb}^2 V_{ud}^2}{\sin^4\theta_W (t - m_W^2)^2}[(s + t)^2 - (s - t)m_t^2].$$

6

For the s-channel process $u\bar{d} \to \bar{b}t$,

$$|M_{u\bar{d} \to \bar{b}t}|^2 \ / \ \frac{4\pi^2\alpha^2 V_{tb}^2 V_{ud}^2}{\sin^4\theta_W} \frac{t(t - m_t^2)}{(s - m_W^2)^2}$$
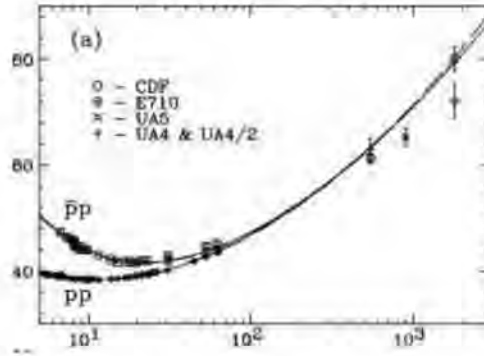
Figure 1.6. Cross section of pp and p$\bar{\text{p}}$

Suppose b quark content due to gluon spitting is enough large, the t-channel cross section is larger than s-channel. This is because the kinematic dependence of t-channel is $(s - m_t^2)/s(t - m_W^2)^2$ while kinematic dependence of s-channel is $t(t - m_t^2)/s^2(s - m_W^2)^2$. This means that t-channel is more kinematically probable than s-channel for large s. As small s, the b quark content in proton is much smaller than that of light quark, and thus the cross section of s-channel is larger. However, the b quark content becomes larger for high energy(i.e. larger s), and thus t-channel cross section becomes larger at high s.

1.3   A test of Anomalous Wtb Coupling

The electroweakly produced top quarks are nearly 100% polarized. The top quark decay width is much larger than Λ_{QCD} [14], so the top quarks remain polarized when they decay. The decay of top quark proceeds so rapidly that toponium bound states and T mesons do not have time to form, so the decay products of the top quark are correlated with its spin. On the other hand, the bound state mesons(or lighter quarks) such as the B^0 and the $B^\pm$ lost the information of their polarization due to spin-exchanging interactions with the spectator quarks and gluons.

7

The polarization fraction of singly-produced top quarks is expected to be modified if the top quark couplings to the SM $W^{\pm}$ are anomalous, if the production W has an admixture of an exotic W^0, if single-top quarks are produced in addition to the SM mechanisms by more exotic mechanisms [17] such as FCNC's [16], charged Higgs boson exchange instead of SM W exchange in the production channel.

The meausured cross-section of SM single-top production at CDF is $2.3^{+0.6}_{-0.5}$pb and this measured value is lower than the SM prediction of 2.864 ± 0.33 [25][26]. Then any fraction of the single top signal escaped our detecton may exist. Becuase in our analysis the input variables (decay angles and matrix elements and so on) are used to separate signal from background, top quarks produced with right-handed polarization would not look as signal-like as top quarks with left-handed polarization.

At this point, we focused to the anomalous Wtb coupling in single-top production. As it is mentioned before, single top production allow a direct measurement of the CKM matrix element $|V_{tb}|$. We can test the anomalous Wtb coupling by using angular correlations in the events due to the top spin correlation.

The matrix element for the electroweak process $u\bar{d} \rightarrow t\bar{b}$ via virtual W boson can be descriped as follows [11].

As the production of a spin up top quark,

$$|\mathrm{M}\,(0 \rightarrow \bar{\mathrm{u}}\mathrm{dt}_{\uparrow}\bar{\mathrm{b}})|^2 \;/\; \mathrm{g}_W^4 |V_{ud}|^2 \mathrm{N}_c^2 \frac{(2\mathrm{d} \cdot \mathbf{t}_2)(2\mathrm{u} \cdot \mathbf{b})}{(2\mathrm{u} \cdot \mathrm{d} - \mathrm{m}_W^2)^2 + (\mathrm{m}_W \Gamma_W)^2}. \tag{1.1}$$

As the production of a spin down top quark,

$$|\mathrm{M}\,(0 \rightarrow \bar{\mathrm{u}}\mathrm{dt}_{\downarrow}\bar{\mathrm{b}})|^2 \;/\; \mathrm{g}_W^4 |V_{ud}|^2 \mathrm{N}_c^2 \frac{(2\mathrm{d} \cdot \mathbf{t}_1)(2\mathrm{u} \cdot \mathbf{b})}{(2\mathrm{u} \cdot \mathrm{d} - \mathrm{m}_W^2)^2 + (\mathrm{m}_W \Gamma_W)^2} \tag{1.2}$$

where top quark momentum is decomposed into a sum of two massless auxiliary momenta, $\mathbf{t}_1 \equiv \frac{1}{2}(\mathbf{t} + \mathrm{m}_t\mathbf{s})$, $\mathbf{t}_2 \equiv \frac{1}{2}(\mathbf{t} - \mathrm{m}_t\mathbf{s})$ (s is spin vector of the top quark) and g_W is the weak coupling constant, m_W and Γ_W are mass and width of the W boson, N_c is the number of colors. As those equations, the top quark produced via the W^* process are 100% polarized along the direction of the d-type quark, since (1.2) vanishes if we choose $\mathbf{t}_1 \;/\;$ d.

At Wg fusion process, the matrix element for the production of spin down top quarks in the basis where the spin axis coincides with the d quark direction.

$$|\mathrm{M}\,(0 \rightarrow \bar{\mathrm{u}}\mathrm{dgt}\bar{\mathrm{b}})|^2 \;/\; \frac{\mathrm{g}_W^4 \mathrm{g}_s^2 |V_{ud}|^2 \mathrm{N}_c(\mathrm{N}_c^2 - 1)}{(2\mathrm{u} \cdot \mathrm{d} - \mathrm{m}_W^2)^2} \frac{\mathrm{m}_t^2(\mathrm{g} \cdot \mathrm{d})^2}{(\mathbf{t} \cdot \mathrm{g})^2} \left| \frac{\mathrm{u} \cdot \mathrm{b}}{\mathbf{t} \cdot \mathrm{d}} \right|.$$

In $p\bar{p}$ colllision at the Tevatron with $\sqrt{\mathrm{s}}$/ 2.0 TeV, the antiproton beam supplies the d-type quark 98% of the time at W^* production. At W-gluon fusion process,

8

d-type quark is either contained in one of the beams or in the spectator jet. In fact, spectator jet is the d quark 77% of the time [12]. The summary of the fractional cross section is shown in Table 1.3 for W* process and Table 1.4 for Wg-fusion process. Figure 1.7 shows spin configuration of top decay products.

p	$\bar{p}$	Fraction
u	d	98%
$\bar{d}$	u	2%

Table 1.3. The fractional cross section for single top production in the W* channel at the Tevatron with center of mass energy $\sqrt{s}$/ 2.0 TeV

p	$\bar{p}$	Fraction
u	g	74%
g	u	3%
g	$\bar{d}$	20%
$\bar{d}$	g	3%

Table 1.4. The fractional cross section for single top production in the Wg-fusion channel at the Tevatron with center of mass energy $\sqrt{s}$/ 2.0 TeV

In the limit of a massless b quark, b-quark decayed left-handedly . Also, W decay configuration is shown in Figure 1.8. The massless neutrio is left-handedly decayed, and then lepton is decayed backward in the left-handed W decay and goes to the opposite direction in the right-handed W decay to conserve angular momentum. Therefore, decayed lepton momentum is correlated to the direction of top spin(or d-type quark). The decay angular distributions are linear of decay angles (Fig. 1.9) with top spin vector in top quark rest frame [12].

$$\frac{1}{\Gamma}\frac{d\Gamma}{d(cos\theta_i)} / \frac{1}{2}(1 + \alpha_i cos\theta_i).$$

where θ_i is the decay angle of the ith decay product (lepton, neutrino or b-quark) and the degree of correlation between decay product and the spin is represnented as α_i. So, the these angle distribution are shown in 1.10. By using this top polarization, we test anomalous Wtb coupling and for this analysis, generate Monte Carlo with changing V-$\mathbf{A}$ to V+$\mathbf{A}$ coupling at the production W's vertices (called SM single top sample is V-$\mathbf{A}$(LLLL), and non-SM(exotic) samle is V+$\mathbf{A}$(RRLL); details in chapter 7). The fitted values are σ/ 1.43 pb in V-$\mathbf{A}$(LLLL) and σ/ 0.0 pb in V+$\mathbf{A}$(RRLL). Finally, the measured fraction of V+$\mathbf{A}$ coupling is 0 ± 28 %.

9
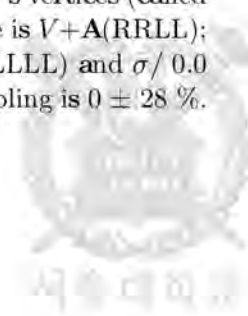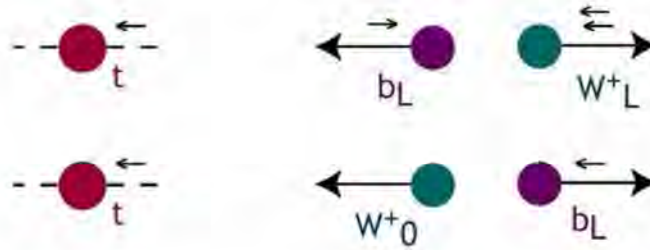
Figure 1.7. Allowed spin configuration for the top decay products in the limit of a massless b quark and each cases are left-handed(negative helicity) and longitudinal(zero helicity) W boson; small arrows represent each spin of top and bottom quarks and W boson.
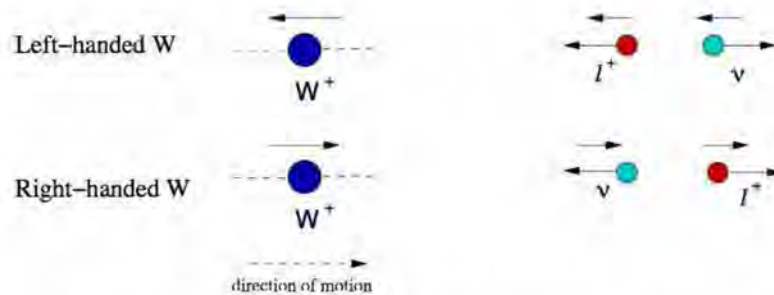
Figure 1.8. W^+ decay for left-handed and right-handed helicity. The charged lepton is decayed backward in the left-handed case and forward in the right-handed case due to angular momentum conservation.

10
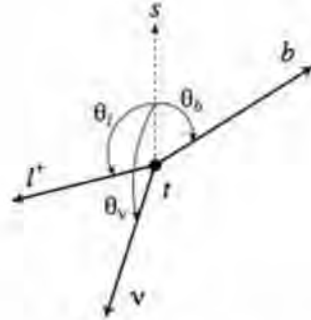
Figure 1.9. The decay angles of lepton, neutrino and b quark in the top quark rest frame. The vector s is the direction of top quark spin.
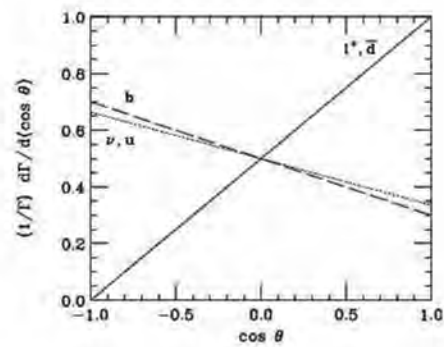
Figure 1.10. Angular correlations between the decayed particles and top quark spin vector in the decay of a spin up top quark.

11

Chapter 2

Experimental Apparatus

2.1 Accelerator

At Tevatron, proton and anti-proton collisions started at the center of mass energy $\sqrt{s}$ / 1.8TeV from 1985. The collected data from 1988 to 1996 (Run I) was 130 pb^{-1} and instantaneous luminosity was 10^{31}cm^{-2}sec^{-1}. During this period, there was the discovery of top quark in 1995. From 1996, the upgrade of the accelerator was performed to increase the center of mass energy and the instantaneous luminosity. From 2001, Run II phase started at $\sqrt{s}$ / 1.96TeV and instantaneous luminosity is about 10^{32}cm^{-2}sec^{-1}. Comparing to the Run I, the cross section of $t\bar{t}$ increased by 30~40 % in Run II.

The accelerator is separated into several steps that is preparing the proton source, producing anti-proton source, the acceleration of both protons and antiprotons to the center of mass energy 1.96TeV, and the collisions at CDF and D0.

The schematic view of the accelerator is shown in Figure 2.1.

Proton Source

The Cocksoft-Walton electrostatic Preaccelerator containing hydrogen atoms produces H$^-$-ions(hydrogen consists of a proton and an electron). H$^-$-ions are subsequently accelerated to an energy of 750 keV by the difference of the electrostatic potentail and passed through a transfer line of focusing magnets to the Linear Accelerator(Linac) where the linear RF acceleration to an energy of 400 MeV occurs. After that, the electron in a H$^-$-ion is stipped passing through a carbon foil leaving a proton and the separated protons are accelerated from 400 MeV to 8 GeV in the Booster.

Main Injector

The protons at 8 GeV are injected into the Main Injector, which has a sheared over shape and has two fold symmetry, and are accelerated to 120 GeV for fixed target operation or 150 GeV for injection into the Tevatron.

12
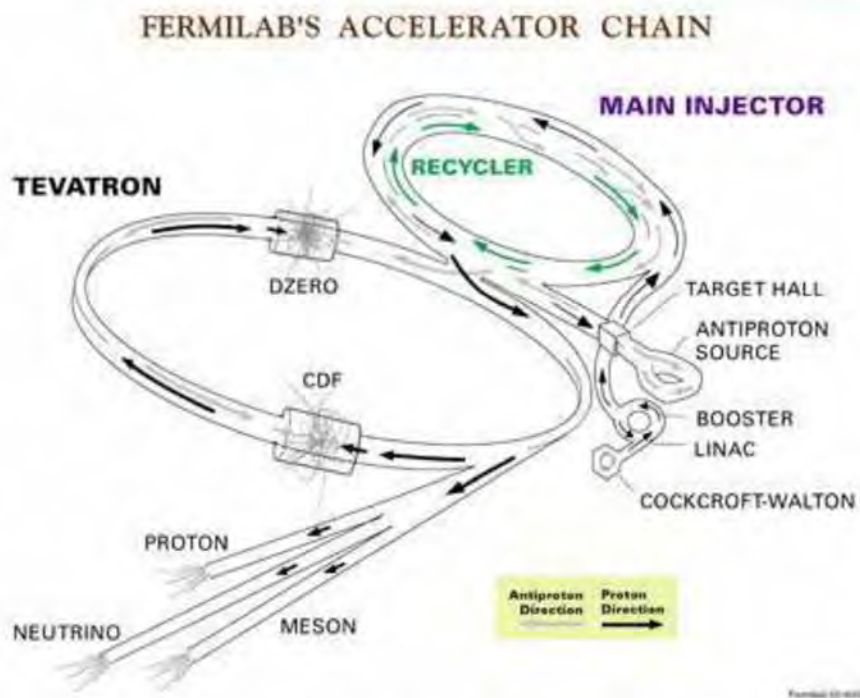
Figure 2.1. Schematic overview of the Fermilab accelerator chain.

Anti-proton Source

A beam of 120 GeV protons from Main In|ector is smashed on to a stack of nickel targets and copper cooling disks. The antiprotons coming out of the target at many different angles are focused into a beam line with a Lithium lens and then separated from many different particles through a pulsed magnet. A very large spread in energy of these antiprotons can change into the narrow energy spread by Debuncher accelerator. Additionally, the Debuncher maintains a stable antiproton beam at the energy of 8 GeV. Stochastic cooling systems achieves the beam stabilization by removing a wide range of energies, positions and angles of the antiprotons. The antiprotons remain in the Debuncher for about 2 sec until the next bunch of protons come and are sent to the Accumulator where the antiprotons are stacked at an energy of 8 GeV and further cooled down. When the antiproton in the Accumulator reaches the maximum optimal capacity, the bunches are trasferred back to the Main In|ector and in|ected into the Recycler.

Recycler

The Recycler is a fixed 8 GeV kinetic energy storage ring and is located in the Main In|ector tunnel directly above the Main In|ector beamline. The Recycler sing provides long-term stash for antiprotons by acting as a high reliability post-Accumulator and receptacle for recycled antiprotons from previous store. The further cooling of antiproton source occured using stochastic cooling and electron cooling in the Recycler.

Tevatron

Finally, the protons and antiprotons are sent to the Tevatron, which is a circular synchrotron with a diameter of about 2 km. The 36 proton and 36 antiproton bunches are accelerated to the center of mass energy $\sqrt{s}$ / 1.96 TeV. The collisions of focused proton and antiproton beam occure at CDF and B0.

2.2 Detector: Upgrade of RunII Detector

The CDF II detector, upgraded CDF detector from Run I in 1992 - 1995 period, is an azimuthal and forward-backward symmetric apparatus designed to study p$\bar{\text{p}}$ collisions at the Tevatron.

Figure 2.2 shows the detector.

Tracking System

The Tracking system consists of a silicon micro-strip detector and an open-cell wire drift chamber that surrounds the silicon detector. When a charged particle passed through the tracking system it ionizes the material/gas around it. A dedicated tracking algorithm searches for a continuous pattern of localized charge depositions (hits) and reconstructs the path of the charged particle, called the

14
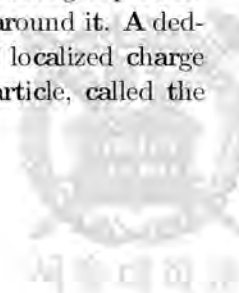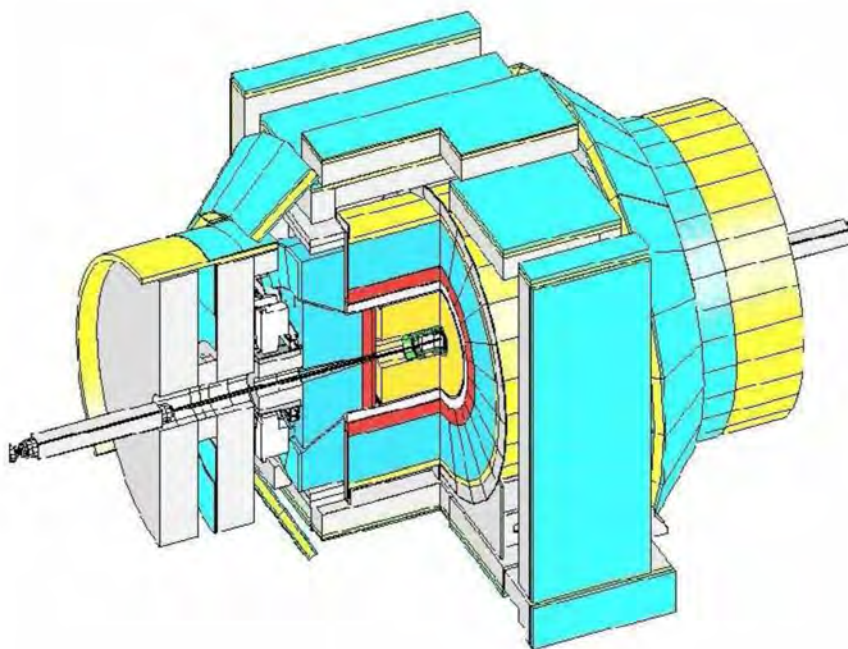
Figure 2.2. The CDF Run II Detector

particle's 'track'. The longitudinal view of the CDF II tracking system is shown in Figure 2.3

CDF Tracking Volume
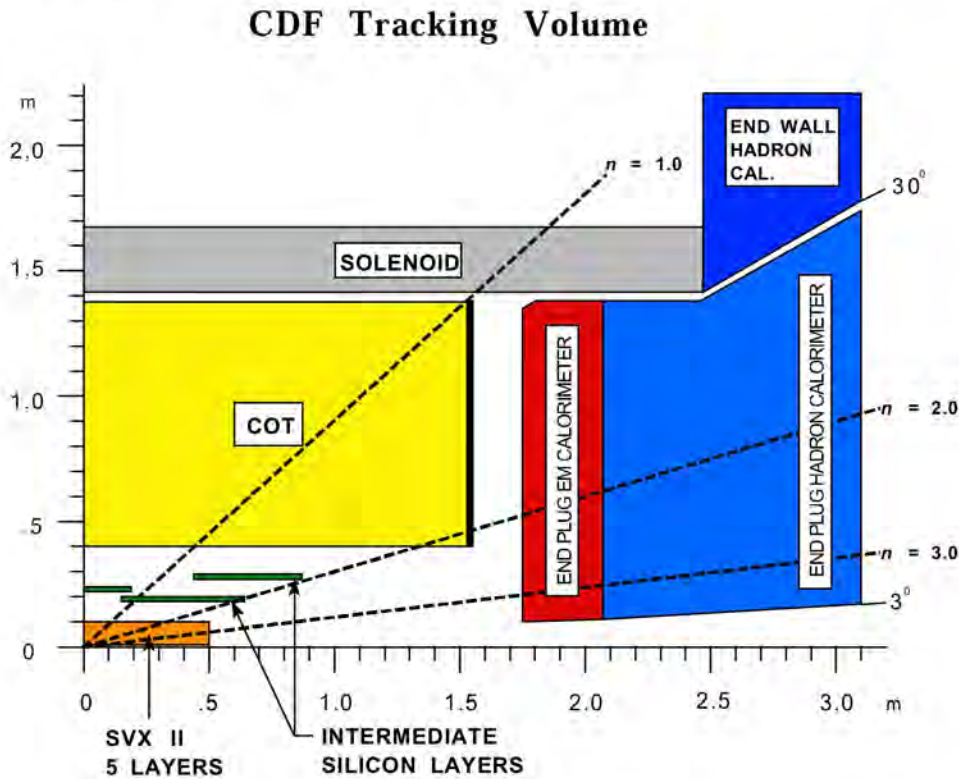
Figure 2.3. Longitudinal View of the CDF II Tracking System

The silicon micro-strip detector consists of three sub-detectors shown in Figure 2.4

The first is the Layer00 detector. This is a layer of radiation hard silicon wafers which is directly mounted around the beam pipe.

To detect secondary vertices from heavy flavor particle decays such as bottom and charm hadrons and to give an excellent tools for b-tagging, Silicon Vertex Detector(SVX) was added to CDF in 1992 for second sub-system. This detetor was replaced with SVX^0 to control radiation damage using AC-coupled detectors and a radiation hard readout chip. For increasing the number of p and $\bar{p}$ bunches, SVX^0 detector was substituted for SVX II (Run II Silicon Vertex Detector) which is designed to permit good resolution in locating the z-position of secondary vertices and to enhance the 3-D pattern recognition capability of the

16
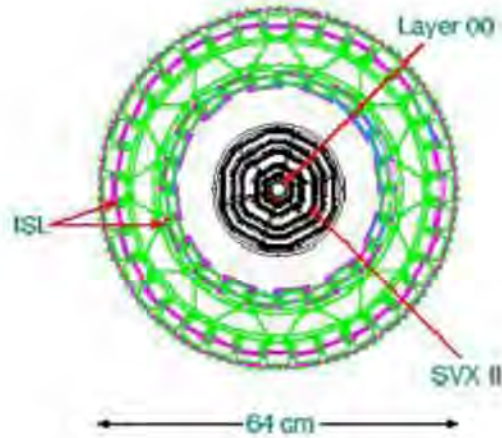
Figure 2.4. Silicon micro-strip detector consists of Layer 00, SVX II and ISL.

tracker. This detector has three barrels(Fig. 2.5), each 29 cm long. There are 12 wedges in ϕ, each with five layers of silicon; three have 0°-90° stereo and two have 1.2 ° small-angle stereo. Some mechanical properties are given in Table 2.1. For each barrel, the silicon ladders are mounted between two precision-machined beryllium bulkheads(Fig.2.6) which also carry the water cooling channels for the readout electronics.

For $|\eta| > 1$, SVX II can only perform 2D tracking and impact parameter resolution for such tracks will be too poor to enable efficient b tagging. These problems are addressed by the Intermediate Silicon Layers(ISL). In the central region, a single layer of silicon is placed at a radius of 22 cm and the region. $1.0 \leq |\eta| \leq 2.0$, two layers of silicon are placed at radii of 20 cm and 28 cm. Thus, ISL extends tracking, lepton indentification, and b-tagging capabilities over the full region $|\eta| \leq 2.0$

The new open-cell drift chamber, referred to as Central Outer Tracker (COT), is located directly outside of the silicon tracking detectors in the radial direction. The chamber consists of eight-layers (SL) of 310 cm length cells and radii between 40 and 132 cm from the beam axis. The COT is designed to operate with a maximum drift of 100 nsec by using a gas mixture containing 50.35.15 Ar-Et-CF$_4$. drift velocity is ∼100 μm/ns which implies a maximum drift distance of ∼1 cm. In Run II, to improve the robustness of the COT superlayers each consist of 12 sense wires, |ust like the axial layers. At CTC(Run I), The electrostatics of a cell is shaped by field wires whose potential varies to account for the tapered shape of the cell. In the COT(Run II), the field wires are replaced by as cathode "field

17

Figure 2.5. The SVX II 3 barrels

Property	Layer0	Layer1	Layer2	Layer3	Layer4
number of ϕ strips	256	384	640	768	896
number of Z strips	256	576	640	512	896
number of ϕ chips	2	3	5	6	7
number of Z chips	2	3	5	4	7
stereo angle	90°	90°	+1.2°	90°	-1.2°
ϕ strip pitch (μm)	60	62	60	60	65
Z strip pitch (μm)	141	125.5	60	141	65
total width (mm)	17.140	25.594	40.300	47.860	60.170
total length (mm)	74.3	74.3	74.3	74.3	74.3
active width (mm)	15.300	23.746	38.340	46.020	58.175
active length (mm)	72.43	72.43	72.38	72.43	72.38
number of detectors	144	144	144	144	144

Table 2.1. Silicon detector mechanical dimensions

18
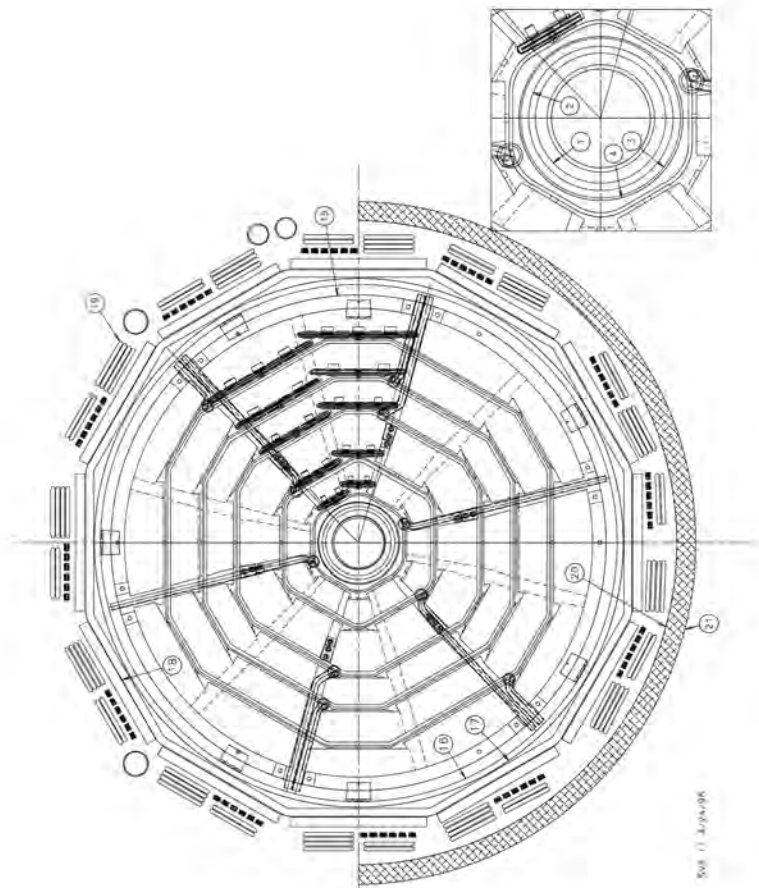
Figure 2.6. The SVX II bulkhead design

19

panel" which is gold on a 0.25 mil thick Mylar sheet. The ends of each cell are closed, both mechanically and electrostatically, by Mylar strips with field-shaping wires attached. these are referred to as "shaper pannels". Between the field panels, sense wires alternate with potential wires in a plane. The 1.6 mil gold-plated tungsten is used for both wires. Figure 2.7 illustrates the cell geometry using SL2 as an example.
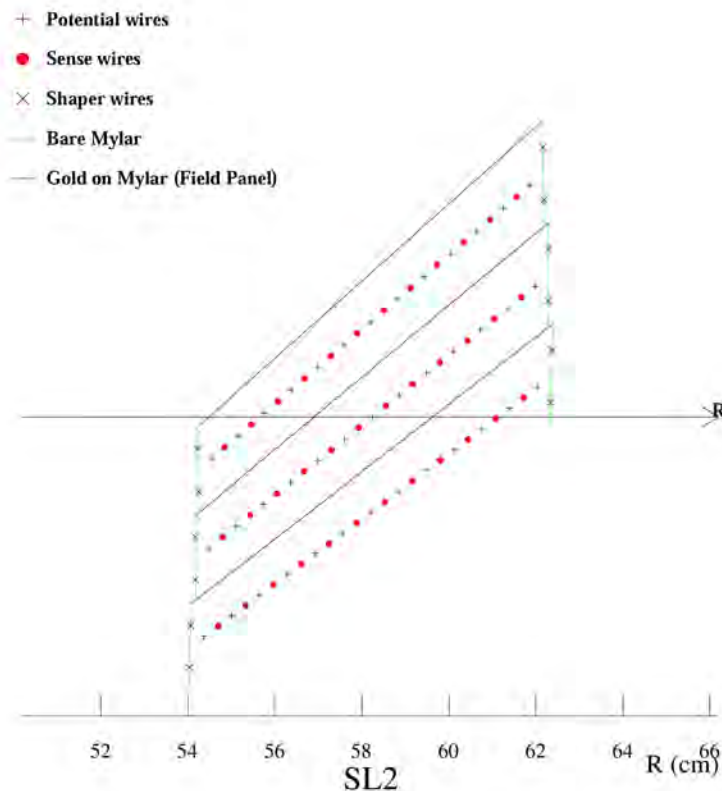
Figure 2.7. Nominal cell layout for SL2.

The charge and momentum of a particle-track are determined by measuring the curvature of the track in the magnetic field. The solenoid produces a 1.4T magnetic field inside the tracking volume that is uniform to 0.1% in the acceptance region. The transverse momentum of a reconstructed track is determined from P_T / Bqr, where B is the strength of the magnetic field, q is the charge of the

20
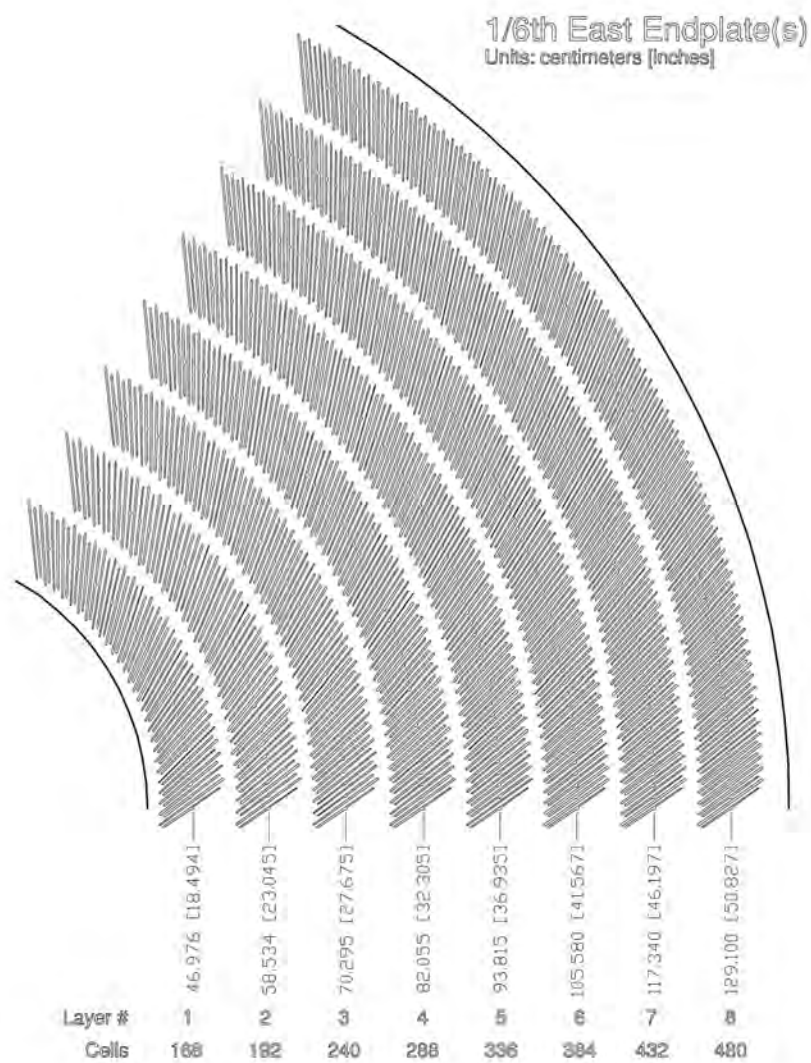
Figure 2.8. East endplate slots. Sense and field planes are at the clock-wise edge of each slot.

21

Number of Layers	96
Number of Superlayers	8
Stereo Angle	+3.0 -3.0 +3.0 -3.0°
Cells/Layer	168 192 240 288 336 384 432 480
Sense wires/Cell	12 12 12 12 12 12 12 12
Radius at Center of SL	46 58 70 82 94 106 119 131cm
Sense wire Spacing	0.3^{0}(7.62 mm) in plane of wires
Wire Diamter	1.6 mil gold plated Tungsten
Wire tension	135 g
Tilt Angle	35°
Length of Active Region	310 cm
Total number of Wires	63000
Endplate Load	~ 40 metric tons
Drift Field	2.5-3 kV/cm (depending on gas)

Table 2.2. COT Mechanical Summary

particle and **r** is the measured radius of curvature. The momentum resolution of the COT is given by $\sigma_{Pt}/\mathrm{P}_T^2$ / 1.7×10^{-3} | GeV/**c** $|^{-1}$

Calorimeter System

The CDF calorimeter is a scintillator sampling system measuring the energy of particles produced in the $p\bar{p}$ collision. The calorimeter is located behind the tracking volume and consists of layers of active (scintillator) material sandwiched between sheets of absorbing material such as lead and steel. As particles pass through the calorimeter, they interact with the layers. The photons produced in the scintillator layers and directly go to the photomultiplier by the plexiglass guides. Figure 2.9 shows the calorimeters in both central and plug region.

The central region which extends to a pseudorapidity($|\eta|$) of about 1 is spanned by CEM (lead(1/8 inch)-scintillator(5 mm polystyrene) Electro-Magnetic calorimeter) followed by CHA (iron (2.5 mm) - scintillator (1cm PMMA) hadron calorimeter). Both calorimeters have the basic stucture of 15° wedges which are subdivided in 10 projective towers. EM calorimeter has provided effective indentification of electrons and photons. Hadrons(strongly interactina particles), on the other hand, shower over longer distances in the calorimeter and deposit the most significant fraction of their associated energy in the hadronic section of the calorimeter.

CEM light-output is $\sim$100 photoelectrons per GeV per PMT and design energy resolution σ(E)/E for electrons is 13.5%/$\sqrt{E sin\theta}$.

22

CHA has good resolution($33\%/^p\overline{E sin\theta}$ with a 4 % constant term) for 50 GeV pions but there's the limitted thickness due to financial and structural limitations. The WHA(Wall Hadron Calorimeter) is in $|\eta|$-range $\sim$1.1 complementing CHA. This detector is also an iron(5 cm)-scintillator(1cm PMMA) but the sampling fraction is smaller than for the CHA because higher forward energies require more absorber and its resolution is worse.

The forward plug calorimeter has been upgraded for Run II. . The original gas calorimeter was replaced with scintillator plate calorimetry using scintillator tiles readout by wavelength shifting fibers embedded in the scintillator. Both the new plug electromagnetic calorimeter (PEM) and the new plug hadronic calorimeter (PHA) use the same polystyrene based scintillator and photomultiplier tubes used in the CEM. The PEM contains 23 layers of 0.45 cm of lead interleaved with 4.0 mm of scintillator while the PHA is made of 23 layers of 2.5 cm steel interleaved with 1.0cm of scintillator. These calorimeters span the range $1.1\leq |\eta| \leq 3.64$. Detector performance is $16\%/^p\overline{E}+1\%$ for the PEM with 5 p.e./minimally-ionizing particle(mip)/tile corresponding to a total light output of 400 p.e./GeV. For the PHA, is is $70\%/^p\overline{E}+4\%$ with 5 p.e./mip/tile correspoding to a total light output of 40 p.e./GeV Figure 2.10 shows the cross-section of end plug calorimeter.

Muon System

The muon detectors are located behind the calorimeter modules. Muons typically pass through the calorimeter modules leaving only a small fraction of their energy in the calorimeter. The muon system consists of four independent system of proportional wire chambers, filled with a 50.50 of argon and ethane, and scintillators.The Central Muon detector(CMU) and the Central Muon Upgrade(CMP) both cover $0 <| \eta |< 0.6$; the Central Muon extension (CMX) which covers $0.6 <| \eta |< 1.0$; and the Barrel Muon Upgrade Detector (BMU) which covers $1.0 <| \eta |< 1.5$.

The CMU consists of four layers of drift chamber and can detect muons with a transverse momentum $p_T \geq 1.4$ GeV/c The CMP consists of four layers of wire drift chamber of identical design to the CMU, but they are staggered by half cell per layer. The chambers are located behind 60 cm of steel and form a rectangular box around the central detector. The CMP is mainly used in combination with the CMU detector to improve the purity in muon identification and the combined system is called CMUP. The Central Scintillator Upgrade (CSP) is located on top or the outermost layer of the CMP. The CSP consists of a single layer of scintillator plates to provide additional timing information.

The CMX is a conial arrangement of drift chambers similar to those of the CMP. Different to the CMU and CMP, this detector consists of eight layers of rectangular chambers which are grouped in pairs to form four continuous layers.
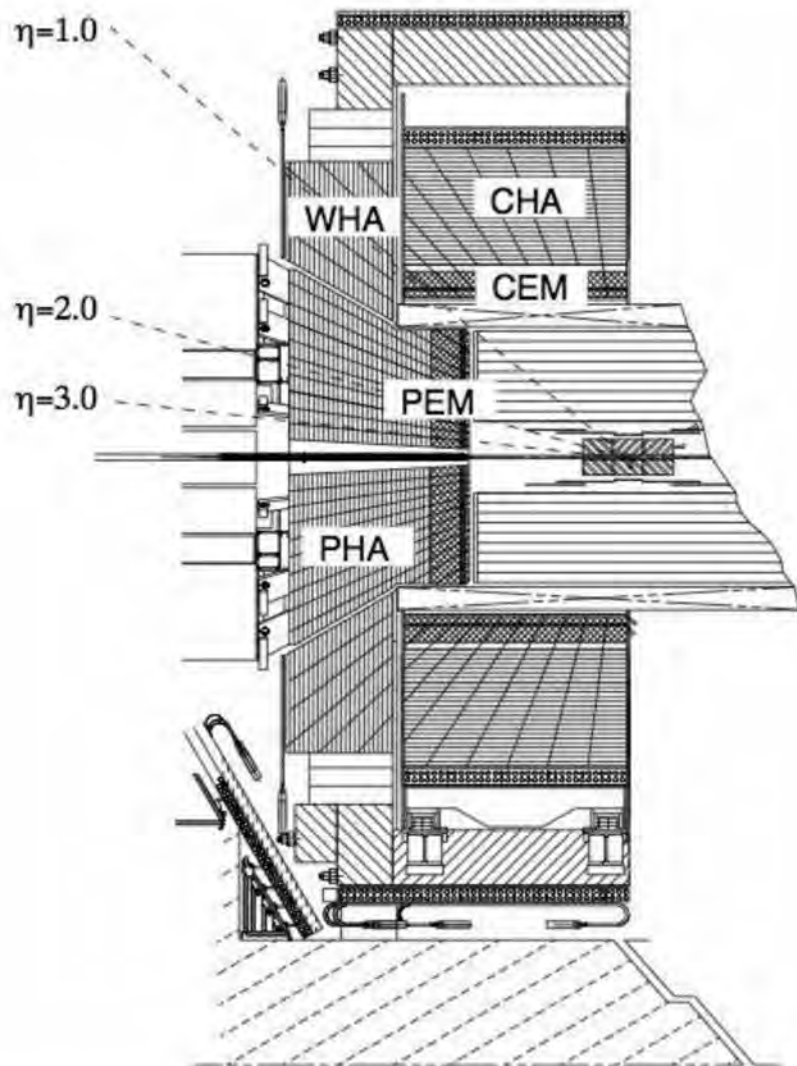
Figure 2.9. Calorimeter at CDF. CEM, CHA (central region $|\eta| < 1.0$, plug region. PHA, PEM, WHA)
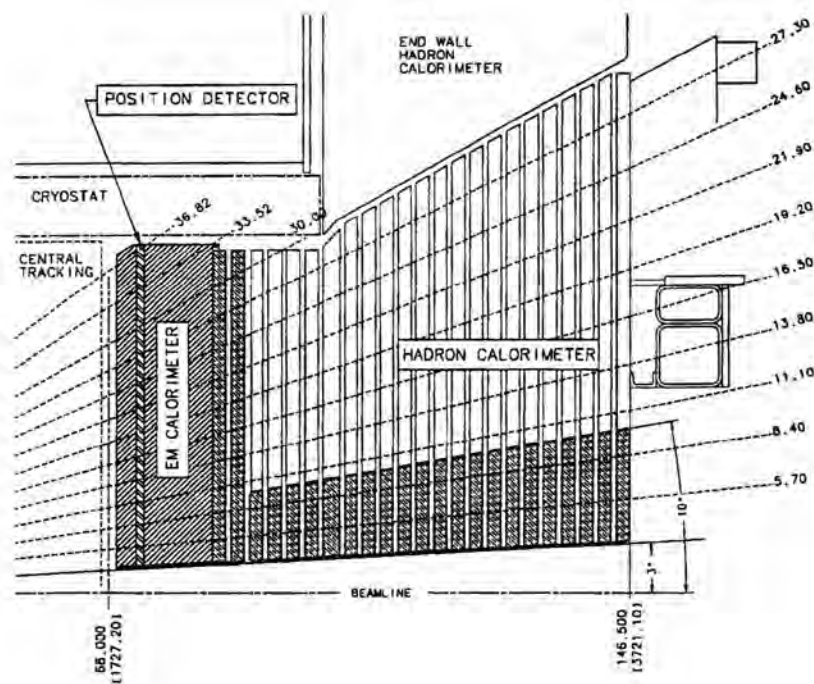
Figure 2.10. Cross section of upper part of new end plug calorimeter

25

The Central Muon Extension (CSX) are mounted on both sides of the CMX system which is used in coincidence with the wire chambers to further improve the timing of the system and reduce the fake rate such as beam splashes.

The BMU and BSU(Barrel Scintillator Upgrade) provides momentum and timing measurement. Those detectors are installed on top of the forward toroid barrels. At η-ϕ plane, the geometrical coverage of the muon chamber is shown in 2.11.
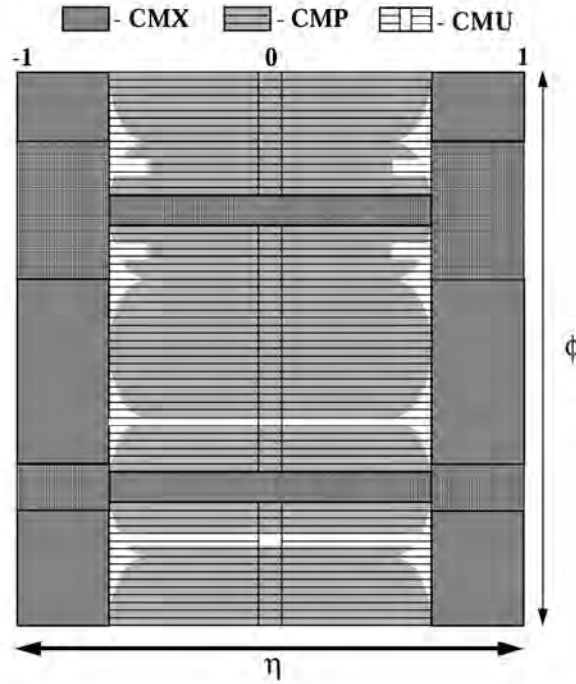
Figure 2.11. Geometrical Coverage of the Muon Chambers in η-ϕ plane

2.3   Trigger and Data Acquisition

The trigger is important system for accepting events because the collision rate is much higher than the rate at which data can be stored on tape. The interesting physices events need to be extracted from the large number of minimum bias events. The entire trigger system used in Run I is replaced for Run II because

26

the accelerator and detector upgrade. The main reason for replacing the trigger electonics is the reduction of the accelerator bunch spacing from 3.5μsec to 132-396nsec. The CDF trigger system is composed of three level constituents which is Level 1, Level 2, Level 3.

The first level of the tigger(Level 1) has to be the fastest and uses custom hardware to select events based on information from the calorimeters, tracking chamber(COT) and muon detectors. All detector data are fed into a 6 μs pipeline to provide time for processing required at Level-1. The eXtremly Fast Trigger(XFT) reconstructs tracks in the transverse plane of the COT. The XTRP then matches the tracks to electromagnetic calorimeter energy clusters or track segments in the muon systems. The acceptance rate of Level 1 is about 30 KHz.

The Level 2 trigger used custom hardware to do a limited event reconstruction. Processing of Level 2 trigger starts after the event is written into one of the four Level 2 buffers on all front-end and trigger modules by a Level 1 accept. The buffer cannot be used for additional Level 1 accepts during analyzing data at Level 2. This trigger level get the information from the SVX and CES(central shower-max detector). The CES(shower maximum detector) designed to improve identification of electrons and photons. The electron and photon trigger hardware is upgraded for RUN II using the information from the central shower maximum detector(CES). This upgrade made 50% reduction of backgrounds for electron. The Silicon Vertex Tracker(SVT) enables to increase the physics reach using impact parameter informatin to detect secondary vertices. The acceptance rate of Level 2 is about 300-1000 Hz.

The Level 3 trigger uses the full detector resolutions to fully reconstruct events in a processor farm. The developments aim for the reduction of event size to increase the Level 3 accept rate. After passing Level 3, the events are sent to the permanet storage at a rate of about 75-100 Hz. The dataflow of trigger system is shown in Figure 2.12.

2.4   Offline Data Reconstruction

Monitering and Finding of Beam Position

The beamline calibration is one of works of the offline group. The position of the beamline is an important input for many physics analyses such as event reconstruction for missing Et. Fitting beam position is performed by using track information of SVX and COT.After fitting the beamline, the fitting results (beamx, beamy, slopex, slopey, etc.) are stored in Data Base by each run. The fitted results can be used to monitering of tracking detector performance. The tracking alignment can be checked from comparing beam position of SVX and COT.

We used two algorithms for fitting beamlines. The first algorithm is based on

27

Dataflow of CDF "Deadtimeless" Trigger and DAQ

Detector — 7.6 MHz Crossing rate, 132 ns clock cycle

L1 Storage Pipeline: 42 Clock Cycles Deep

L1 trigger

Level1: 7.6 MHz Synchronous pipeline, 5544ns latency, <50 kHz Accept rate

L1 Accept

L2 Buffers: 4 Events

L2 trigger

Level 2: Asynchronous 2 stage pipeline, ~20μs latency, 300 Hz Accept Rate

L2 Accept

L1+L2 rejection: 20,000:1

DAQ Buffers

L3 Farm

Mass Storage

PJW 10/28/96

Figure 2.12. Fundamental block diagram of the CDF II data flow

28

the reconstruction of the primary vertex for each event using tracks. The second algorithm is based directly on tracks using the correlation of the d_0 and the ϕ_0 parameter of a track. The detailed description and fitted results for each run is in Appendix **A**. The explanation about the fitting algorithm is described in **A**.1 and the plots for beam position about svx and cot for each run are shown in **A**.2.

The |ob of fitting beam position is performed three times a day by cron |ob. The cron |ob runs main script(auto$V$alidate.pl) and check if the runs are already fitted runs in good-run list.

If all runs are valid within certain run range(processed runs in good run list), the information of beam about those runs is stored in Data Base. The values of x-position and y-position, slope in xz and yz plane and beam width and so on are stored in Data Base.

29

Chapter 3

Monte Carlo Simulation

3.1 Signal: s-channel, t-channel

The single-top signal events are produced with MADEVENT and PYTHIA. MADEVENT is a tree-level generator which is powered by the matirx element generator MADGRAPH. The amplitudes and event for each process are generated by MADEVENT. Because MADEVENT is designed to produce events at parton level, it interfaces with PYTHIA for showering and hadronization of events. The PYTHIA is a multi-particle production generator such as hard and soft interactions, parton distributions, initial and final-state parton showers, multiple interactions, fragmentation and decay.

s-channel Single Top-Quark Production

In s-channel single-top production, NLO distributions are the same as the LO distributions multiplied only by a constant correction. ZTOP software package provides NLO s-channel and t-channel single top-quark production distribution within the geometrical acceptance of a given detector. The ZTOP software calculates, that at least one jet(apart from the 1st b-quark jet coming from the top-quark decay) should be visible within the detectors acceptance in about 90% of all s-channel events. In most events, this p_T-leading jet is a b quark from the top decay. In MADEVENT, it is represented by a 2nd b quark at parton level. Only in about 10% ZTOP expects a light quark jet, which could come from hard initail or final-state gluon radiation and initail-state gluon splitting. Since the s-channel MADEVNET sample is LO and does therefore not include matrix elements with real gluon corrections modeled by the PYTHIA showering.

30

t-channel Simulation Matching Procedure

The PYTHIA generates too soft and too far forward distributed 2nd b quarks. Because PYTHIA starts with the LO 2→2 diagram, that is with a b-quark PDF and then creates the initial state using backward evolution(DGLAP). In LO process, soft region of the transverse momentum is well modeled, but the hard region is underestimated. The 2→3 NLO processes are generated with the initial state gluon splitting into a b$\bar{\text{b}}$ for hard region. Therefore, we need to match those two samples of 2→2 LO and 2→3 NLO. A joint event sample is created by matching the p_T spectrum of the 2nd b quarks in the matched t-channel sample consists of 2→2 events for transverse momenta below a certain cutoff K_T and of 2→3 events for transverse momenta above K_T. The ratio R between the two processes are varied until the rate of events with a detectable 2nd b quark jet, that is $p_T >$ 20 GeV/c, of the joint t-channel sample are simulated using 2→3 sample. The Figure 3.1 shows the 2nd b-quark Pt distributions of LO and NLO events.
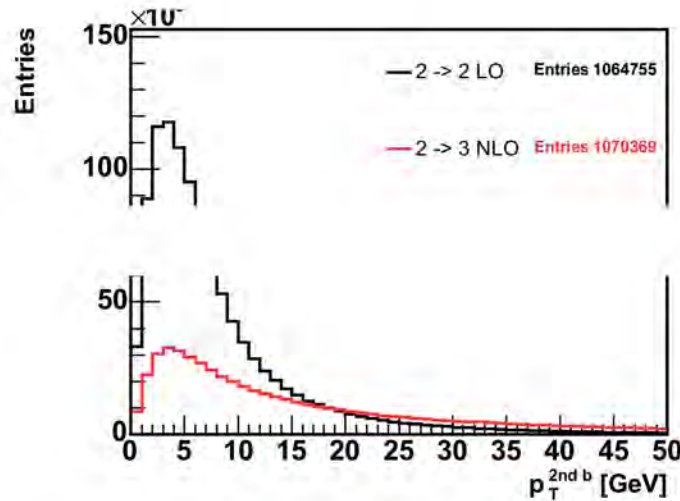
Figure 3.1. 2nd b-quark Pt distributions of LO and NLO

31

The Figure 3.2 shows the 2nd b-quark Pt distributions of LO and NLO events in log scale.

Finally, obtained value of K_T is 18 GeV for single-top t-channel(stopm0) sample.
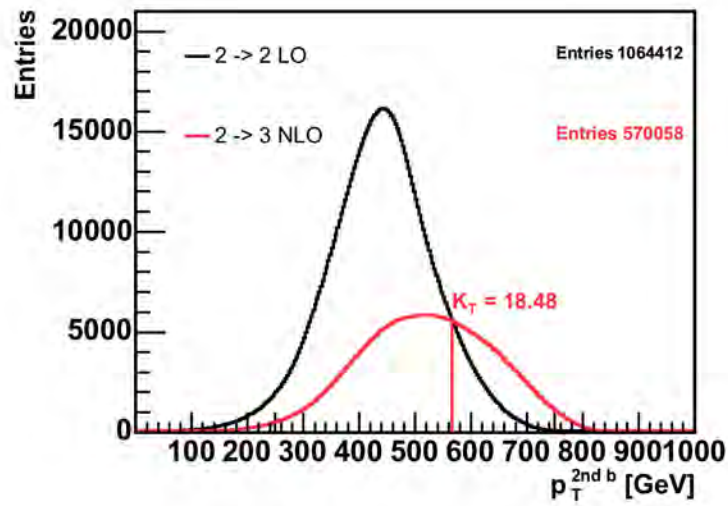
Figure 3.2. 2nd b-quark Pt distributions of LO and NLO in log scale with K_T / 18 GeV

3.2 Backgrounds

3.2.1 Top-Antitop

For the $t\bar{t}$ production, the events are generated with PYTHIA. The $t\bar{t}$ (top pair production) can be detected as single top events. There are two cases. One W decays leptonically and the other decays into two jets in the lepton plus jets and the other case is both of two bosons from top decay decay leptonically, but one lepton lost in detector.
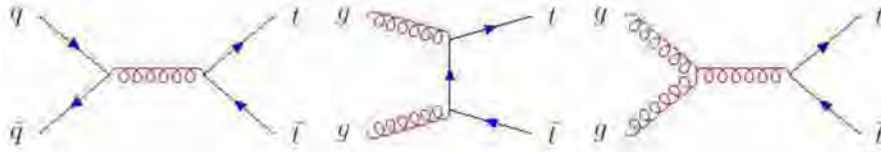
The simulated events (PYTHIA Monte Carlo sample) are used to calculate the expectation by normalizing the Monte Carlo to the theoretical cross section. The number of expected events is calculated as

$$\mu \ / \ \sigma \cdot \epsilon_{evt} \cdot L_{int}$$

where σ is theoretically predicted cross section, ϵ_{evt} is event detection efficiency, and L_{int} is the integrated luminosity.

The event detection efficiency can be calculated by selecting simulated events.

$$\epsilon_{evt} \ / \ \epsilon_{mc} \cdot \epsilon_{BR} \cdot \epsilon_{corr} \cdot \epsilon_{trig}$$

where ϵ_{mc} is detection efficiency from MC, ϵ_{trig} is the trigger efficiency, ϵ_{corr} is the correction factor between data and simulation and ϵ_{BR} is the branching fraction.

3.2.2 W + Heavy Flavor

To estimate of W + Heavy Flavor processes($W b\bar{b}$, $W c\bar{c}$, $W c$), the number of direct W+jets events, $N_{W+jets}^{N_{jets}}$, are measured by using pre-tag data sample. The number of $N_{data}^{N_{jets}}$ of W+jets candidates in pretag data is subtracted the contributions from all sources other than direct W+jets production including non-W, electroweak diboson and top-quark.

$$N_{W+jets}^{N_{jets}} \ / \ N_{data}^{N_{jets}}(1 - F_{non-W}^{N_{jets}}) - N_{diboson}^{N_{jets}} - N_{top}^{N_{jets}}$$

33

To extract heavy flavor jets from W+jets events, the ratio between W+HF jets and W+jets is obtained from Monte Carlo samples and data for the normalization.

W+heavy flavor production($W b \bar{b}$, $W c \bar{c}$, $W c$, $W + LF$ (light flavor)) is simulated by using Alpgen generator and PYTHIA showering. Specific heavy flavor processes are combined with light flavor production to obtain the Alpgen multi-jet samples, with the same procedure used to combine the Monte Carlo W+jet samples when extracting the heavy flavor fraction [41]. The W+heavy flavor(HF) contribution to the tagged lepton+jets sample is estimated by calculating the fraction of HF in W+jets events.

$$ N_{W+HF}^{tag} / N_{W+jets,data}^{pretag} \times F_{HF} \times \epsilon_{tag}^{W+HF} \times K F $$

where

$$ F_{HF} / \frac{N_{b,MC}^{W+jets}}{N_{jets,MC}^{W+jets}} $$

F_{HF} is the heavy flavor fraction of the W+jets sample, ϵ_{tag}^{W+HF} is the tagging efficiency in the W+HF MC sample, $N_{W+jets,data}^{pretag}$ is the number of pretag W+jets events in data, and $KF(F_{j,data}^{b,events} / F_{j,MC}^{b,events})$ is the calibration factor(K-factor) of the heavy flavor fraction. For $W b \bar{b}$ and $W c \bar{c}$, the fitted K-factor is measured by $1.4 = 0.4$ [37].
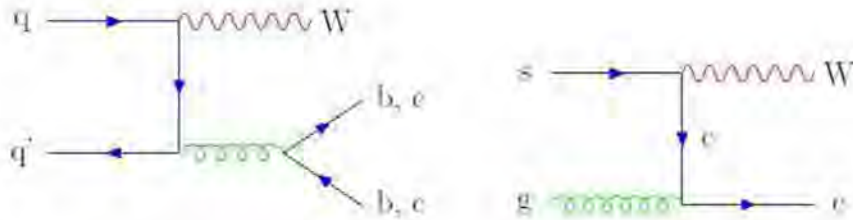
Figure 3.3. W+heavy flavor production . $W b \bar{b}$/$W c \bar{c}$, $W c$

3.2.3 Mistags

The SECVTX b-tagger is used to identify heavy-flavor quarks(mostly long-lifetime b quark) [42]. B-hadron travels a macroscopic distance before decaying, so SECVTX reconstruct a secondary vertex of a jet that is well-displaced from

34

primary interaction point. But there are fake tracks satisfy the secondary vertex requirements; those come from limited detector resolution, long-lived light particle decays(K_s and Λ), interactions in the beampipe/detector material. The resolution effects are expected to be symmetric in the signed 2D displacement L_{xy} of the vector separating the secondary and primary vertices. The mistag matrix is derived from the tagging rate with negative L_{xy} as positive L_{xy} tags. Therefore, the negative L_{xy} rate in generic jets is an approximation of the $+L_{xy}$ of light quark jets(i.e. mistag rate). To obtain the mistag contribution of a sample of $W + N_{jets}$ events, the mistag probability is computed for each jet in the event which is then summed over all events in the sample.

3.2.4 Dibosons

The diboson production WW and WZ contribute to the backgrounds according to their final states are a lepton, a neutrino and heavy-flavor jets. In the case of ZZ, one of Z decays two leptons, so this can be a background if one lepton is lost.(Figure 3.4) The theoretical NLO cross section is predicted at $^{\text{p}}\overline{\text{s}}$/ 1.96TeV to expect the number of diboson events in the data.
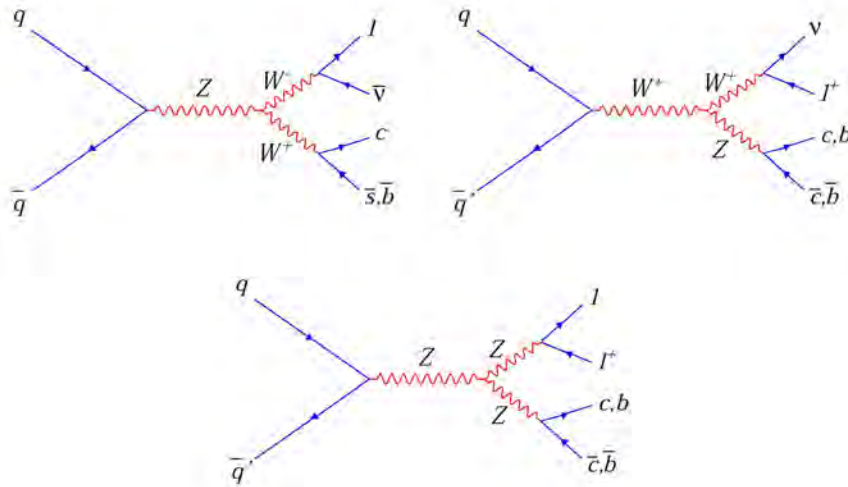
Figure 3.4. Diboson Production: WW, WZ, ZZ

3.2.5   Non-W

The non-W events(QCD backgound) are modeled from the |et electron and anti-electon.

The |et electron is a |et that fakes an electron, the QCD event coming from |et electron can pass the selection cut. The |et is required to have $E_T > 20 GeV$, $0.05 < E_{had}/E_{em} < 0.02$, and at least four |ets have to be contained in the event. The |et electrons are treated as electrons and the charge of the |et electron is assigned randomly. The antielectron model is considered to find electron candidates nearly passing the electron kinematic cuts. The pretag sample is used for this QCD background, "taggable" |et is defined as "tagged" |et.

3.3   MC Simulation of Single-top Production including NLO effect

In this chapter, we describe the study of using MC@NLO to generate single-top-quark samples. We present a comparison between the MC@NLO samples and the official MadEvent samples currently used by the single-top group. In general we find good agreement between the two samples, but there are small number of differences.

The next-to-reading oder(NLO) QCD corrections enlarge the leading-order cross section by about 30% at Tevatron. For the analysis of single-top production, NLO results are important to have a reliable estimate of the number of events expected. The MC@NLO allows to match cross section computed at NLO in QCD with an event generator. In the case of standard MC, a hard kinematic configuration is generated on an event-by-event basis, and it is subsequently showered and hadronized. In the case of MC@NLO, all of the hard kinematic configuration (events) are generated in advance, and stored in a file and then each event is showered and hadronized by HERWIG.

We generated event files using MC@NLO 3.3 package. We tell HERWIG that the events should be read from the event file using Les Houches interface by specifying a negative value of the process code IPROC. For the single-top production, IPROC is -2000-IC($H_1 H_2 \to t/\bar{t}+X$), -2001-IC($H_1 H_2 \to \bar{t}+X$), or -2004-IC($H_1 H_2 \to t+X$) by setting IC/ 10 and IC/ 20 for s- and t-channel production. $H_{1,2}$ represents hadrons, p or $\bar{p}$.

We can set IL1CODE/ 1,2,3 for the lepton identification of W-decay. Spin correlation for the decay products are therefore taken into account.

36

HEPG - post-parton-showering level

We compared the MadEvent samples and MC@NLO samples at the hepg level. MadEvent single-top samples are LO s-channel, matched(LO+NLO) t-channel, and LO t-channel (for illustration purposes). Therefore, we compare the following pairs of samples. (MadEvent LO s-channel, MC@NLO s-channel), (MadEvent LO t-channel, MC@NLO t-channel), and (MadEvent matched t-channel, MC@NLO t-channel).

Table 3.1 shows the means of the P_T and $|Pz|$ distributions for the MadEvent and MC@NLO samples. One can see that the agreement is good, with the mean values of MC@NLO distributions being consistently slightly lower than those from the MadEvent samples.

Particle	Sample	P_T		$|P_Z|$	
		MadEvent	MC@NLO	MadEvent	MC@NLO
lepton	s-chan	40.1	39.24	25.53	24.98
	LO t-chan	37.44	37.18	23.87	23.65
	Matched t-chan	37.85		24.09	
neutrino	s-chan	53.31	52	60.19	59.52
	LO t-chan	50.68	49.47	51.16	50.05
	Matched t-chan	50.49		50.79	
b from t	s-chan	64.15	62.34	72.33	70.88
	LO t-chan	60.36	59.2	60.6	59.14
	Matched t-chan	60.39		60.53	
top	s-chan	68.74	62.34	139.8	137.5
	LO t-chan	48.29	46.24	119.5	115.9
	Matched t-chan	49.28		118.4	

Table 3.1. The means of the P_T and P_Z distributions for the MadEvent and the MC@NLO samples at generator level

The compared plots of MadEvent and MC@NLO are shown Appendix B.

Reconstruction level

We compared the MadEvent single-top samples and MC@NLO single-top samples at detector-level (ie post CDF simulation, reconstruction, and trigger simulation steps) stage. We compared the distributions of η, E, Pt and $|Pz|$ of the top, lepton, neutrino, b-quark from top, b-quark not from top and the light-quark, as well as top mass and $Q \times \eta$ in Appendix B. To identify the b-from-top etc we used standard HEPG matching. The neutrino Pz is found by imposing the W mass

37

constraint for the lepton-neutrino invariant mass, and then taking the lower $|P_z|$ solution of the two (or the real part if complex solutions).

Table 3.2 shows the means of the P_T and $|Pz|$ distributions for the MadEvent and the MC@NLO samples.

Particle	Sample	P_T		$|P_Z|$	
		MadEvent	MC@NLO	MadEvent	MC@NLO
lepton	s-chan	44.55	45.02	31.07	31.42
	LO t-chan	42.24	41.9	30.93	29.79
	Matched t-chan	42.74		31.22	
neutrino	s-chan	53.77	53.32	33.23	32.4
	LO t-chan	52.82	52.62	31.83	30.98
	Matched t-chan	52.64		31.29	
b from t	s-chan	63.04	62.17	41.49	40.48
	LO t-chan	57.57	56.49	37.83	36.75
	Matched t-chan	57.45		37.41	
other b	s-chan	92.73	89.47	60.98	59.26
light q	LO t-chan	95.41	93.42	123.5	125.1
	Matched t-chan	93.38		118.4	
top	s-chan	61.35	59.97	73.83	72.67
	LO t-chan	54.45	53.01	71.32	65.66
	Matched t-chan	54.03		69.56	

Table 3.2. The means of the P_T and P_Z distribution for MadEvent and MC@NLO samples at reconstruction level

The acceptance tables and compared plots of MC@NLO and Madevent are shown in Appendix B.

Chapter 4

Data and Event Selection

4.1 Data Set

In this analysis, we used Run II CDF data of 4.8 fb^{-1} at $\sqrt{s}$ / 1.98TeV in Tevatron. Figure 4.1 shows the integrated luminosity plot during Run II (2001~2009) associated 4.8 fb^{-1} data. The data set with each period(run range) is shown in Table 4.1.

Figure 4.1. Run II(2001~2009) Integrated Luminosity; Delivered is 7.28 fb^{-1}, Acquired is 6.04 fb^{-1}, physics data is 4.8 fb^{-1} used for this analysis

For the single top production events, we select one lepton, missing E$_T$, two or three jets for final states. The leptonic W decays(electron or muon and its neutrino) is only considered to reduce the backgrouds of multi-jet production (it is difficult to distinguish signal from backgrounds due to QCD multi-jet events if W decays into quarks).

We require the lepton P$_T$ > 20 GeV, $|\eta|$ < 1.6, jet E$_T$ > 20 GeV, $|\eta|$ < 2.8,

39

missing $E_T > 25$ GeV and then also remove Dilepton, Cosmics, Conversinos, QCD events.

At least one of |ets must be tagged as b-|et reconstructed as a displaced secondary vertex at silicon vertex detector. The long lived b-quark is distinguished from the light quark using b-tagging algorithm.

Period	Run Range	Sample	Dataset
p18 - p25	261119-277511	High Pt Central Electrons	bhelmm
		High Pt Plug Electrons	bpelmm
		High Pt Central Muons	bhmumm
p14 - p17	252836-261005	High Pt Central Electrons	bhelmk
		High Pt Plug Electrons	bpelmk
		High Pt Central Muons	bhmumk
p11 - p13	233133-241665	High Pt Central Electrons	bhelm|
		High Pt Plug Electrons	bpelm|
		High Pt Central Muons	bhmum|
p08 - p10	217990-233111	High Pt Central Electrons	bhelmi
		High Pt Plug Electrons	bpelmi
		High Pt Central Muons	bhmumi
0i	203819-212133	High Pt Central Electrons	bhel0i
		High Pt Plug Electrons	bpel0i
		High Pt Central Muons	bhmu0i
0h	190697-203799	High Pt Central Electrons	bhel0h
		High Pt Plug Electrons	bpel0h
		High Pt Central Muons	bhmu0h
0d	138425-186598	High Pt Central Electrons	bhel0d
		High Pt Plug Electrons	bpel0d
		High Pt Central Muons	bhmu0d

Table 4.1. CDF Dataset Summary . data $\sim$p25 (luminosity 4.8 fb^{-1} with silicon)

4.2 Trigger

A high p$_T$ central lepton trigger used for the data sample. Used data sets are listed in Table 4.1.

The cetral electrons are required to pass ELECTRON_CENTRAL_18 trigger. At least one calorimeter tower with $E_T > 8$ GeV and $E_{had}/E_{em} < 0.125$ are requried, and also at least one COT track with a XFT track with p$_T > 8$ GeV with hits in at least four XFT layers is demanded at level 1. At level 2, the

40
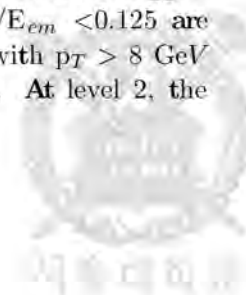
CEM energy cluster have to be $E_T > 18$ GeV, $E_{had}/E_{em} < 0.125$, $\eta < 1.317$ and XFT track with $p_T > 8$ GeV with hits in at least four XFT layers and stereo confirmation. At level 3, it requires a COT track with $p_T > 8$ GeV/c matched to an energy cluster in the CEM with $E_T > 18$ GeV with $E_{had}/E_{em} < 0.125$. The forward electrons have to pass the MET_PEM trigger which is not only PEM because of higher background energy deposition from elastic collision and beam remnants in the forward region. At least one forward calorimeter tower with $E_T > 8$ GeV and $E_{had}/E_{em} < 0.125$ are requried and in the forward region, $E_{had}/E_{em} < 0.0625$ and $\not{E}_T > 15$GeV at level 1. At level 2, an electromagnetic ob|ect with $1.1 < |\eta| < 3.6$ and $E_T > 20$ GeV is required.

The central muon trigger MUON_CMUP18 demands a track $p_T > 18$ GeV/c in COT matched to track segments of both CMU and CMP. The forward muon trigger MUON_CMX18 requires a COT track with $p_T > 18$ GeV/c has to be matched with reconstructed stubs in CMX.

4.3 Selection for W Candidates

4.3.1 Lepton

Electron Candidate Selection

The selection cuts on electron candidates are required to increase the sample purity. The energy deposited in the electromagnetic calorimeter have to match a track from the tracking system and also electron has to be distiguished from other particles(charged hadrons or photons). For the central electron, $E_T > 20$ GeV in CEM has to match with a reconstructed track $P_T \geq$ GeV and Isolation has to be less than 0.1. Table 4.2 lists central electron candidate requirements. For the forward electron, $E_T > 20$ GeV in PEM is required. Table 4.3 shows plug electron candidate requirements.

- E_T . Total transverse energy of towers in the cluster.

- P_T . Transverse momentum of the COT track pointing to the cluster.

- E/p . Ratio of the energy in the EM cluster to the associated track's transverse momentum in COT. This is useful to re|ect the accidental overlap of charged hadrons and photons.

- E_{had}/E_{em} . Ratio of energies measured in the hadronic calorimeter of the CHA and WHA to that from the EM calorimeter(CEM). An real electron has a smaller value of E_{had}/E_{em}.

41

Central Tight Electrons	
Geometric	Fiducial in CEM
E_T	≥ 20 GeV
Track $|4\ z_0|$	≤ 60 cm
Track P_T	≥ 10 GeV/c
E_{had}/E_{em}	$\leq 0.055 + 0.00045*E$
L_{shr}	≤ 0.2
E/P if $P_T \leq 50$ GeV/c	≤ 2
$|4\ z|$	≤ 3 cm
$Q \times 4\ x$	$\geq$ -3.0 and ≤ 1.5 cm
χ^2_{strip}	≤ 10
# axial SL	≥ 3
# stereo SL	≥ 2
Isolation	≤ 0.1

Table 4.2. Cental Electron Identification Requirements

Plug Tight Phoenix Electrons	
E_T	≥ 20 GeV
Track $|4\ z_0|$	≤ 60 cm
# Silicon Hits	≥ 3
PES 2D Eta	$1.2 \leq |\eta| \leq 2.8$
E_{had}/E_{em}	≤ 0.05
PEM 3$\times$3 χ^2	≤ 10
PES 5$\times$9 U	≥ 0.65
PES 5$\times$9 V	≥ 0.65
Isolation	≤ 0.1
$|4\ R|$	≤ 3.0 cm

Table 4.3. Plug Electron Identification Requirements

42

- $| 4 z_0 |$. $4 z_0$ of the eletron track is required to be within 60 cm of the nominal interaction point.

- L_{shr} . A measure of the difference between lateral development of an electron candidate's shower profile and the expected profile as measured in test beam data. Most electrons deposit the energy on a single CEM tower because the lateral size of electromagnetic shower is smaller than the tower size. However, an overlap event of charged hadron and multiple photons can leave extra energies on towers adjacent to a seed tower by multi-photon hit.

- $|$ axial/stereo SL . Number of axial/stereo super laters with hits associated to the COT track, pointing to the EM cluster.

- Isolation . The amount of energy that is deposited in a cone around a track for distinguishing between an isolated particle and a particle in a jet. Isolation is defined as $(E_T^{cone} - E_T^{cluster})/E_T^{cluster}$, where E_T^{cone} is the E_T of all towers in a cone of $4 R / 0.4$ centered on the electron cluster and $E_T^{cluster}$ is the total E_T of towers included in the cluster.

Muon Candidate Selection

The muon candidates are required a COT track $p_T > 20 GeV/c$ that pointed to a track segment in a muon chamber. For central muon, track segments are detected in both CMU and CMP(this defines CMUP muons), or in the CMX. Table 4.4 shows the muon identification requirements.

4.3.2 Neutrino

The neutrino escape the detector, so the missing energy of transverse direction is defind as E_T of neutrino and Pz of neutrino is calculated by using W mass constraint. First, missing transverse energy is summed over all calorimeter towers.

$$\not{E}_T / -\sum_i E_T^i \hat{n}_i$$

where E_T^i is the transverse energy deposited in the ith calorimeter tower, $\hat{n}_i$ is a unit vector perpendicular to the beam axis pointing to the ith calorimeter tower. The muons leave a minimum amount of energy in the calorimeter, so muon E_T can be measured from muon P_T (mass is negligible compared to the kinematic energy). In this case, $\not{E}_T$ is calculated as $(\not{E}_T^{corr})_{xy} / (\not{E}_T^{raw})_{xy} - (p_\mu)_{xy} + (\not{E}_T^{depos})_{xy}$. The small amount energy deposited in the calorimeter by the

43

Central Muon Candidate	
Geometric	Fiducial in CMUP or CMX
P_T	> 20 GeV/c
E_{em}	< 2 GeV $+$ max(0, 0.0115*(p-100))
E_{had}	< 6 GeV $+$ max(0, 0.0280*(p-100))
Tracks with no silicon hits	$|d0| < 0.2$ cm
Tracks with silicon hits	$|d0| < 0.02$ cm
(if CMUP) $|4 \, x|_{CMU}$	< 7.0 cm
(if CMUP) $|4 \, x|_{CMP}$	< 5.0 cm
(if CMX) $|4 \, x|_{CMX}$	< 6.0 cm
$4 \, z_0$	< 60 cm
# axial SL	≥ 3
# stereo SL	≥ 2
Isolation	< 0.1

Table 4.4. Muon Identification Requirements

muons is subtrated. For Pz of neutrino, we set W mass as 80.4GeV and use $m_W / \sqrt{(p_l + p_\nu)^2}$.

4.4 Jet Reconstruction

The |ets are identified using a cone-clustering algorithm with cone size 4 R / $\sqrt{4 \, \eta^2 + 4 \, \phi^2}$. The sum of energy deposited in a cone with radius 0.4 which is centered at seed cluster is refered to as 'raw' energy of |et. This measured 'raw' energy is underestimated compared to the original parton |et. Therefore, the measured |et energy have to be corrected to the parent parton energy as the following |et correction procedures.

Jet Corrections

The |et corrections from several different sources are performed with different 'levels'. The sources are the respose of the calorimeter to different particles, non-linearity response of the calorimeter to the particle energies, spectator interactions, energy radiated outside the |et clustering algorithm and so on. The |et energy correction has the following eight levels.

• Level 0. Online and **Offline calibrations**

This correction sets the calorimeter energy scale. CEM scale set to Z→ee

44

peak(91.2GeV). The time dependence and PMT gains are tracked via the inclusive 8GeV electron data. CHA scale is set to Run 1 MIP(Minimum Ionizing Particles) peak and tower gain varitions are tracked via J/Psi muons and min-bias rates. WHA scale is tracked with source calibrations. PEM/PHA PMT gains drop with integrated charge, and are tracked with offline LERs from frequent laser calibrations. Scale shifts are tracked via a combination of source calibraions and CP $Z{\rightarrow}$ee data.

- Level 1. Eta Dependence

This correction is the "eta-dependent of relative correction" to correct measured |et energy uniformly along eta. The η-dependent corrections are performed using the "di|et balancing method". The transverse energy of the two |ets in di|et events should be balanced. This property is used to scale |ets outside the $0.2 < |\eta| < 0.6$ region to |ets inside the region because CEM and CHA are well understood calorimeters.

- Level 2

It was for removing time dependence of the calorimeter PMTs. This is now done at the tower level in level0. Currently, this correction is not being applied.

- Level 3

This correction took care of the differences in scale between Run I vs Run II. In Gen4 it also covered some difference between MC and data observed in photon+|ets events. Now this difference is covered by other uncertainties, so it is not being applied.

- Level 4. Multiple Interactions

At high instantaneous luminosities more than one p$\bar{\text{p}}$ interaction occurs in the same bunch crossing. The energy from different p$\bar{\text{p}}$ interaction inside the |et cluster increases measured |et energy, so this extra energy should be subtracted. The average transverse energy in a cone is measured using minimum bias data sample and this data are parameterized as a function of the number of vertices in the event. The transverse energy in a cone, which is defined using a seed tower randomly selected in the central calorimeter region $0.2< |\eta| < 0.6$, is measured as a function of the number of vertices for three cone size.

45

- Level 5. **Absolute Energy Scale**

The **absolute correction carry** out the transformation of the meausured |et energy into the energy correponding to the underlying particle |et. Since the **calorimeter** simulation is optimized to reproduce the measured single particle response, we rely on the simulation for **correction** over a wide range of |et transverse momentum.

- Level 6. Underlying Events

The particle |et not related to the **actual** mother partons of the hard interaction of the |et is called "Underlying Event"; such as the initial state radiation(ISR) or spectator partons with color connection to the other partons of the proton. Therefore, the UE energy needs to be subtracted from the particle-level |et energy.

- Level 7. Out of Cone Corrections

A fraction of the parton energy can be lost from the |et cone due to final state gluon **radiation(FSR)** and this energy is called "Out-of-Cone" energy. Final State Radiation and hadronization are correlated with the primary |et direction and the energy. The corrections are determined from MC simulation at particle generator level. The systematic uncertainty of UE and OOC correction is derived from comparisions of the energy measured in calorimeter towers in a |et cone with the simulation of Phthia and Herwig.

4.5 B Jet Idendification

The idenfication of |ets from **b** quark (or b-tagging) is important to reconstruct the top quark.

The b-|ets have the different features from light flavor and charm |ets.the long lifetime of the b quark, large mass of B hadrons and energetic semileptonic decay of B hadrons.

To idenfify **b** |et, we use CDF's secondary vertex b-tagger(b-tagging tool) using these distinguishing features.

The **b-quark** hadronizes almost immediately to form a |et of particles; a B meson(B^0, $B^\pm$,B_s^0) or a B baryon(Λ_B) is included in a |et. The B hadron usually has most of the original b-quark momentum and has a long lifetime. Before decaying particles, the B hadrons moved a macroscopic distance away from the primary intercation point due to this long lifetime and large boost. Each track's impact parameter(d_0) is measured with respect to a primary pp̄ interaction posi-

46

tion(or primary vertex). The silicon tracks within jet are required to have $p_T >$ 0.5 GeV, d_0 significance S_{d_0} / $|\frac{d_0}{\delta_{d_0}}| > 2.0$, minimum number of hits in the silicon tracking detector and finally the tracks must not exceed a maximum d_0 requirement. The selected tracks are ordered in p_T and then a 2-track "seed" vertex is searched among those tracks. If a seed vertex is found, the remaining tracks are considered for vertexing with the seed tracks. The vertex χ^2 is calculated after attaching all qualifying tracks to the vertex, and tracks are iteratively pruned from the vertex if they contribute too much to the overall χ^2. Having three or more tracks is final cuts, including removal of vertices from material, nuclear interactions, long-lived light flavor hadrons and so on. Finally the vertex is required to have $S_{L_{xy}} > 7.5$, where $S_{L_{xy}}$ / $|L_{xt}/\delta_{L_{xy}}|$. L_{xy} is the 2D decay length of the fitted vertex with respect to the primary. The jet is defined as "tagged" if a secondary vertex is found as either followng criterion. The tag is called "positive" if the product of the 2D displacement vector from primary vertex to the secondary vertex and the jet's momentum is positive, and the tag is called "negative" if that product is negative. Most b-tags are reconstructed in the "positive" tag, and "negative" tagged jets are considered as mistags.
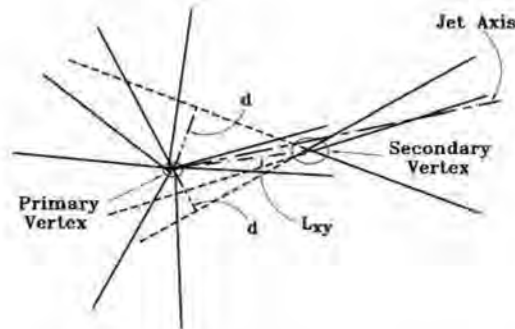
Figure 4.2. Primary and Secondary vertices of tracks of jet

4.6 Data Reduction and Final Candidate Sample

For single-top analysis, the proper modeling of the signal and background processes is important, as well as precise estimate of the signal and background components of the data. We can select more pure signal events reducing backgrounds by applying the W selection and jet requirement explained previous sections. For

47

further event selection requirement, the event vetoes also contribute to reduce the background events.

Dilepton *Veto*

We require one lepton per event for single-top analysis, so the events having additional lepton are removed. Also the events coming from $t\bar{t}$ or diboson background can be reduced from this selection cut.

z *Vertex Cut*

The recontructed primary z vertex of the events have to be put in a region within ± 60 cm of the center of the detector.

Z *Boson Veto*

The events having leptons supposed to come from Z boson is removed. The invariant mass of two leptons is consistent with a Z boson mass as $76 \text{GeV}/\mathbf{c}^2 \leq \text{M}_Z \leq 106 \text{ GeV}/\mathbf{c}^2$.

QCD *Veto*

The events from QCD multijet(non-W) is also removed. Because the QCD events do not have $\slashed{E}_T$, the events passing $\slashed{E}_T$ cut come from lost or mismeasured jets. The assumed QCD events has following features. The measured $\slashed{E}_T$ is low, $\slashed{E}_T$ lines up with the direction of the leading jet. Thus, the QCD cut removes the events which $\slashed{E}_T < 30$ GeV and the angle between the $\slashed{E}_T$ and the leading jet is less than 0.5 or greater than 2.5 radians. The additional cuts for each lepton category are explained in [53].

The expected number of signal and background processes are obtained from CDF's Method II. The theoretically well known process's expectation is decided using simulated events.

The event selection tables of signal events of s-channel(stop00) and one of W$b\bar{b}$ backgrounds(btop0w) for each lepton category, for example, are shown in Table 4.5∼ 4.12. The event efficiency of s-channel is 14% for 2jet and 7.2% for 3jet and t-channel is 9.5% for 2jet and 5.2% for 3jet events. The efficiency of $t\bar{t}$ is 14% for 2jet and 12.8% for 3jet, W$b\bar{b}$ is 3% for 2jet and 4% for 3jet, W$c\bar{c}$ is 1% for 2jet and 1% for 3jet and W+LF is 0.2% for 2jet and 0.57% for 3jet. The efficiency of Diboson is 0.56% for 2jet and 0.19% for 3jet and Z+jets is 0.1% for 2jet and 0.2% for 3jet. As it shows, the efficiency of single-top signal processes is much higher than the efficiency of the backgrounds except $t\bar{t}$ background.
The final expectation number of signal and backgrounds and the number of observed data are shown in Table 4.13.

48

CEM	0Jet	1Jet	2Jet	3Jet	4+Jet	Total
Stage 0 Initial	9353	130201	418316	266628	93675	918173
Stage 1 Good Run	8870	124129	397188	249766	87422	867375
Stage 2 Trigger	8870	124129	397188	249766	87422	867375
Stage 3 >/ 1 TLep	1540	21244	62256	25088	8106	118234
Stage 4 Met	1321	17786	52257	21249	6996	99609
Stage 5 Iso	1321	17441	49261	17040	4816	89879
Stage 6 Dilep	1311	17259	48899	16943	4787	89199
Stage 7 Z	1300	17134	48561	16808	4750	88553
Stage 8 Conv	1300	17067	47994	15185	4059	85605
Stage 9 Diff Z	1300	17067	47990	15184	4058	85599
Stage 10 QCD	1300	16249	45092	14154	4058	80853
Stage 11 Si Good Run	1300	16249	45092	14154	4058	80853
Stage 12 Taggable	0	12278	41684	13491	3913	71366
Stage 13 >/ 1 +b-tag	0	5962	26330	8444	2460	43196

Table 4.5. CEM Acceptance Table of s-channel Sample(stop00)

PHX	0Jet	1Jet	2Jet	3Jet	4+Jet	Total
Stage 0 Initial	9353	130201	418316	266628	93675	918173
Stage 1 Good Run	8870	124129	397188	249766	87422	867375
Stage 2 Trigger	8870	124129	397188	249766	87422	867375
Stage 3 >/ 1 TLep	524	6353	15828	5028	1362	29095
Stage 4 Met	453	5212	12951	4186	1130	23932
Stage 5 Iso	453	5175	12615	3685	925	22853
Stage 6 Dilep	447	5123	12535	3659	918	22682
Stage 7 Z	445	5090	12441	3632	907	22515
Stage 8 Conv	445	5090	12441	3632	907	22515
Stage 9 Diff Z	445	5090	12440	3632	907	22514
Stage 10 QCD	445	4716	10748	3099	907	19915
Stage 11 Si Good Run	445	4716	10748	3099	907	19915
Stage 12 Taggable	0	3607	10206	3038	897	17748
Stage 13 >/ 1 +b-tag	0	1707	6339	1927	575	10548

Table 4.6. PHX Acceptance Table of s-channel Sample(stop00)

49

CMUP	0Jet	1Jet	2Jet	3Jet	4+Jet	Total
Stage 0 Initial	9353	130201	418316	266628	93675	918173
Stage 1 Good Run	8870	124129	397188	249766	87422	867375
Stage 2 Trigger	8870	124129	397188	249766	87422	867375
Stage 3 >/ 1 TLep	1005	13342	39348	13453	3804	70952
Stage 4 Met	804	10970	32518	11128	3172	58592
Stage 5 Iso	751	10244	29822	9623	2558	52998
Stage 6 Dilep	743	10173	29592	9560	2535	52603
Stage 7 Z	742	10129	29479	9517	2523	52390
Stage 8 Conv	742	10129	29479	9517	2523	52390
Stage 9 Diff Z	742	10128	29478	9516	2523	52387
Stage 10 QCD	742	9488	28659	9246	2523	50658
Stage 11 Si Good Run	742	9488	28659	9246	2523	50658
Stage 12 Taggable	0	7162	26519	8795	2434	44910
Stage 13 >/ 1 +b-tag	0	3464	16722	5427	1572	27185

Table 4.7. CMUP **Acceptance** Table of **s-channel** Sample(stop00)

CMX	0Jet	1Jet	2Jet	3Jet	4+Jet	Total
Stage 0 Initial	9353	130201	418316	266628	93675	918173
Stage 1 Good Run	8781	122713	392743	247012	86445	857694
Stage 2 Trigger	8781	122713	392743	247012	86445	857694
Stage 3 >/ 1 TLep	464	6103	17390	5814	1571	31342
Stage 4 Met	380	4992	14393	4837	1316	25918
Stage 5 Iso	351	4674	13183	4171	1079	23458
Stage 6 Dilep	345	4634	13091	4142	1071	23283
Stage 7 Z	343	4617	13047	4117	1065	23189
Stage 8 Conv	343	4617	13047	4117	1065	23189
Stage 9 Diff Z	343	4617	13046	4116	1065	23187
Stage 10 QCD	343	4515	12700	3999	1065	22622
Stage 11 Si Good Run	343	4515	12700	3999	1065	22622
Stage 12 Taggable	0	3374	11937	3832	1039	20182
Stage 13 >/ 1 +b-tag	0	1630	7528	2407	644	12209

Table 4.8. CMX **Acceptance** Table of **s-channel** Sample(stop00)

CEM	0Jet	1Jet	2Jet	3Jet	4+Jet	Total
Stage 0 Initial	515254	708112	270256	46603	2314	1542539
Stage 1 Good Run	501996	662337	249283	42357	2104	1458077
Stage 2 Trigger	501996	662337	249283	42357	2104	1458077
Stage 3 >/ 1 TLep	243906	156610	41891	4059	243	446709
Stage 4 Met	206455	124699	34099	3524	202	368979
Stage 5 Iso	206455	107764	26542	1929	108	342798
Stage 6 Dilep	206392	107589	26461	1921	108	342471
Stage 7 Z	205883	107122	26289	1901	107	341302
Stage 8 Conv	205883	100408	22757	1079	63	330190
Stage 9 Diff Z	205849	100395	22755	1079	63	330141
Stage 10 QCD	205849	97689	22064	1036	63	326701
Stage 11 Si Good Run	205849	97689	22064	1036	63	326701
Stage 12 Taggable	0	66352	19086	955	59	86452
Stage 13 >/ 1 +b-tag	0	27900	10992	549	39	39480

Table 4.9. CEM **Acceptance** Table of Wbb Sample(btop0w)

PHX	0Jet	1Jet	2Jet	3Jet	4+Jet	Total
Stage 0 Initial	9353	130201	418316	266628	93675	918173
Stage 1 Good Run	8870	124129	397188	249766	87422	867375
Stage 2 Trigger	8870	124129	397188	249766	87422	867375
Stage 3 >/ 1 TLep	524	6353	15828	5028	1362	29095
Stage 4 Met	453	5212	12951	4186	1130	23932
Stage 5 Iso	453	5175	12615	3685	925	22853
Stage 6 Dilep	447	5123	12535	3659	918	22682
Stage 7 Z	445	5090	12441	3632	907	22515
Stage 8 Conv	445	5090	12441	3632	907	22515
Stage 9 Diff Z	445	5090	12440	3632	907	22514
Stage 10 QCD	445	4716	10748	3099	907	19915
Stage 11 Si Good Run	445	4716	10748	3099	907	19915
Stage 12 Taggable	0	3607	10206	3038	897	17748
Stage 13 >/ 1 +b-tag	0	1707	6339	1927	575	10548

Table 4.10. PHX **Acceptance** Table of Wbb Sample(btop0w)

CMUP	0Jet	1Jet	2Jet	3Jet	4+Jet	Total
Stage 0 Initial	9353	130201	418316	266628	93675	918173
Stage 1 Good Run	8870	124129	397188	249766	87422	867375
Stage 2 Trigger	8870	124129	397188	249766	87422	867375
Stage 3 >/ 1 TLep	1005	13342	39348	13453	3804	70952
Stage 4 Met	804	10970	32518	11128	3172	58592
Stage 5 Iso	751	10244	29822	9623	2558	52998
Stage 6 Dilep	743	10173	29592	9560	2535	52603
Stage 7 Z	742	10129	29479	9517	2523	52390
Stage 8 Conv	742	10129	29479	9517	2523	52390
Stage 9 Diff Z	742	10128	29478	9516	2523	52387
Stage 10 QCD	742	9488	28659	9246	2523	50658
Stage 11 Si Good Run	742	9488	28659	9246	2523	50658
Stage 12 Taggable	0	7162	26519	8795	2434	44910
Stage 13 >/ 1 +b-tag	0	3464	16722	5427	1572	27185

Table 4.11. CMUP **Acceptance** Table of Wbb Sample(btop0w)

CMX	0Jet	1Jet	2Jet	3Jet	4+Jet	Total
Stage 0 Initial	9353	130201	418316	266628	93675	918173
Stage 1 Good Run	8781	122713	392743	247012	86445	857694
Stage 2 Trigger	8781	122713	392743	247012	86445	857694
Stage 3 >/ 1 TLep	464	6103	17390	5814	1571	31342
Stage 4 Met	380	4992	14393	4837	1316	25918
Stage 5 Iso	351	4674	13183	4171	1079	23458
Stage 6 Dilep	345	4634	13091	4142	1071	23283
Stage 7 Z	343	4617	13047	4117	1065	23189
Stage 8 Conv	343	4617	13047	4117	1065	23189
Stage 9 Diff Z	343	4617	13046	4116	1065	23187
Stage 10 QCD	343	4515	12700	3999	1065	22622
Stage 11 Si Good Run	343	4515	12700	3999	1065	22622
Stage 12 Taggable	0	3374	11937	3832	1039	20182
Stage 13 >/ 1 +b-tag	0	1630	7528	2407	644	12209

Table 4.12. CMX **Acceptance** Table of Wbb Sample(btop0w)

	2jets	3jets
s-channel	72.7 ± 10.5	23.2 ± 3.3
t-channel	111.4 ± 16.5	32.4 ± 4.8
Wbb	906.9 ± 273.4	259.5 ± 78.4
Wcc+Wc	755.25 ± 232.9	192.1 ± 59.2
Mistag	681.6 ± 95.4	195.3 ± 27.9
ttbar	246.75 ± 35.8	559.65 ± 81
Z+jets	41.85 ± 6.4	16.2 ± 2.4
Diboson	117.45 ± 12.15	37.1 ± 3.9
non-W	123.3 ± 49.35	49.8 ± 19.9
Total Signal	184.1 ± 27.0	55.6 ± 8.1
Total Prediction	3057 ± 519.3	1365.3 ± 162.4
Observed in Data	2920	1300

Table 4.13. Data and Background for single-top production with 4.8 fb^{-1}

After the selection cut, the plots of Pt(transeverse momentum) of lepton, missing Et, Pt of tagged jet(to select b-quark from top) and E(energy) of lepton, E of neurino, E of tagged jet are shown in Figure 4.3 ~ 4.8.
In the case of the tagged jet, the transverse momentum of single-top (s-channel, t-channel) and $t\bar{t}$ are higher than $W b\bar{b}$, $Wc(\bar{c})$ and mistag. Also the peak of energy of single-top and $t\bar{t}$ are higher than other backgrounds.

53
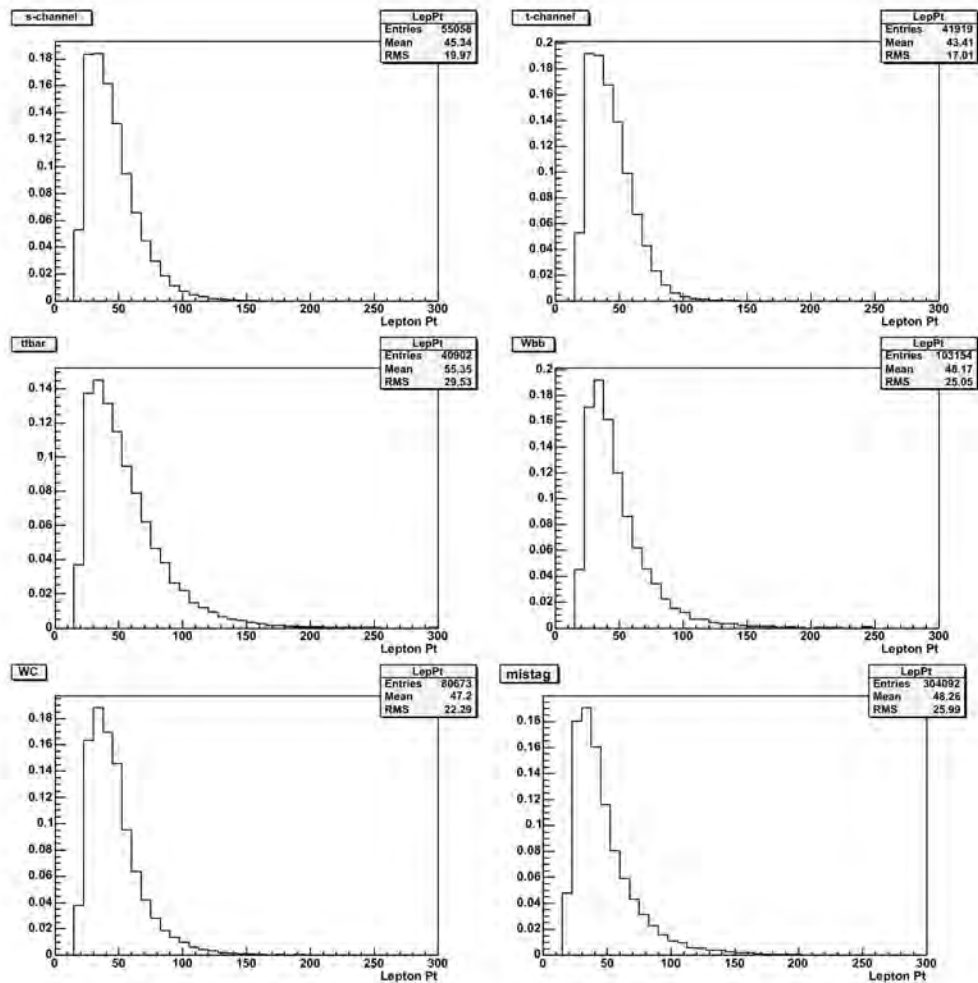
Figure 4.3. Lepton Pt of s-channel, t-channel, t$\bar{\text{t}}$, W b$\bar{\text{b}}$, W c($\bar{\text{c}}$) and mistag after selection cut

54
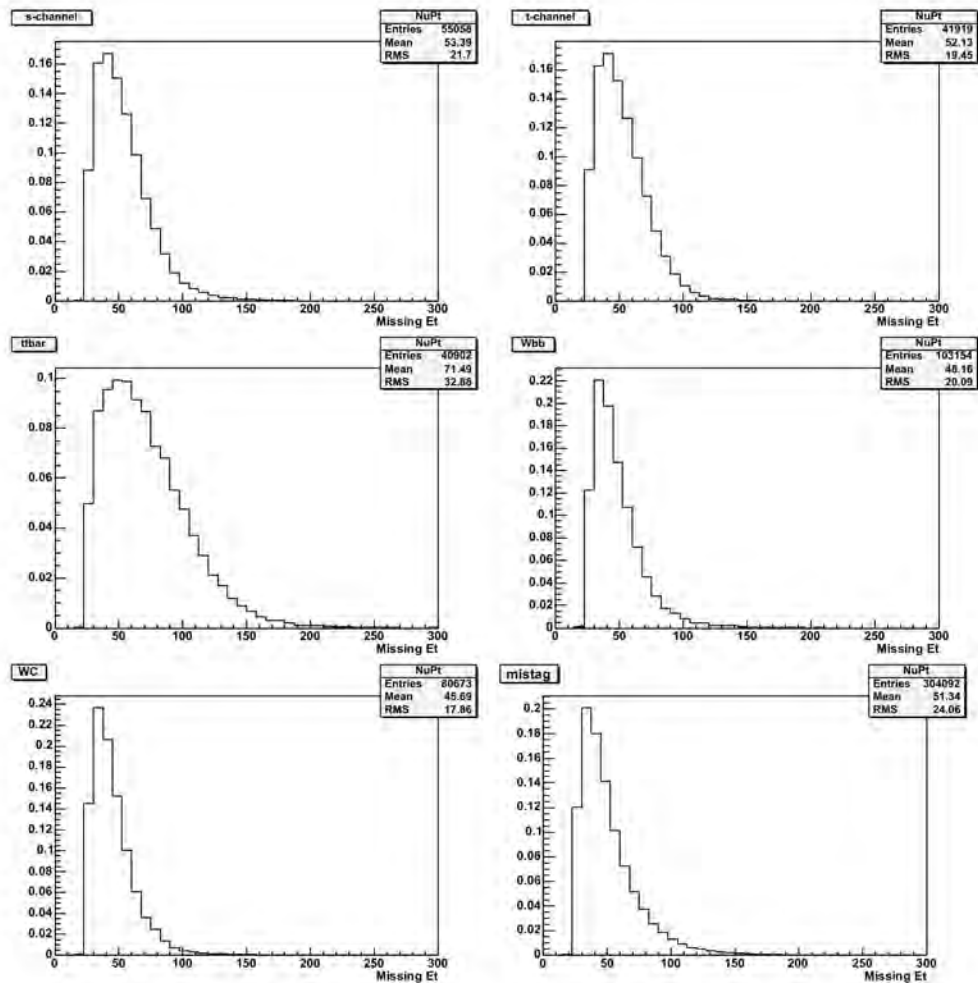
Figure 4.4. Missing Et of s-channel, t-channel, tt̄, Wbb̄ Wc(c̄) and mistag after selection cut
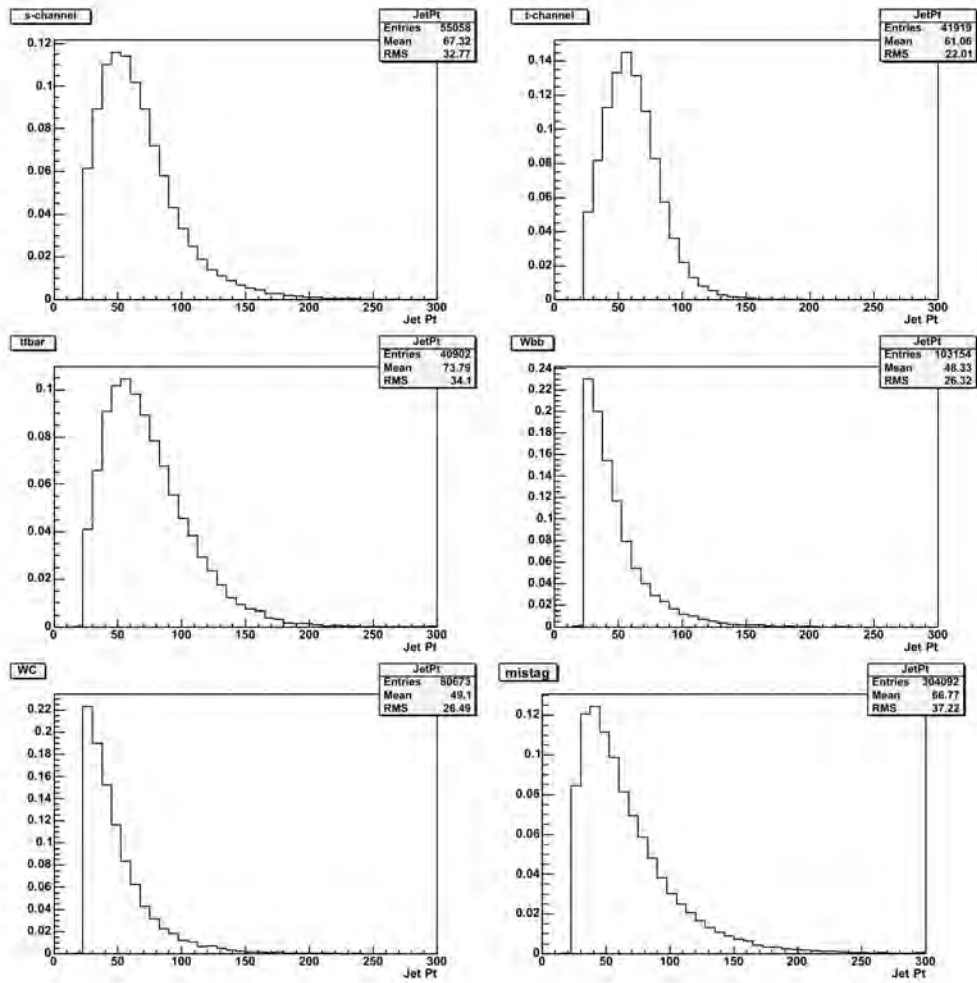
Figure 4.5. Tagged Jet Pt of s-channel, t-channel and tt̄ after selection cut

56
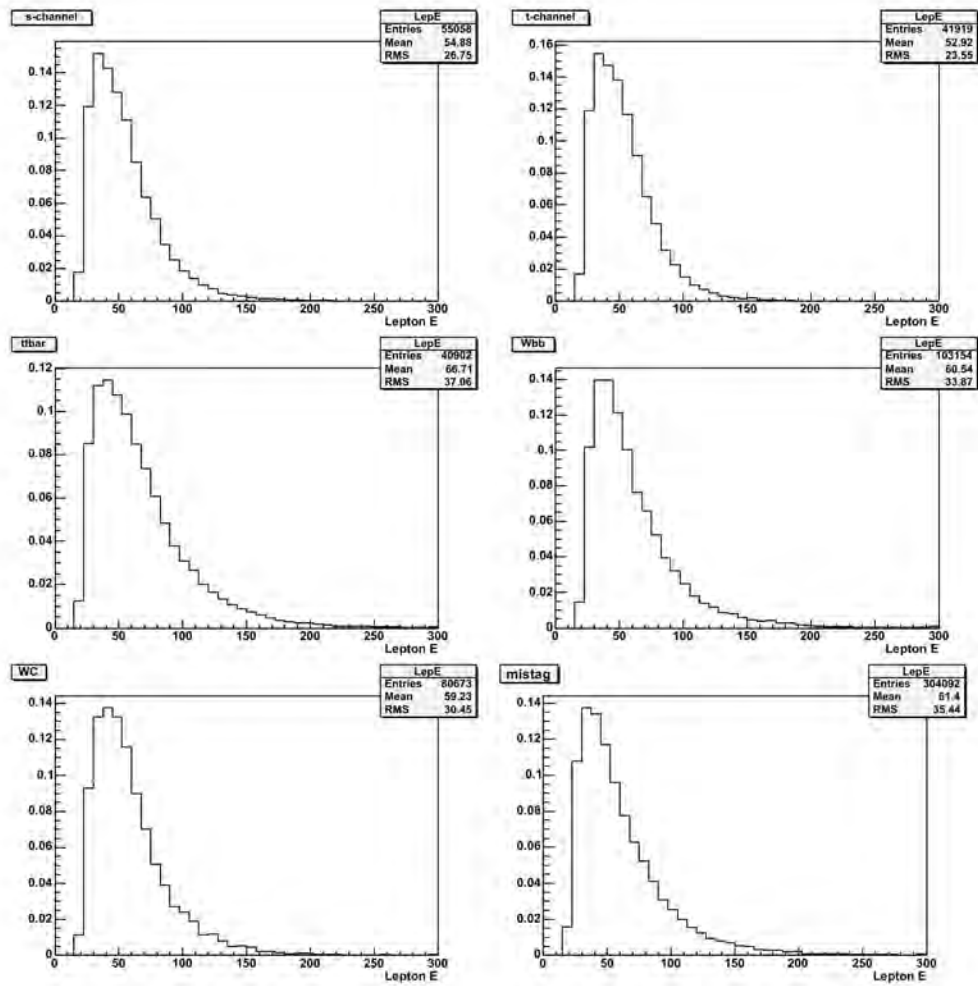
Figure 4.6. Lepton Energy of s-channel, t-channel, t$\bar{\text{t}}$, W b$\bar{\text{b}}$, Wc($\bar{\text{c}}$) and mistag after selection cut

57
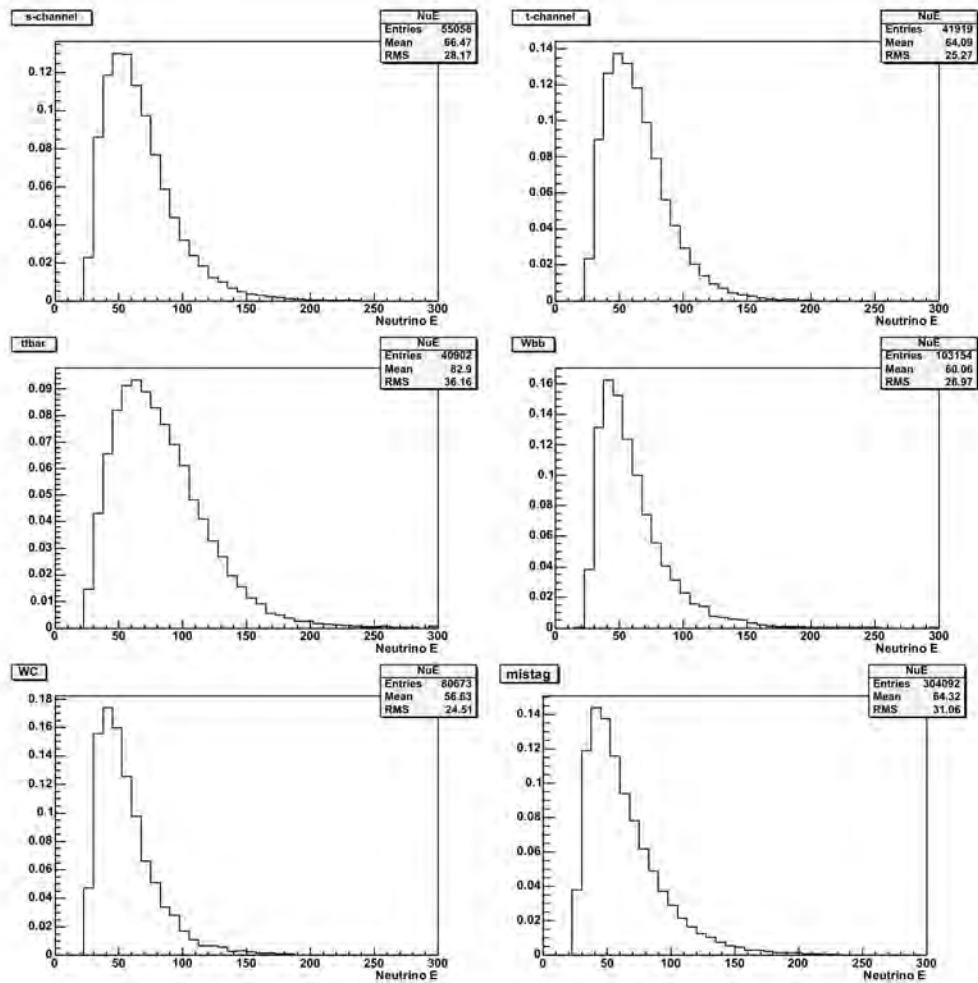
Figure 4.7. Neutrino Energy of s-channel, t-channel, $t\bar{t}$, W$b\bar{b}$, W$c(\bar{c})$ and mistag after selection cut

58
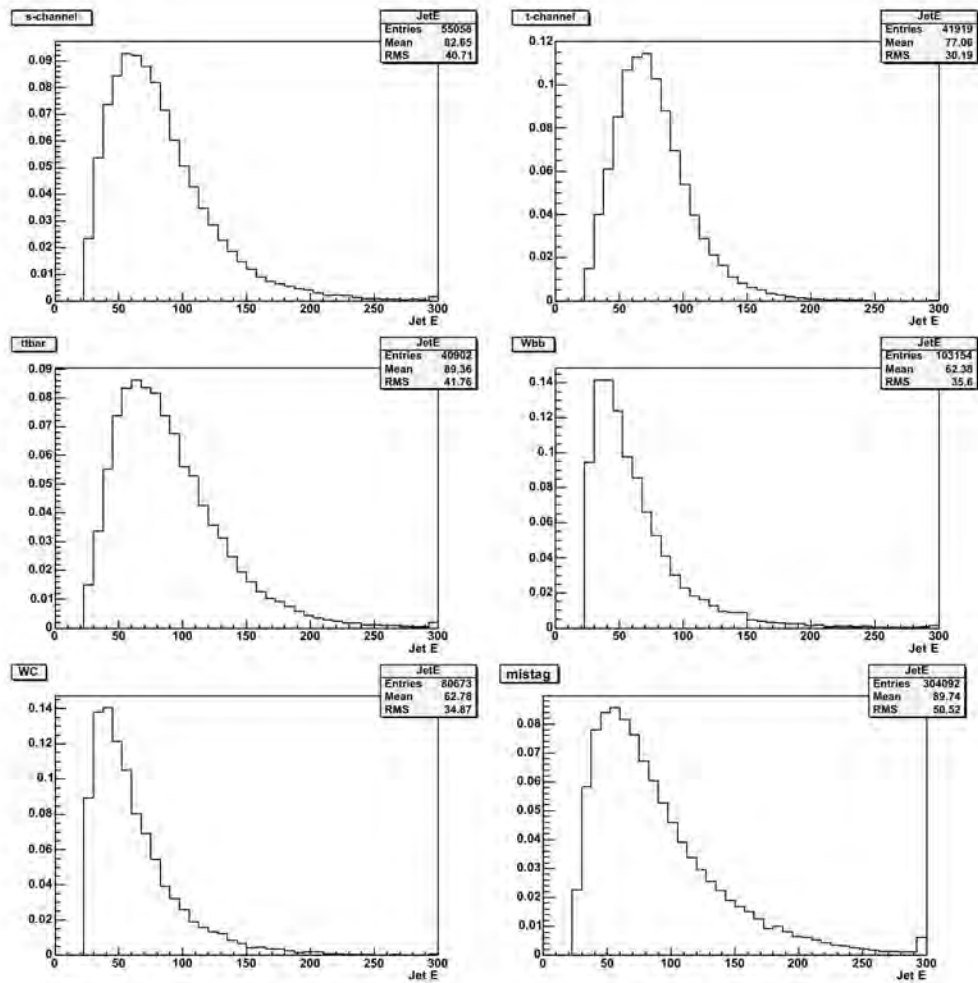
Figure 4.8. Tagged Jet Energy of s-channel, t-channel, $t\bar{t}$, $Wb\bar{b}$, $Wc(\bar{c})$ and mistag after selection cut

59

Chapter 5

Likelihood Method

This analysis present the measurement of single-top production using a multivariate likelihood function(LF) technique with 4.8 fb^{-1} data at p$\bar{\text{p}}$ collision at $\sqrt{s}$ / 1.96 TeV. It is difficult to distinguish signal from the backgrounds due to much background compared to single-top signal events. To observe single-top events, we used a technique of multivariate likelihood function. The discriminant input variables are chosen to separate optimally signal from the background. Many kinematic variables are used for the discriminant variables using four vector of lepton, neutrino, b $|$et or light quark $|$et. Finally, those input variables are combined into one discriminant(LF).

5.1 Likelihood Fuction

To distiguish single-top signal events from backgrounds, we used the multivariate likelihood function discriminant and require at least one b tagged $|$et in 2$|$et or 3$|$et events.

The single-top final state have one tight lepton, a neutrino, and two or three tight $|$ets. To find four-vectors of the b $|$et and the neutrino(reltively lepton momentum vector is well measured), the kinematic solver is used by constraing the mass of top quark(175GeV) and W boson(80.4GeV). The output from the kinematic solver is a set of neutrino Pz and b-$|$et four vector and used to reconstruct kinematic variables. We choose the input variables for each 2$|$et and 3$|$et events to maximally separate signal from background.

One of strongest input variables is Q $\times$ η, the charge of the lepton times the pseudorapidity of the not b-tagged $|$et. This gives asymetry for t-channel single-top production because the quark which donates the W travels predominantly in the same direction it was going before the interaction and the lepton charge determines the sign of the top quark. As another angle-related variable, the

60
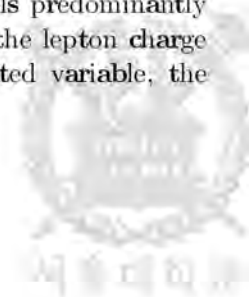
angle of cosine between the lepton and the untagged jet in the top rest frame. The signal(especially t-channel) is distiguished from background because the electroweakly produced top quark is nearly 100% polarized. For energy related variables, H_T, the scalar sum of the transverse energies of the two jets, the lepton, the missing energy, and $M_{l\nu b}$,reconstructed top mass, and the mass of two jets are considered. The strategy is to combine various variables to optimize the likelihood function. Generally, a large number of variables are considered and choose the best input variables.

The likelihood fuction L is constructed by forming histograms of each variables. The value of each bin of histograms is denoted f_{ijk} where i is the variable, j is the bin, and k is the event class ($k=1$ for t-channel signal and $k=2,3,4,5$ for backgrounds). Because t-channel signal events compared to the s-channel has good features for the separation from backgrounds, the variables is formed for t-channel likelihood function L_t. For this fucntion, four background classes are used; $W b\bar{b}$, $t\bar{t}$, $W c\bar{c}/W c$ and mistags. These histograms are normalized to unit area such that $\sum_{j=1}^{n_i} f_{ijk} = 1$. The likelihood function calculated by evaluating which bin a given event falls in the distribution of variable i.

$$p_{ik} = \frac{f_{ijk}}{\sum_{m=1}^{5} f_{ijk}}$$

This value is used to compute

$$L_{sig} = \frac{\prod_{i=1}^{n_{var}} p_{i,sig}}{\sum_{m=1}^{5} \prod_{i=1}^{n_{var}} p_{im}}.$$

The likelihood method dose not consider the correlations between the input variables, but this method is easy to put a number of differnt configurations of the input variables compared to other multivariate techniques at CDF.

In this analysis, two likelihood functions are calculated for two-jet events and three-jet events; the input variables are chosen separately to optimize the likelihod function for each 2jet and 3jet events.

5.2   Input variables

The input variables for likelihood function are considered by using angular and energy related features of produced events(the lepton, the neutrino(missing transverse energy), b tagged jet or untagged jet) as well as the MadGraph matrix elements. There are the input variables of $Q \cdot \eta$, M_{jj}, $cos\theta_{lq}$, KIT Flavor Separator. For only 2jet, H_T, $\log(ME_{t-chan})$, χ_t^2 are added to the input variables. With the presence of a third jet in each event, a larger number of reconstructed

61
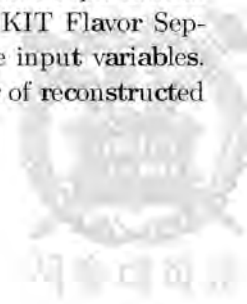
varaibles is possible. Therefore, more variables are considered when constructing the 3-|et bin likelihood function. For only 3|et, $M_{l\nu b}$, the number of b-tagged |ets, the smallest 4 R of any two |ets, P_T of the lowest momentum |et, P_T of the |et chosen to be the b from top decay, η of the reconstruceted W boson are added to the input variables.

• $Q \times \eta$, the product of the charge of the lepton and the pseudorapidity of the light quark
 This gives the asymetry for t-channel signal events, while it is central for backgrounds. The initial state u-quark in the proton which is composed of two u-quark and a d-quark mostly contributes the single-top production, while d̄-quark in antiproton gives smaller contribution to that production in t-channel. The light quark which donates the W boson from the initial valence quark travles predominantly in the same direction of the valence quark before interaction, while the b quark as a sea quark carries small momentum fraction from initial hadron. Therefore, the light quark |ets mostly moves in proton direction, which means positive pseudorapidity, and the lepton charge determines the the sign of the top quark (Figure 5.1, 5.2).
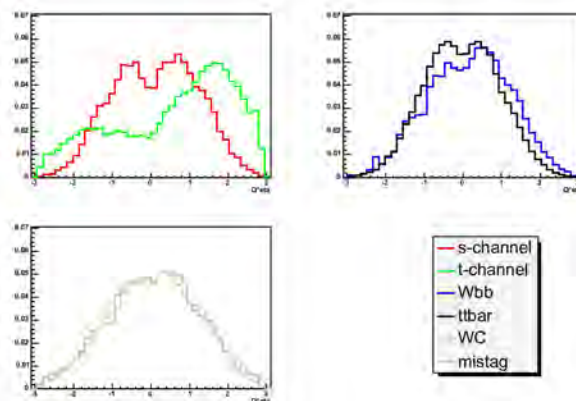
Figure 5.1. $Q \cdot \eta$ of the lepton charge and untagged |et η. input variable in 2|et bin (normalized plots)

62
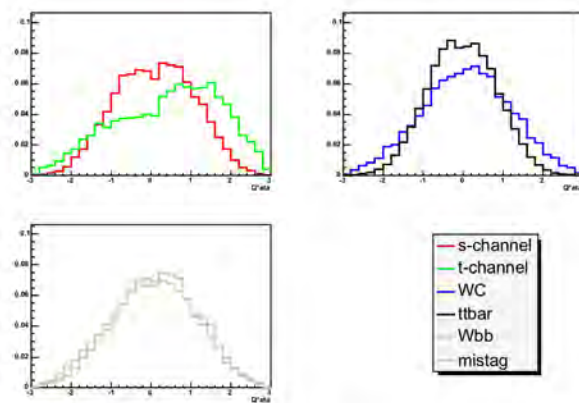
Figure 5.2. $Q \cdot \eta$ of the lepton charge and untagged jet η. input variable in 3 jet bin (normalized plots)

- M_{jj}, the invariant mass of the two jets

For W+jets events, two jets mainly come from the gluon splitting and the invariant mass is lower than single-top siganl and $t\bar{t}$ events. For the diboson processes, the invariant mass of two jets is expected to be the W and Z boson mass (Figure 5.3, 5.4).
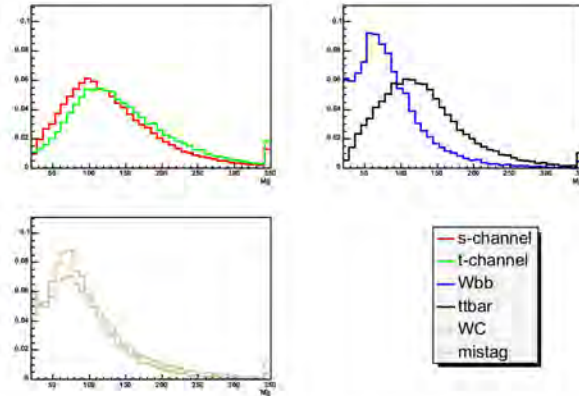
Figure 5.3. The invariant mass of the two jet. input variable in 2jet bin (normalized plots)
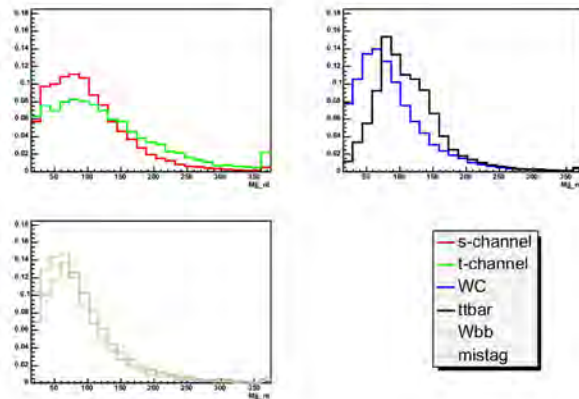
Figure 5.4. The invariant mass of the two jet. input variable in 3jet bin (normalized plots)

64

- $cos\theta_{lq}$, the cosine of the angle between the lepton and the light quark(untagged |et) in the top quark rest frame.

The top spin polarized to the direction of light quark momentum in t-channel single-top events. The top quark decays to the W boson, and W boson decays to the lepton and neutrino satisfying the angular momentum conservation. The lepton momentum is correlated to the top quark spin(that is light quark momentum) and this variable($cos\theta$) contributes to distiguishing t-channel sample from background (Figure 5.5, 5.6).
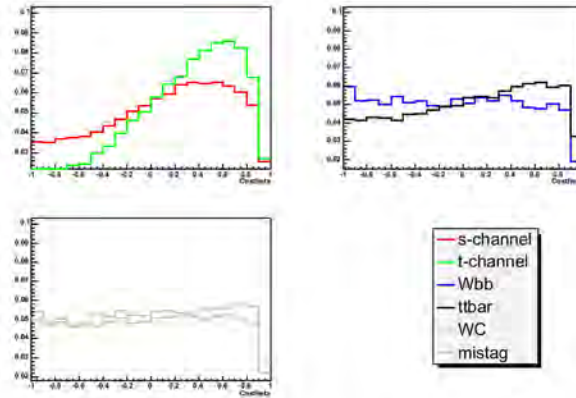
Figure 5.5. $cos\theta_{lq}$. input variable in 2|et bin (normalized plots)
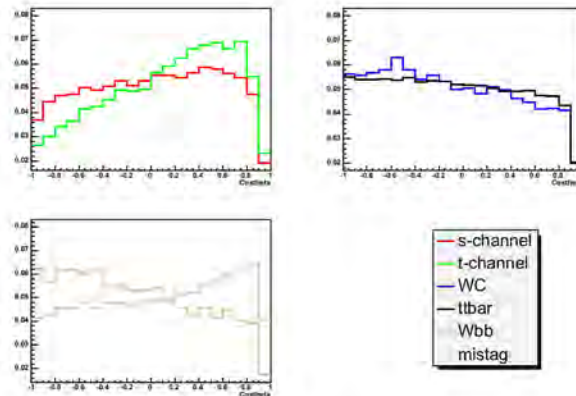
Figure 5.6. $cos\theta_{lq}$. input variable in 3|et bin (normalized plots)

• KIT Flavor Separator , the output of Neural Network for the choice of b-quark |et.

The range of output of NN btagger is from -1 to 1. The outputs of signal, $t\bar{t}$ or W$b\bar{b}$ events containing b-quark go to the +1 and the ouputs of W$c(\bar{c})$ and mistags go to the -1 (Figure 5.7, 5.8).
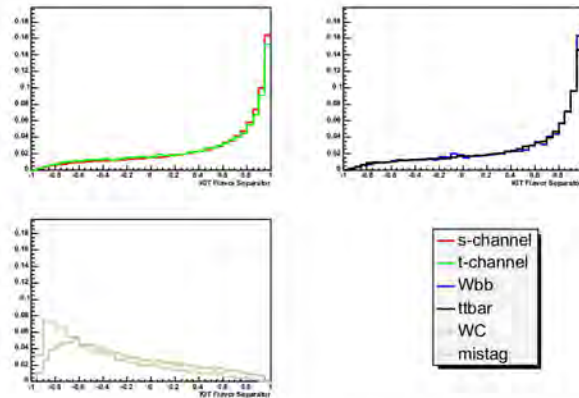
Figure 5.7. NN-btagger. input variable in 2|et bin (normalized plots)
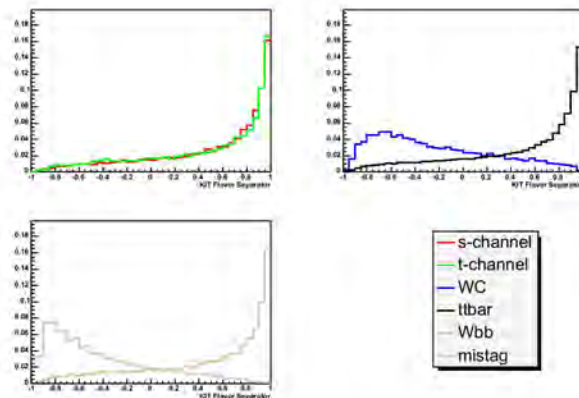
Figure 5.8. NN-btagger. input variable in 3|et bin (normalized plots)

66

- H_T, the scalar sum of the transverse energies of the lepton, and the missing transverse energy, and the two highest momentum |ets.

The peak of signal events is lower than $t\bar{t}$ events and higher than other backgrouns (Figure 5.9).
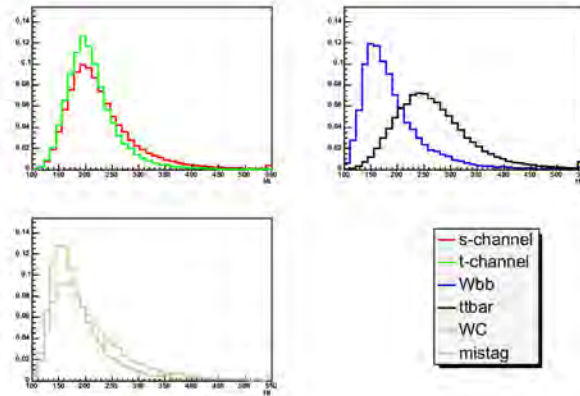
Figure 5.9. H_T. The scalar sum of transverse energies of the two |ets, the lepton, and the missing transeverse energy. input variable in 2|et bin (normalized plots)

- $\log(ME_{t-chan})$, is the log of the MadGraph matrix element

The MadGraph matrix element is computed using the constrained four-vectors of the b-quark, the lepton and the neutrino, assuming t-channel signal production. The matrix element was a weighted average of the $ub \rightarrow dt$ matrix element with weight 2/3, and the same matrix element with lepton sign reversed with weight 1/3 in order to simulate $d\bar{b} \rightarrow u\bar{t}$. This increases the signal-like behavior of the t-channel signal, but also increases the background prediction. The overall sensitivity of the analysis was improved and this can be understood as the optimization of the search for the larger subclass of the signal (Figure 5.10).

- χ^2_t, the output from the kinematic solver for the t-channel selection algorithms

The kinematic constraint is the top-quark mass($M_{l\nu b}$ / M_t) and W boson mass($M_{l\nu}$ / M_W). This constraint allows a solution for the b-|et's energy and improve the reconstruction of signal events, worsen the reconstruction of background events. Therefore, the kinematic solver helps to separate the signal events from the backgrounds (Figure 5.11).

67
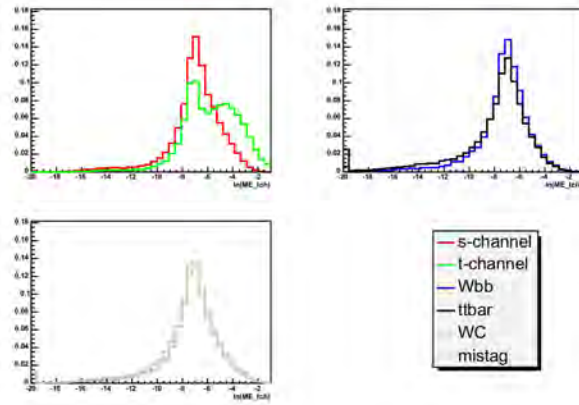
Figure 5.10. Matrix Element assuming t-channel signal production. input variable in 2|et bin (normalized plots)
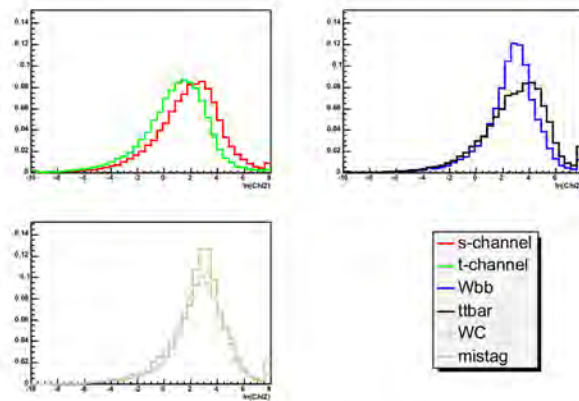
Figure 5.11. χ^2 output from the kinematic solver. input variable in 2|et bin (normalized plots)

• $M_{l\nu b}$, the reconstructed top-quark mass of lepton, neutrino, and b-quark jet
The invariant mass peak(around 170 GeV) of signal events is higher value than
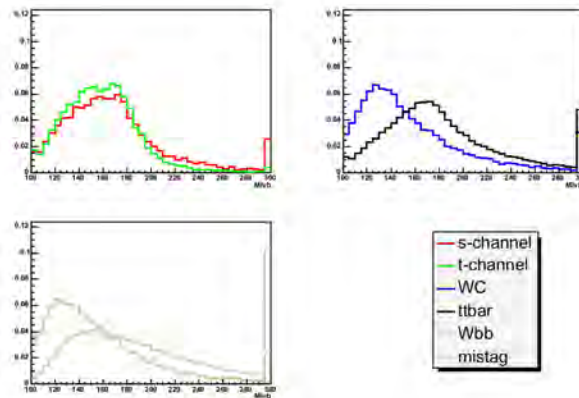it of backgrounds events (Figure 5.12).

Figure 5.12. Reconstructed top mass. input variable in 3jet bin (normalized plots)

• The number of b-tagged jets
This variable can differentiate sample of small b jet from larger number of b jet samples (Figure 5.13).
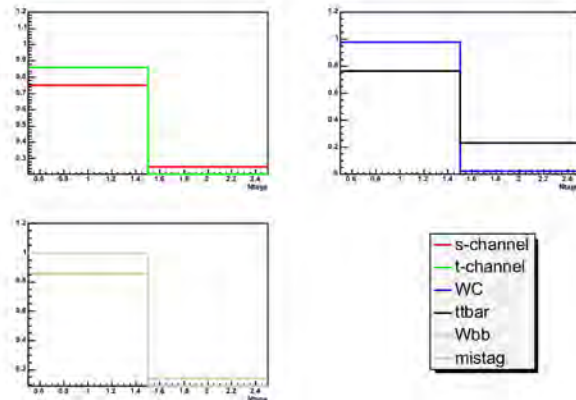
Figure 5.13. The number of b-tagged jets. input variable in 3jet bin (normalized plots)

69

• The smallest 4 R of any two |ets ; This is a discriminant variable from the properties of relations between two |ets. For example, the angle of two |ets came from gluon is different from the angle of other pair of |ets (Figure 5.14).
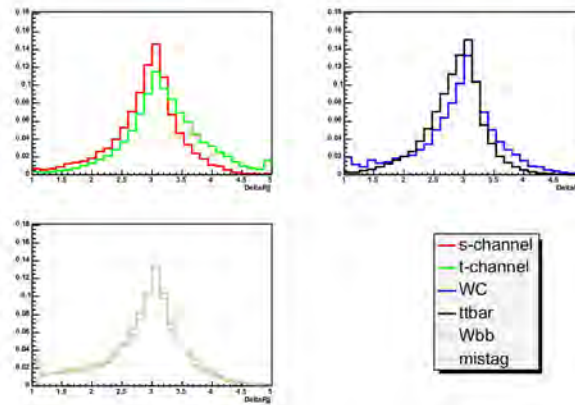
Figure 5.14. The smallest 4 R of any two |et. input variable in 3|et bin (normalized plots)

• P_T of the lowest momentum |et ; The backgrounds such as W b$\bar{b}$, W c(c) and mistag have lower momentum distribution than signal and t$\bar{t}$ (Figure 5.15).
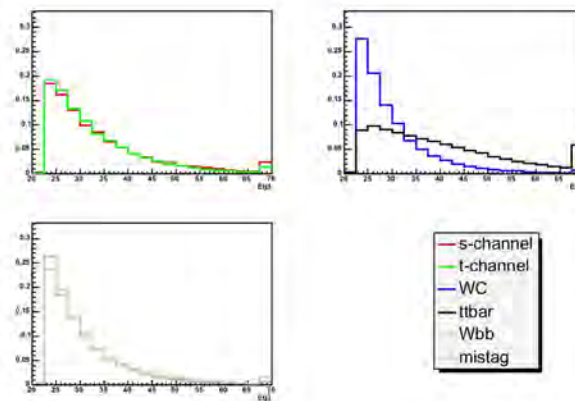
Figure 5.15. P_t of the lowest momentum |et. input variable in 3|et bin (normalized plots)

70

• P$_T$ of the |et chosen to be the b from top decay ; This is also similar situation with previous varaible (Figure 5.16).
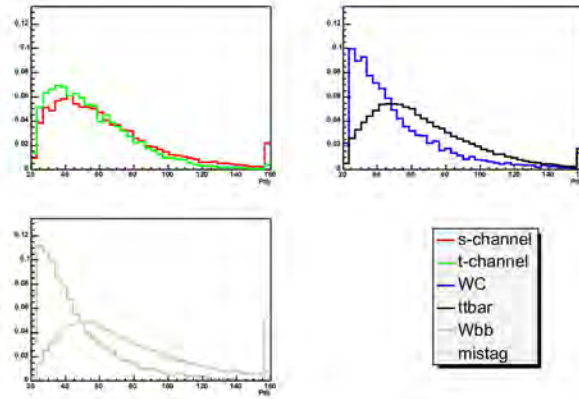
Figure 5.16. P$_t$ of the |et chosen to be the b from top decay. input variable in 3|et bin (normalized plots)

• η of the reconstruceted W boson (Figure 5.17).
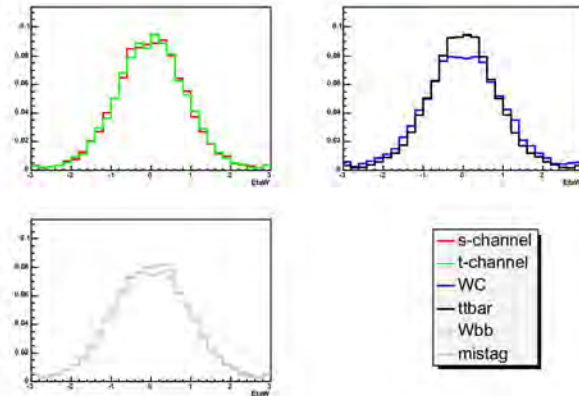
Figure 5.17. η of W. input variable in 3|et bin (normalized plots)

It is difficult to distinguish signal from background by using only one input variable. So, we combined proper input variables, they are already mentioned, to one likelihood function discriminant. Figure 5.18$\sim$ 5.24 show the stacked plots(Data and MC are compared) of input variables.

71
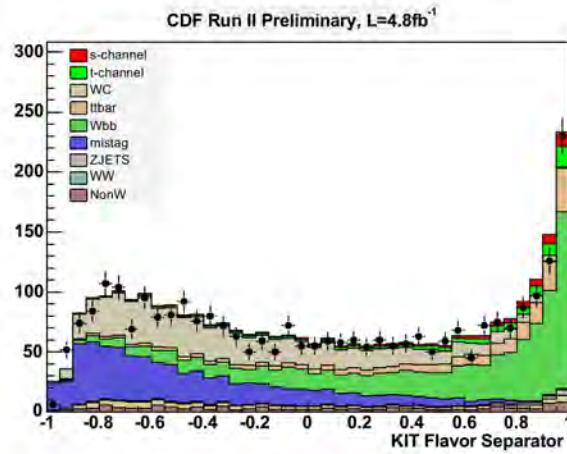
Figure 5.18. NN-btagger. input variable in 2|et bin (Data and MC are compared)
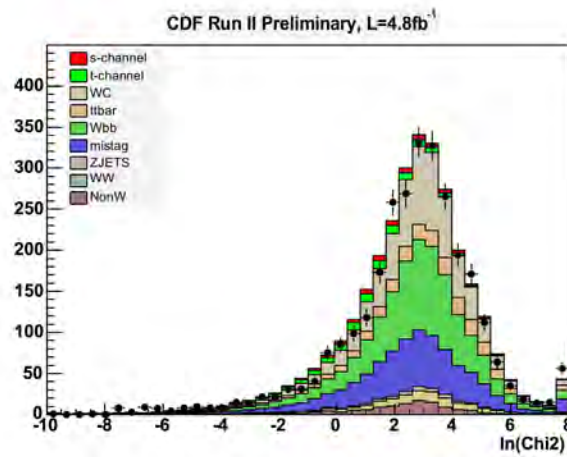
Figure 5.19. χ^2 output from the kinematic solver. input variable in 2|et bin (Data and MC are compared)

72
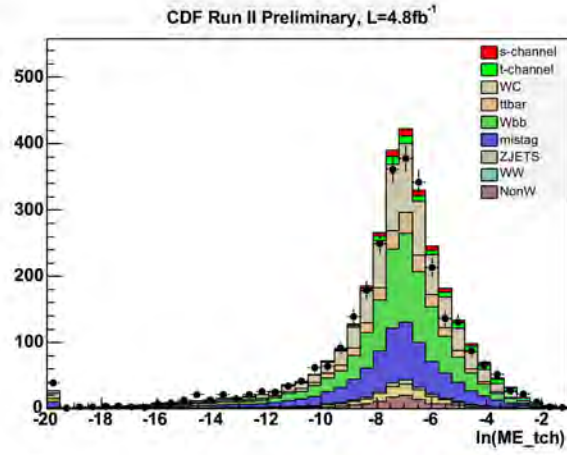
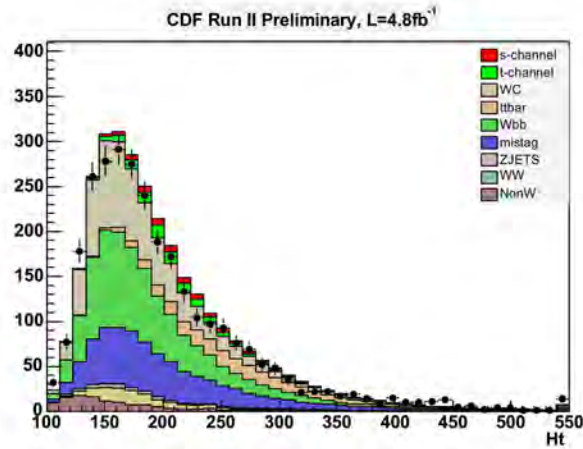Figure 5.20. $\log(M E_{t-ch})$. Output from the kinematic solver. input variable in 2|et bin (Data and MC are compared)

Figure 5.21. H_T. The scalar sum of transverse energies of the two |ets, the lepton, and the missing transeverse energy. input variable in 2|et bin (Data and MC are compared)
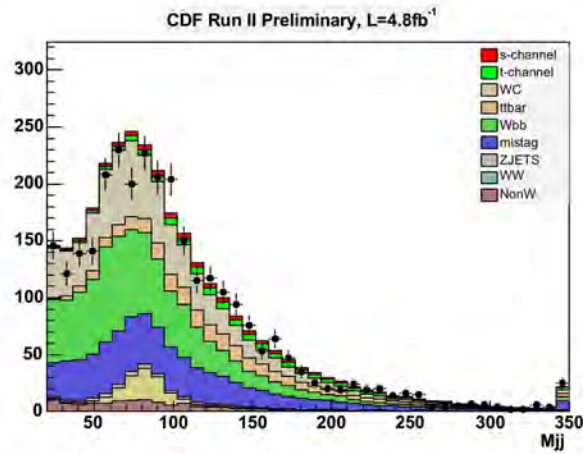
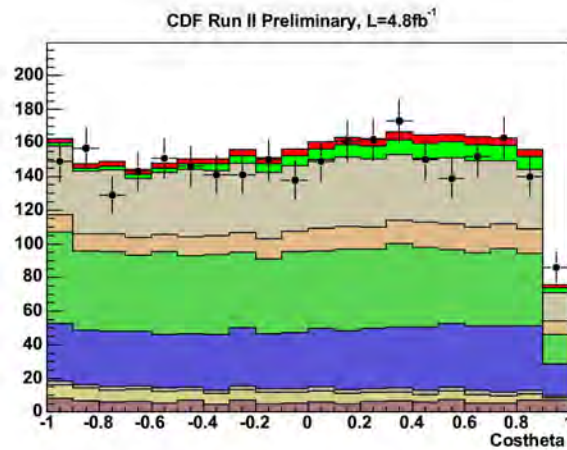Figure 5.22. The invariant mass of the two |et. input variable in 2|et bin (Data and MC are compared)

Figure 5.23. $cos\theta_{lq}$. input variable in 2|et bin (Data and MC are compared)

74

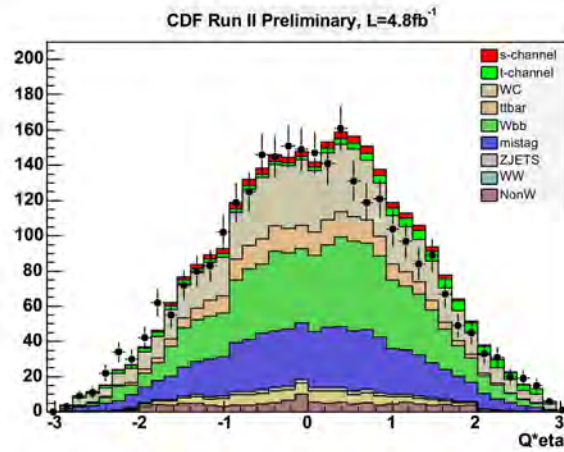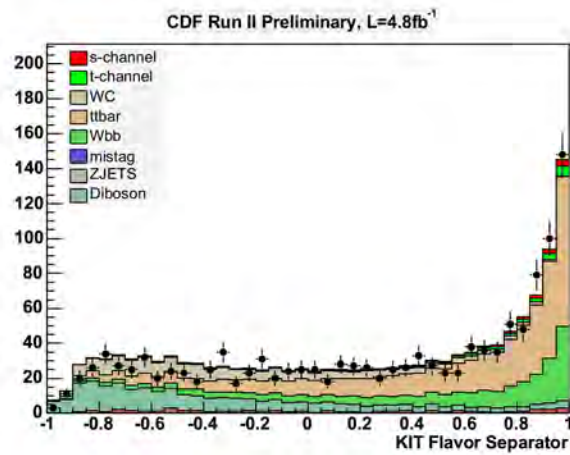Figure 5.24. Q · η of thelepton charge and untagged |et η. input variable in 2|et bin (Data and MC are compared)

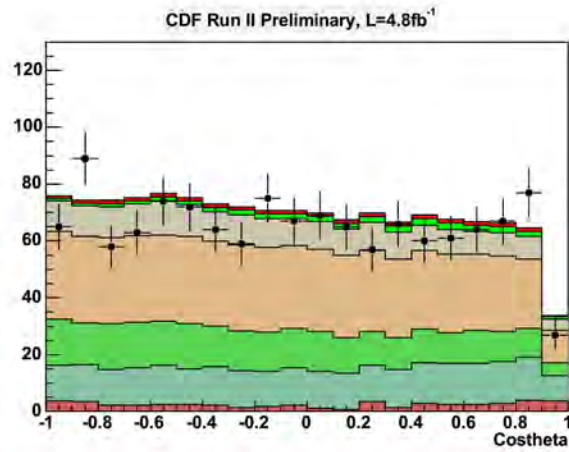Figure 5.25. NN-btagger. input variable in 3|et bin (Data and MC are compared)

75

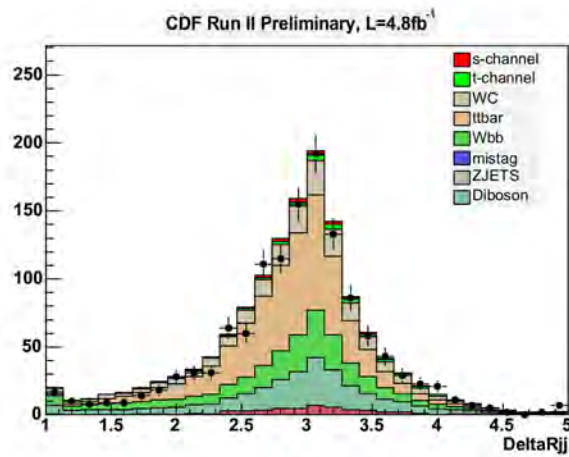Figure 5.26. $cos\theta_{lq}$. input variable in 3|et bin (Data and MC are compared)

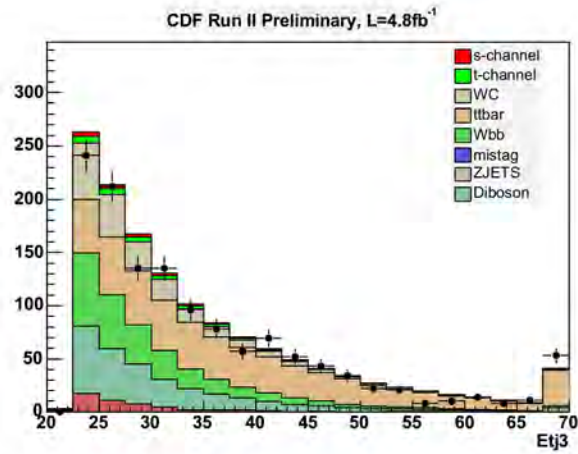Figure 5.27. The smallest 4 R of any two |et. input variable in 3|et bin (Data and MC are compared)

76

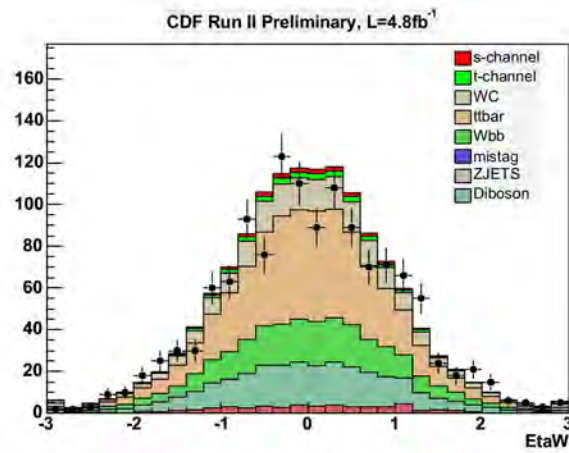Figure 5.28. Lowest Et of jet. input variable in 3jet bin (Data and MC are compared)

Figure 5.29. η of W. input variable in 3jet bin (Data and MC are compared)

77

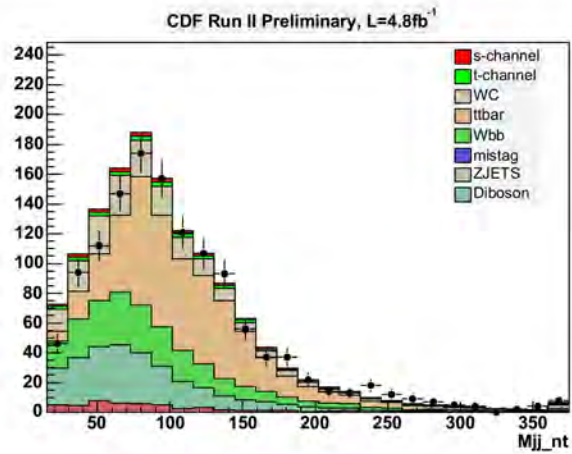Figure 5.30. Two jets not chosen to be the b from top. input variable in 3 jet bin (Data and MC are compared)
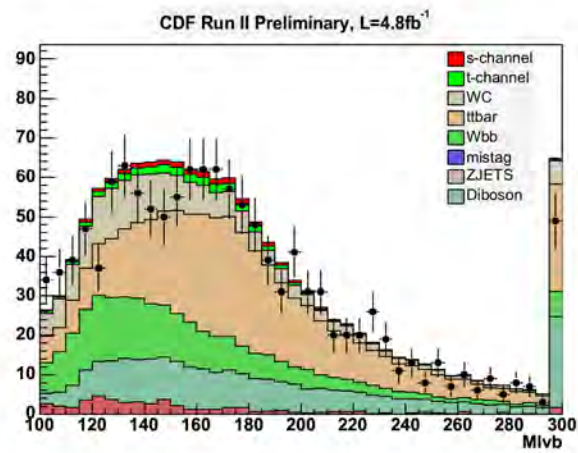
Figure 5.31. Reconstructed top mass. input variable in 3 jet bin (Data and MC are compared)
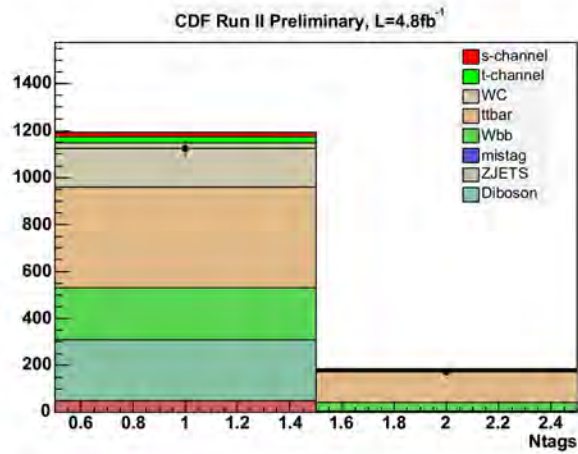
Figure 5.32. The number of b-tagged jets. input variable in 3jet bin (Data and MC are compared)
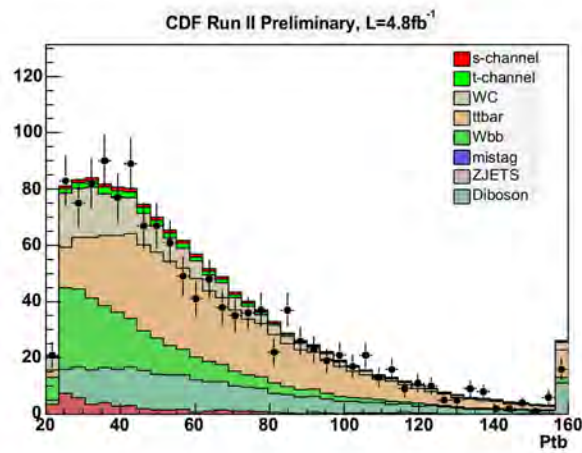

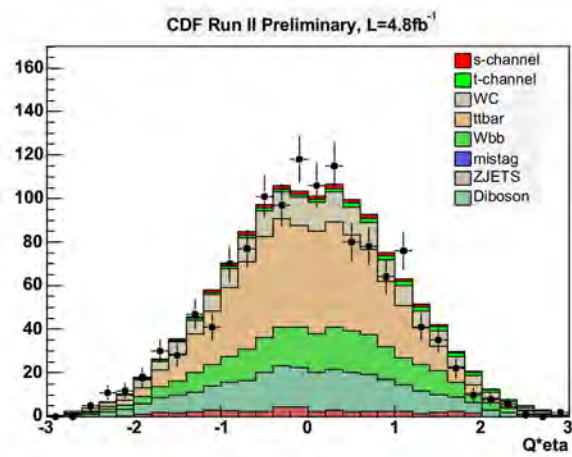Figure 5.33. P_t of the lowest momentum jet. input variable in 3jet bin (Data and MC are compared)

79

Figure 5.34. $Q \cdot \eta$ of thelepton charge and untagged |et η. input variable in 3|et bin (Data and MC are compared)

80

5.3   Likelihood Function

The likelihood functions created from input variables are used to measure the single-top cross-section. Figure [5.35], [5.36] show the likelihood function in 2|et and 3|et bin for comparison of MC and data. The right plots are the events of L > 0.8. For 2|et events of the region L > 0.8, single-top is 41%, Wbb is 29%, Wcc/Wc is 19% and other backgrounds(nonW+Diboson+Z|ets+t$\bar{\text{t}}$) are 11%. For 3|et events of the region L > 0.8, single-top is 19%, Wbb is 28%, Wcc/Wc is 9%, tt is 31% and other backgrounds(nonW+Diboson+Z|ets) are 13%. Therefore, we can see that single-top signal has more portion in the high likelihood bin about 40% for 2|et and about 20% for 3|et events.
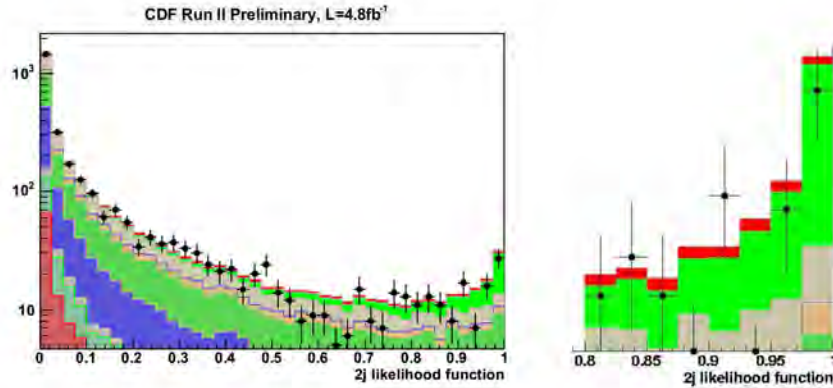

Figure 5.35. 2|et bin t-channel Likelihood function shown on log scale(left plot) and Likelihood function for L >0.8(left plot)
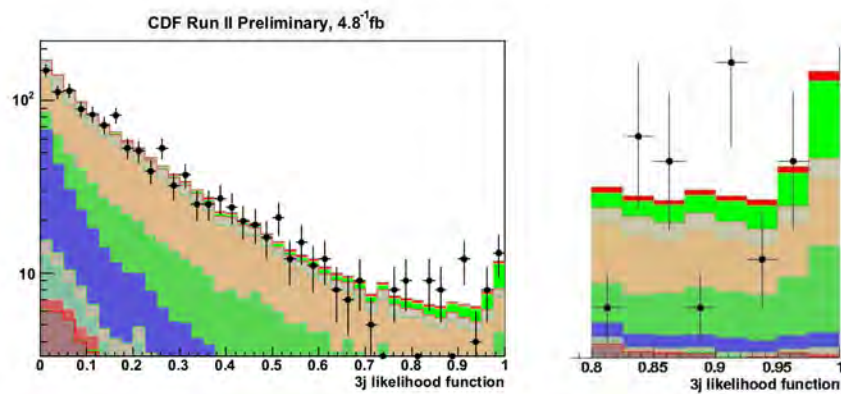
81

Figure 5.36. 3|et bin t-channel Likelihood function shown on log scale(right plot) and Likelihood function for L >0.8(left plot)

82

Chapter 6

Extraction of Signal

The likelihood distiribution(at previous chapter) combined various input templates is applied to the fit code. For fitting the cross section , Maximum-likelihood technique are used. The fitted value is the fraction of the measured cross section in the predicted cross section. The two dimentional fit is done for testing Wtb coupling .

For the degree of evidende of single-top production, p-value is calculated. From this p-value, we defined the evidence(3σ) or observed events(5σ). In the single-top group of CDF, we performed the observaion of single-top production at 3.2f b^{-1} at 5σ level.

6.1   Maximum Likelihood Fit

To measure the cross-section of single-top production, a binned likelihood fit to the multivariate likelihood is performed using a Baysian technique [46] [47].

Given N channels (from histogram bins or number of |ets..), and n_k observed events in the kth channel, k / 1,2,...,N, the Poisson Probability of obtaining the observed result is

$$\prod_{k=1}^{N} \frac{e^{-(s\epsilon_k + b_k)}(s\epsilon_k + \mathbf{b_k})^{n_k}}{n_k \rightarrow}$$

where s represents the parameter of interest (the cross section) and ϵ_k and $\mathbf{b_k}$ are the acceptance and expected background for the kth channel, respectively. All the ϵ_k and $\mathbf{b_k}$ have uncertainties and are considered "nuisance parameters".

The |oint nuisance prior is written as

$$\pi(\mathbf{s}) \iiint_{(2N)} \pi(\epsilon_1; \mathbf{b_1}; \cdots; \epsilon_N; \mathbf{b_N}) \left[\prod_{k=1}^{N} \frac{e^{-(s\epsilon_k + b_k)}(s\epsilon_k + \mathbf{b_k})^{n_k}}{n_k \rightarrow} \right] d\epsilon_1 \mathbf{db_1} \cdots d\epsilon_N \mathbf{db_N}$$

83

where 2N marginalization integrals are performed, and $\pi(\mathbf{s})$, the prior for $\mathbf{s}$, is assumed to be independent of the joint nuisance prior. The random M $(\epsilon_1; \mathbf{b}_1; \cdots; \epsilon_N; \mathbf{b}_N)$ vectors are generated.

The marginalized posterior for $\mathbf{s}$ then becomes

$$\mathrm{p}(\mathbf{s}) \propto \frac{1}{\mathrm{N}} \frac{\pi(\mathbf{s})}{\mathrm{M}} \sum_{i=1}^{M} \left[\prod_{k=1}^{N} \frac{\mathrm{e}^{-(s\epsilon_k + b_k)}(s\epsilon_k + \mathbf{b}_k)^{n_k}}{\mathrm{n}_k \to} \right]$$

where the normalization constant N is given by

$$\mathrm{N} \propto \int_0^1 \frac{\pi(\mathbf{s})}{\mathrm{M}} \sum_{i=1}^{M} \left[\prod_{k=1}^{N} \frac{\mathrm{e}^{-(s\epsilon_k + b_k)}(s\epsilon_k + \mathbf{b}_k)^{n_k}}{\mathrm{n}_k \to} \right] \mathrm{d}\mathbf{s}$$

In this analysis, the following likelihood function is used.

$$\mathrm{L} \propto \prod_{k=1}^{nbins} \frac{\mathrm{e}^{-\mu_k}\mu_k^{n_k}}{\mathrm{n}_k \to} \cdot \prod_j^{bgs} \mathrm{G}_j(\beta_j | 4\ _j) \cdot \prod_i^{sys} \mathrm{G}_i(\delta_i)$$

where μ_k is given by,

$$\mu_k \propto \sum_j^{sig\&bg} \beta_k \cdot \sum_i^{sys} [1 + |\delta_i| \cdot (\epsilon_{ji+} \mathrm{H}(\delta_i) + \epsilon_{ji-} \mathrm{H}(-\delta_i))]$$

$$\cdot \alpha_{jk} \cdot \sum_i^{sys} [1 + |\delta_i| \cdot (\mathrm{k}_{jik+} \mathrm{H}(\delta_i) + \mathrm{k}_{jik-} \mathrm{H}(-\delta_i))]$$

The fitted parameter is $\beta_j \propto \sigma_j^{fit}/\sigma_j^{SM}$, ratio of measured cross-section and SM prediction. The shape information is given by α_{jk} in template bin j of process k. The relative strength of a systematic effect for source i is δ_i. The $\epsilon_{ji\pm}$ is the ± 1 σ changes in the rate uncertainty and k_{jik} is for the shape uncertainty.

The Gaussian constraints for the background components with $4\ _j$ is,

$$\mathrm{G}_j(\beta_j | 4\ _j) \propto \frac{1}{\sqrt{2\phi \cdot 4\ _j^2}} \exp(-\frac{1}{2} \cdot (\frac{\beta_j - 1.0}{4})^2)$$

6.2   Background Estimation

The final estimate number of signal and background and observed data are shown in Table 6.1(already shown in chapter 4). After selection of events, the expected number of signal events is 15% of the backgrounds in 2jet and 24% in 3jet. The W$b\bar{b}$, W$c\bar{c}$, and mistag are dominant backgrounds and $t\bar{t}$ occupied larger portion in 3jet than 2jet. These estimated numbers are used to the likelihood fit.

84

	2jets	3jets
s-channel	72.7 ± 10.5	23.2 ± 3.3
t-channel	111.4 ± 16.5	32.4 ± 4.8
Wbb	906.9 ± 273.4	259.5 ± 78.4
Wcc+Wc	755.25 ± 232.9	192.1 ± 59.2
Mistag	681.6 ± 95.4	195.3 ± 27.9
ttbar	246.75 ± 35.8	559.65 ± 81
Z+jets	41.85 ± 6.4	16.2 ± 2.4
Diboson	117.45 ± 12.15	37.1 ± 3.9
non-W	123.3 ± 49.35	49.8 ± 19.9
Total Signal	184.1 ± 27.0	55.6 ± 8.1
Total Prediction	3057 ± 519.3	1365.3 ± 162.4
Observed in Data	2920	1300

Table 6.1. Data and Background for single-top production with 4.8 fb^{-1}

6.3 Systematic Uncertainties

Source of systematic uncertainty are incorporated in this analysis as nuisance parameters in the likelihood function, conform with a fully Bayesian treatment. Most systematic uncertainties, such as the uncertainty on the jet-energy-scale, can affect the analysis in two ways. first, since we require the jets to have $E_T > 15 GeV$, a change in the jet-energy-scale affects the event detection efficiency . Meanwhile, the shape of the H_T distribution, which depends also on jet energies, will also change(we call this the 'shape uncertainty'). We include all sources of systematic uncertainty into the likelihood and take the correlation between normalization and shape uncertainties for a given source into account.

6.3.1 Rate Systematic Uncertainties

Normalization uncertainties are estimated by recalculating the event detection efficiency using Monte Carlo samples altered due to a specific systematic effect. The normalization uncertainty is the difference between the systematically shifted event detection efficiency and the default event detection efficiency. The effect of the uncertainty in the jet energy scale is evaluated by applying jet-energy corrections that describe $\pm\sigma$ variations to the default correction factor. For the s-channel, both variations show a lower event detection efficiency(both relative changes are negative). This is an artifact of the $M_{l\nu b}$-window cyt. Increasing(decreasing) the jet energy scale factor by the $+1\sigma(-1\sigma)$ variation, shifts the $M_{l\nu b}$ distribution to higher(lower) values. Systematic uncertainties due to the

85

modeling of ISR and FSR was increased and decreased in the parton showering to represent $\pm\sigma$ variations.

Jet Energy Scale(JES) The uncertainties in the jet energy scale are estimated by processing all events in Monte Carlo samples with the jet energy scale varied with $\pm 1\sigma$. The correction of jet energy is to dertermine the energy correction to scale the measured energy of the jet energy back to the energy of final state particle level jet. Also, there are additional corrections to the measured jet energy to the parent parton energy. The jet energy corrections are performed through the multi-levels; detector non-uniformity, multiple interactions, not assigned jet outside of the jet cone and so on. The original parton transverse energy can be estimated as follows [48].

$$\mathrm{p}_T^{parton} \ / \ (\mathrm{p}_T^{jet} \times \mathrm{C}_\eta - \mathrm{C}_{MI}) \times \mathrm{C}_{Abs} - \mathrm{C}_{UE} + \mathrm{C}_{OOC} \ / \ \mathrm{p}_T^{particle} - \mathrm{C}_{UE} + \mathrm{C}_{OOC}$$

where p_T^{parton} is the transverse momentum of the parent parton, p_T^{jet} is the transverse momentum measured in the calorimeter jet and $\mathrm{p}_T^{particle}$ is the particle jet momentum.

- C_η . "η-dependent" correction for homogeneous response.
- C_{MI} . "Multiple Interaction" correction for subtracting the jet from multiple $\mathrm{p}\bar{\mathrm{p}}$ interactions.
- C_{Abs} . "Absolute" correction of the calorimeter response to the momentum of the particle jet.
- C_{UE} and C_{OOC} . "Underlying Event" and "Out-Of-Cone" corrections for parton radiation and hadronization effects due to the finite size of the jet cone algorithm.

All corrections are determined as the transverse momentum of jet but they apply to all components of the four-momentum of the jet. The uncertainty of jet energy scale is about 3%($\mathrm{P}_T >$70GeV) and 3~9($\mathrm{P}_T <$70GeV) in Figure 6.1. The systematic error from JES about single-top cross section is about +8/-11%.

Heavy Flavor Fraction in W+jets The uncertainty about the prediction of W$b\bar{b}$, W$c\bar{c}$, Wc mainly comes from Heavy flavor fraction(k-factor).

The heavy flavor(HF) content of the W+jets sample is calculated by [35] [36].

$$\mathrm{N}_{W+HF}^{tag} \ / \ \mathrm{N}_{W+jets,data}^{pretag} \times \mathrm{F}_{HF} \times \epsilon_{tag}^{W+HF} \times \mathrm{KF}$$

where $\mathrm{F}_{HF} \ / \ \mathrm{N}_{b,MC}^{W+Jets}/\mathrm{N}_{jets,MC}^{W+Jets}$ is the heavy flavor fraction of the W+jets sample, ϵ_{tag}^{W+HF} is the tagging efficiency in the W+HF Monte Carlo sample, $\mathrm{N}_{W+jets,data}^{pretag}$ is the number of pretag W+jets events in data, and KF is the calibration factor(or K-factor) of the heavy flavor fraction(F_{HF}). The K-factor is
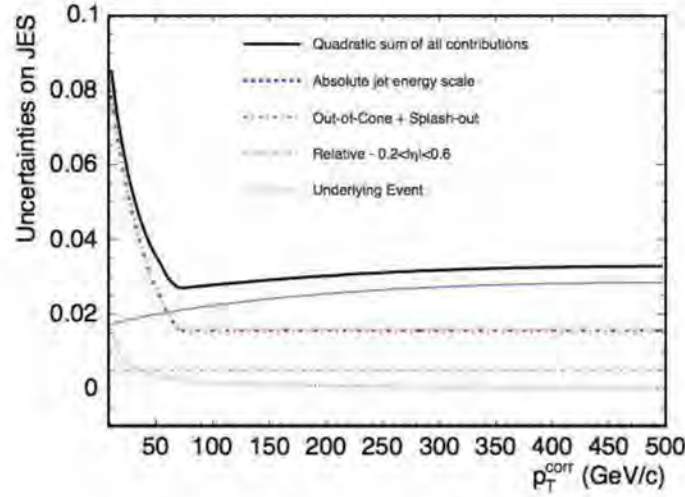
86

Figure 6.1. The Uncertainty as a function of the corrected Jet P_T in $0.2 < \eta < 0.6$

defined as

$$ KF \ / \ \frac{F_{j,data}^{b,events}}{F_{j,MC}^{b,events}} $$

where $F_{j,data}^{b,events} \ / \ N_{b,data}/N_{jets,data}$.

The prediction of the $W b\bar{b}$, $W c\bar{c}$, and Wc fractions in the $W+2$ Jets and $W+3$ Jets samples are extrapolation from the $W+1$ Jet sample. The ALPGEN underpredicts the $W b\bar{b}$, $W c\bar{c}$ fractions in the $W+1$ Jet sample by a factor of 1.4 ± 0.4 [37] (Ideally, it should be unity); this effect comes from the incorrect model of gluon splitting in the MC and Higher order effects. The template fits to the $W+1$ Jet bin data using KNN flavor separator are shown in Figure 6.2. The Wc prediction from ALPGEN is compared to measurement [38] and does not require scaling, but uncorrelated uncertainty is assigned to the Wc prediction. The Uncertainties from KF is about 30% and the systematic error about single-top cross section is +12/-12% for Wbb+Wcc and +1/-9% for Wc.

Luminosity   The uncertainty($\pm 6\%$) of integrated luminosity comes from the inelastic $p\bar{p}$ cross section and the acceptance of luminosity monitor.

Luminosity is measured by the Cherenkov Luminosity Counters(CLC) [49] [50]. The CLC measure the average number of interactions per bunch crossing(μ) and
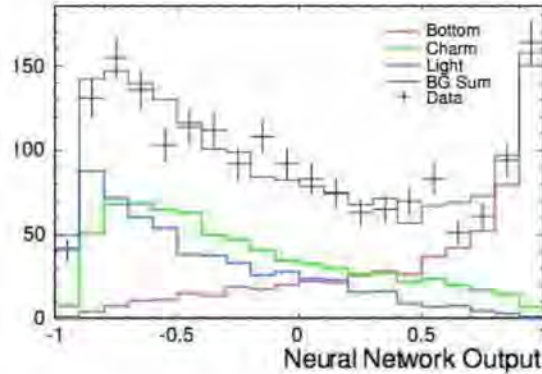
87

Figure 6.2. Template fits to the W+1|et bin data to extract the fraction of tagged |ets using KNN flavor separator

the instantaneous luminosity is calculated by.

$$L \ / \ \frac{\mu \cdot f_{BC}}{\sigma_{tot}}$$

where the σ_{tot} is the total $p\bar{p}$ cross-section, f_{BC} is the rate of bunch crossings. The uncertainty by luminosity monitor comes from following effects; Geometry, Generator, Beam Position, CLC simulation. SPP(single particle peak) calibration, Acceptance stability, Online $\rightarrow$ Offline transfer, Backgrounds (Table 6.2). Uncertainty of luminosity is 6% and systematic error is +12/-12%.

Theoretical Cross Sections   The signal and background Monte Carlos underpredict the total cross sections, so the predictions need to be scaled to the NLO theoretical models. The effects of the top quark mass is separated out from the sources of uncertainty affecting the theoretical predictions. Figure 6.3 shows the cross-section of $t\bar{t}$ and its uncertainties versus top mass. The uncertainty of theoretical $t\bar{t}$ cross-section at top mass 175 GeV is about 12%. The systematic error about single-top cross section is +1/-9%.

Initial/Final State Radiation   The ISR [40] and FSR [40] systematic uncertainties are estimated by altering samples which are more or less initial-state radiation(ISR) and final-state radiation(FSR). The effects of variations of ISR and FSR are taken to be correlated. Figure 6.4 shows P_t distribution of the dileptons for ISRmore and ISRless [39]. The Uncertinty of ISR and FSR is 15% and systematic error is +5/-10%.

88

Sytematic Effect	Updated Uncertainty
Geometry	3%
Generator	2 %
Beam Position	< 1 %
CLC simulation	1%
SPP calibration	< 1 %
Acceptance stability	1%
Online → Offline transfer	negligible
Backgrounds	< 1 %
Statistical uncertainty	negligible
Luminosity method	negligible
Total by CLC measurement	< 4.2 %
Inelastic p$\bar{\text{p}}$ cross section	4%

Table 6.2. Uncertainty of Luminosity from Various Sources
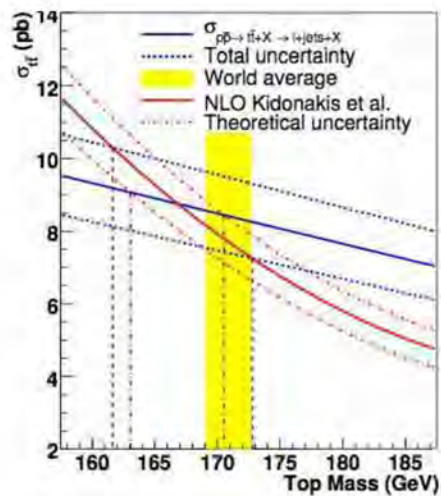
Figure 6.3. The cross-section and its uncertainty of t$\bar{\text{t}}$ cross section versus top mass

89
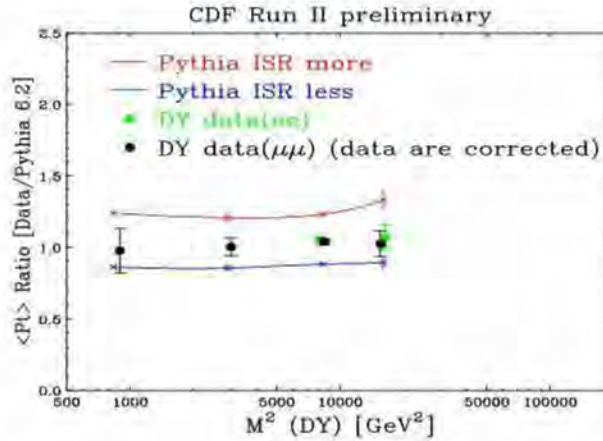
Figure 6.4. The Uncertianty of Initial State Radiation

Accecptance and Efficiency Scale Factors The mismodeling of the lepton identification [33] and the b-tagging efficiency [34] affects the predicted rates of signal and backgrounds. The uncertainties are considered by the scale factors for correction between the simulation and the data.

Parton Distribution Function The PDF parameterization systematic was studied by re-weighted single top and $t\bar{t}$ events with weights associated with default PDF CTEQ5L [32], and PDFs from MRST72, MRST75 and CTEQ6M. CTEQ6M is 20 orthogonal CTEQ PDF sets with up and down for 90%, MRST72 is MRST PDF set with same α_s value as CTEQ5L and MRST75 is MRST PDF set with different α_s value. The uncertainties is calculated by the quadrature of differences between PDF sets. Some compared PDF is shown in Figure 6.5.

The Table 6.3 shows the summary of Systematic rate Uncertainties and Error. The Table 6.4 6.5 shows the systematic rate uncertainties for 2|et and 3|et bin, in percent.

90
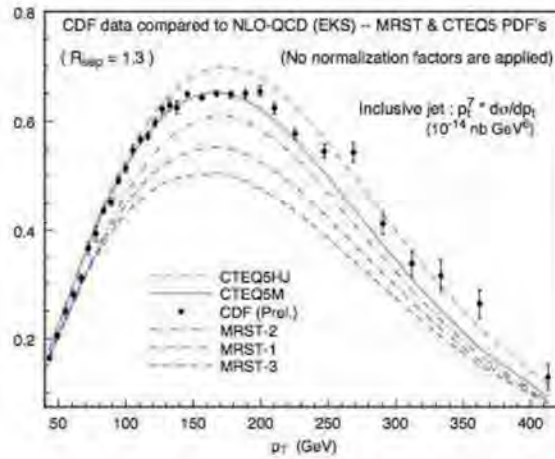
Figure 6.5. The Comparison of the Parton Distribution Functions

Source	Uncertainty	Error
Jet Energy Scale	3%(>70GeV) 3~9%(<70GeV)	+8/-11%
Initial + Final State Radiation	15%	+5/-10%
signal+$t\bar{t}$ nomalization due to PDF	$2 \sim 3$%	+5/-6%
ttbar cross section	12%	+1/-9%
Monte Carlo Generator	5%	+1/-9%
Event Detection Efficiency	$5 \sim 8$%	+7/-11%
Luminosity	6%	+12/-12%
Wbb+Wcc normalization (k/ factor)	30%	+12/-12%
Wc normalization	30%	+1/-9%
Total		+13/-16.2%

Table 6.3. Systematic rate Uncertainties and Error

91

Source	t-channel	s-channel	$t\bar{t}$	W+LF	
JES -/+	-1.1/0.6 s	-0.1/-0.6 s	9.7/-9.3 s	s	
ISR more/less	-0.2/2.8 s	6.7/0.3 s	-7.1/-2.6 s		
FSR more/less	-1.3/4.2 s	0.4/5.9 s	-2.6/-5.1 s		
PDF	-3.5/3.1 s	-1.4/1.7 s	-2.3/1.9 s		
Signal MC model	-2.0/2.0	-1.0/1.0			
Luminosity	-6.0/6.0	-6.0/6.0	-6.0/6.0		
Efficiency	-4.2/4.2	-2.3/2.3	-2.6/2.6		
Cross section (t)	-12.6/12.6	-12.4/12.4			
Cross section (tt)			-12.4/12.4		
m_t(170/180)	6.1/-5.3 s	9.5/-8.0 s	7.8/-8.1 s		
η_{j2}	s	s	s	s	
4 R_{jj}	s	s	s	s	
DataMistags				s	
KIT Flav. Sep.				s	
	Wbb	Wc(c)	Diboson	Z+jets	Non-W
JES -/+	6.9/-7.6 s	7.0/-6.3 s	-2.6/1.7 s	-5.3/5.4 s	
Luminosity			-6.0/6.0	-6.0/6.0	
Efficiency			-9.0/9.0	-8.3/8.3	
Cross section (dib)			-2.0/2.0		
Z+jets rate				-10.8/10.8	
W+QQ k-factor	-30.1/30.1	-13.9/13.9			
W+c k-factor		-16.1/16.1			
η_{j2}	s	s	s	s	
Non-W rate					-40.0/40.0
Non-W Flavor					s

Table 6.4. Systematic rate uncertainties for 2-jet bin. Shape uncertinties are indicated with an "s"

92

Source	t-channel	s-channel	$t\bar{t}$	W+LF	
JES -/+	-9.7/2.5 s	-8.0/8.9 s	4.6/-5.1 s	s	
ISR more/less	-0.5/-4.5 s	-12.6/2.9 s	-5.0/-0.6s		
FSR more/less	-2.5/-0.8 s	-4.8/-6.3 s	-2.3/3.5 s		
PDF	-3.7/3.3 s	-1.5/1.7 s	-2.3/1.9 s		
Signal MC model	-1.5/1.5	-1.9/1.9			
Luminosity	-6.0/6.0	-6.0/6.0	-6.0/6.0		
Efficiency	-4.3/4.3	-3.9/3.9	-4.0/4.0		
Cross section (t)	-12.6/12.6	-12.4/12.4			
Cross section (tt)			-12.4/12.4		
m_t(170/180)	6.4/-6.0 s	11.7/-8.6 s	9.3/-8.6 s		
η_{j2}	s	s	s	s	
4 R_{jj}	s	s	s	s	
DataMistags				s	
KIT Flav. Sep.				s	
	Wbb	**Wc(c)**	Diboson	Z+|ets	Non-W
JES -/+	8.8/-8.8 s	8.3/-7.1 s	-13.0/10.8 s	-10.5/13.6 s	
Luminosity			-6.0/6.0	-6.0/6.0	
Efficiency			-9.0/9.0	-8.0/8.0	
Cross section (dib)			-2.0/2.0		
Z+|ets rate				-10.8/10.8	
W+QQ k-factor	-30.1/30.1	-17.7/17.7			
W+c k-factor		-12.3/12.3			
η_{j2}	s	s	s	s	
Non-W rate					-40.0/40.0
Non-W Flavor					s

Table 6.5. Systematic rate uncertainties for 3-|et bin. Shape uncertinties are indicated with an "s"

93

6.3.2 Shape Systematic Uncertainties

Compared with rate uncertainties, shape systematic uncertainties are considered as shape distortions of the templates for the signals and backgrounds. All shape uncertainties are median smoothed with five bins except the first and last two bins. The bins of ratio historam, which is divided the sytematically varied histogram by the central histogram, are replaced by median of 5 bins(itself and neighboured bins). This prodedure play a role in removing extreme outliers and high frequency noise. The smoothed ratio histograms are then multiplied by the central histograms to obtain the new varied histograms. The shape systematic sources are JES, PDF, ISR/FSR, Jet Flavor Separator Modeling, Mistag Model, Non-W Flavor Composition, Jet η Distribution, Jet 4 R_{jj} Distribution.

Jet Flavor Separator Modeling For verifying tagged b-|et, the neural-network |et flavor separator is used. The predicted shape of the flavor-separator for tagged b |ets is well modeled by the simulation, but the light-flavor sample was found to need a small correction about the NN distribution. The difference between the uncorrected light-falvor Monte Carlo prediction and the data-derived corrected distribution is taken as the shape systematic uncertainty. Because the pure sample of charm |ets can't be derived from the data, the shape template for W+charm |ets is estimated from the difference between the distribution of Monte Carlo simulation and the alterd Monte Carlo distribution by the light-flavor correction.

Mistag Model The untagged data largely consist of W+light falvor |ets, but W$b\bar{b}$, W$c\bar{c}$, t$\bar{t}$, and single top events are also contained. The shape template for mistag model is made from the untagged data weighted by the mistag matrix weights.

Non-W Flavor Composition The neural-network flavor separator distribution is used to fit the flavor fractions in the low-$\not{E}_T$ control samples. The uncertainty in expected flavor composition of the non-W events comes from the limited statistical precision of these fits and the necessity of extrapolating to the higher-$\not{E}_T$ signal region. The central-value estimates are 40% b |ets, 45% c |ets, and 15% light-flavor |ets. A systematic sample uses the variation of the flavor composition. 60% b |ets, 30% c |ets, and 10% light-flavor |ets,

Jet η Distribution The mismodeling of |ets at high $|\eta|$ region is checked with the untagged W+2|ets control sample. This mismodeling affects the analysis relating to one of important input variables, Q $\times$ η. All Monte Carlo samples are weighted by a factor of the pseudorapidity of the second-leading |et in W+2 |et

94

events.

Jet 4 R$_{jj}$ Distribution The uncertainty in the distribution of 4 R of two
jets is similar to jet $|\eta|$ distribution. This angular distribution is mismodeled in
the untagged control sample and the gluon splitting fraction in alpgen may affect
this mismodeling. All Monte Carlo samples are weighted by using the ratio pf
the untagged data to the prediction.

Figure [6.6][6.7] shows JES shape systematic compared plot between central
and systematic sample. ALL shape systematic plots are located in Appendix C.
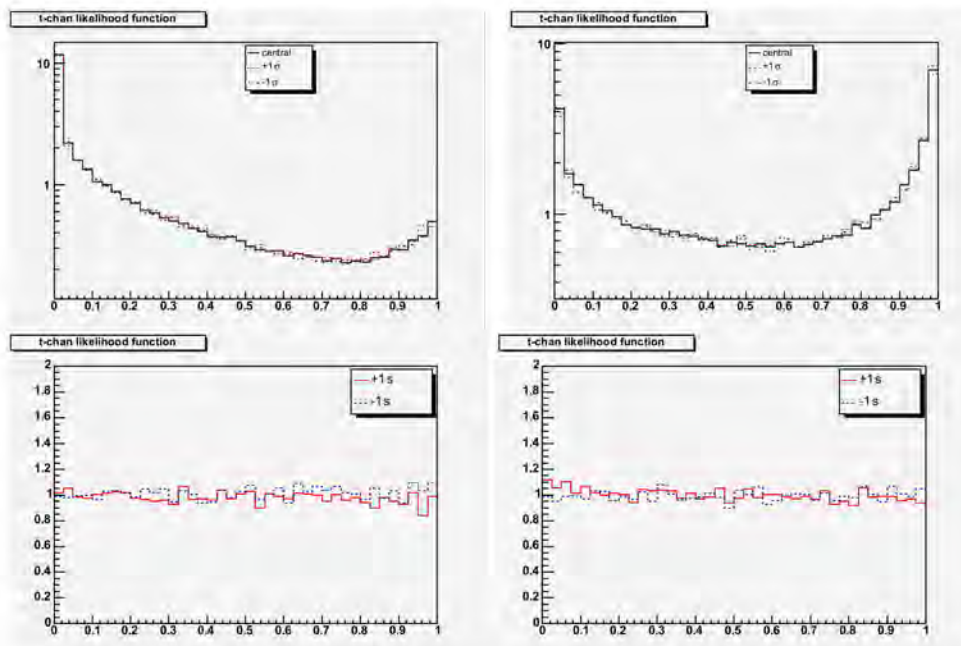
Figure 6.6. JES Shape Systematic Uncertainty(s-/t-channel); compared plot(up)
and ratio plot(down) between central and systematic sample

95
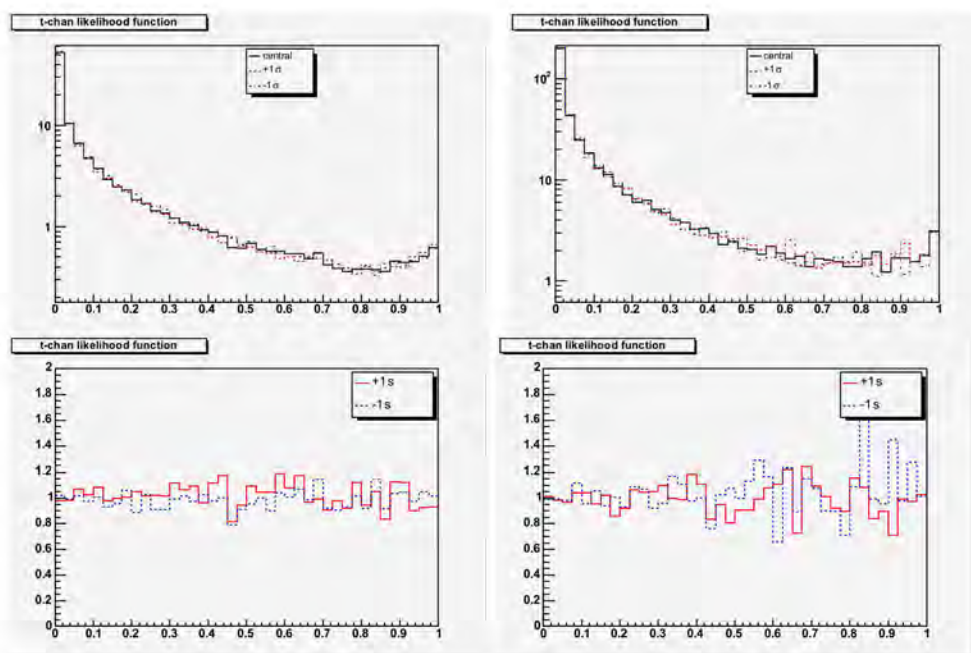
Figure 6.7. JES Shape Systematic Uncertainty(**ttbar**/Wbb); compared plot(up) and **ratio** plot(down) between **central** and systematic sample

6.4 Measurement of Cross Section

The measured cross-section(Fig.[6.8]) is

$$1.83 \; {}^{+0.49(stat)+0.49(sys)}_{-0.43(stat)-0.41(sys)} \; (pb)$$

by using 4.8 f b^{-1} of data collected by the CDF II experiment at the Fermilab Tevatron. we also set the limit(Fig.[6.9]) of

$$V_{tb} > 0.41 \; \text{at } 95\% \text{ CL}.$$
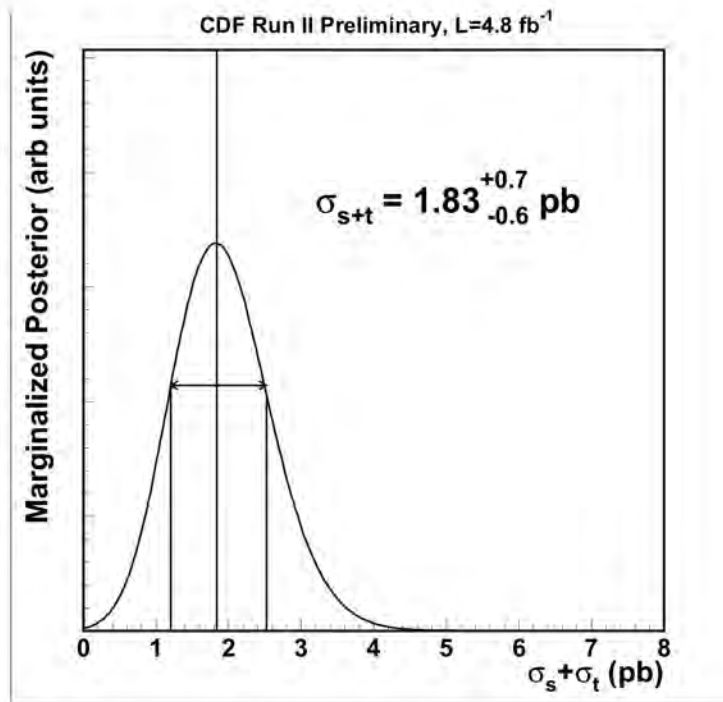
Figure 6.8. Fit for $\sigma_s + \sigma_t$. SM ratio of σ_s/σ_t is assumed. The Baysian posterior, marginalized over nuisance parameter, is shown. The maximum value is the central value of the cross-section fit, and smallest interval enclosing 68% of the integral of the posterior is the quoted interval. The measured result is $1.83 \; {}^{+0.49(stat)+0.49(sys)}_{-0.43(stat)-0.41(sys)} \; (pb)$

97
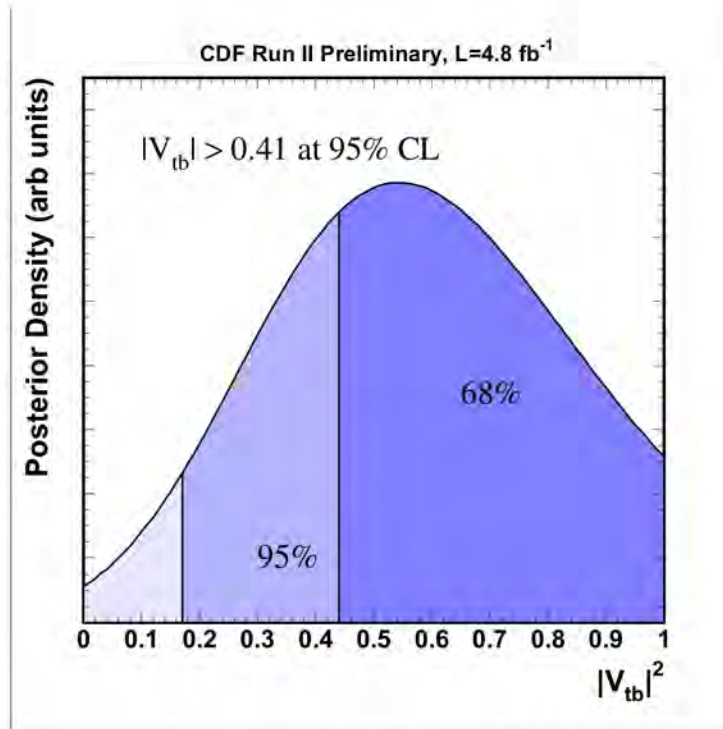
Figure 6.9. Extraction of limits on $|Vtb|^2$ using a Baysian technique. The SM ratio of σ_s/σ_t is assumed. The Baysian posterior, marginalized over nuisance parameter, including the theoretical uncertainty on the single-top cross section and uncertainties due to m_t, is shown. The 68% and 95% confidence intervals are indicated with vertical lines.

98

6.5 Significance

The p-value is the probability of obtaining a test statistic at least as extreme as the one actually observed against the null hypothesis. The data are compared with two hypotheses; test hypothese(signal+backgrounds) assumes single-top quark production and all backgorund processes while null hypothesis(background only) assumes Standard Model processes except single top quark production. We can test what hypothese the data prefer. For obtaining p-value, we calculate Q, the ratio of probability the data in the test(s+b) hypothesis to that in the null(b) hyothesis [43] [44] [45].

$$Q / \frac{P(\text{data}|s+b)}{P(\text{data}|b)} / \prod_{i=1}^{n_{ch}} \prod_{j=1}^{n_i^{bins}} \left[\frac{e^{-(s_{ij}+b_{ij}^s)}(\mathbf{s}_{ij}+\mathbf{b}_{ij}^s)^{d_{ij}}}{d_{ij} \rightarrow} \right] / \left[\frac{e^{-b_{ij}^b}(\mathbf{b}_{ij}^b)^{d_{ij}}}{d_{ij} \rightarrow} \right]$$

The degree of evidence is quantified using pseudoexperiments. One set of pseudoexperiment is performed assuming test hypothese and the other assuming null hypothese. The pseudodata are made from Poisson random distribution with means of the sum of the backgrounds or signal+backgrounds, depending on the hypothesis.

Then the p-value is calculated as the probability of $-2\ln Q < -2\ln Q_{obs}$, assuming the null hypothesis. The measured p-value correspoding the observed data is 9.07×10^{-3}.

The sensitivity of the analysis is computed as the median expected p-value assuming a signal is truly present. The median -2lnQ is extracted from the test hypothesis, and the integral of the null distribution of -2lnQ to the left of this median value is the median expected p-value. The value thus obtained is 2.58×10^{-5}, correspoding to 4.05σ using $3.2f\,b^{-1}$.

99
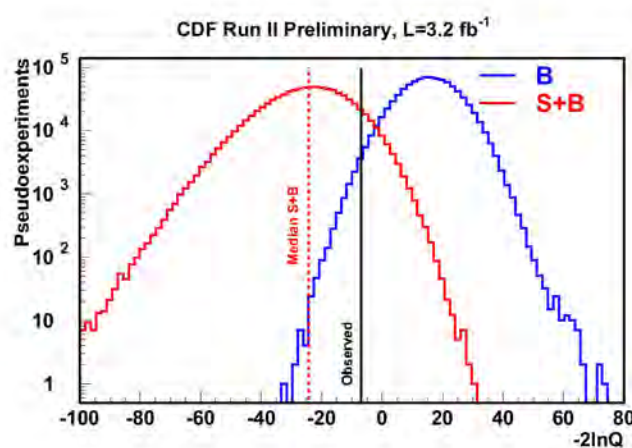
Figure 6.10. Plot of -2lnQ for the test hypothesis, in which pseudoexperiments are drawn from a model which assumes Standard Model backgrounds plus Standard Model single-top production, and for the null hypothesis, in which pseudoexperiments are drawn from a model which assumes single-top production is absent. The dashed line indicates median expected p-value of $2.58 * 10^5$ or 4.05 σ and solid line indicates the data, with a p-value of 0.009 or 2.36σ .

100

Chapter 7

Search for Anomalous Wtb Coupling

7.1 Anomalous Wtb Coupling

In order to test the hypothesis that a fraction of single top quarks may be right-handed, we constructed a single-top events with MADEVENT [29]. The LO and NLO of t-channel samples need to be matched as fully differential NLO calculation[31].

To test anomalous Wtb coupling, we changed the handedness of the Wtb coupling from the SM left-handed version (V-$\mathbf{A}$) to V+$\mathbf{A}$, for two of the four W boson vertices in each event. We chose to be the production W and not the decay W. This is consistent with the available measurements of the W boson helicity in top quark decays [30], and borrows the singly-produced top quarks right-handed polarized. We call this the RRLL model (Figure 7.1).

Figure 7.2 shows the distributions of the cosine of the angle between the lepton and the down-type quark in the top quark rest frame. This angle is expected to show a $1 + \cos\theta$ distribution for 100% polarized top quarks along this axis [11][12]. For s-channel production, the down-type quark is contained in one of the beams, while for t-channel production, 2/3 of the time the down-type quark gives rise to a high-η jet. Because we reconstruct the high-η jet, and because t-channel production amounts to a higher fraction of single top quark production, we choose to use the angle $\cos\theta_{\ell j}$ in the reconstructed top quark frame.

The distribution of $\cos\theta_{\ell j}$ after reconstruction is shown in Figure 7.2. The right-hand side is sculpted by the lepton isolation cut. If the lepton is close to a reconstructed jet, then it removed by the isolation requirement. For the RRLL sample, the leptons are more often found at large angels relative to the jets, and the isolation cut gives less effect. On the other hand, the RRLL samples have

101

(R: V+A, L: V−A)
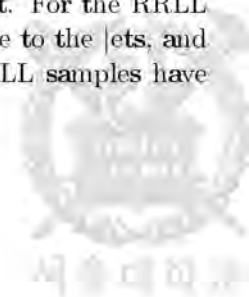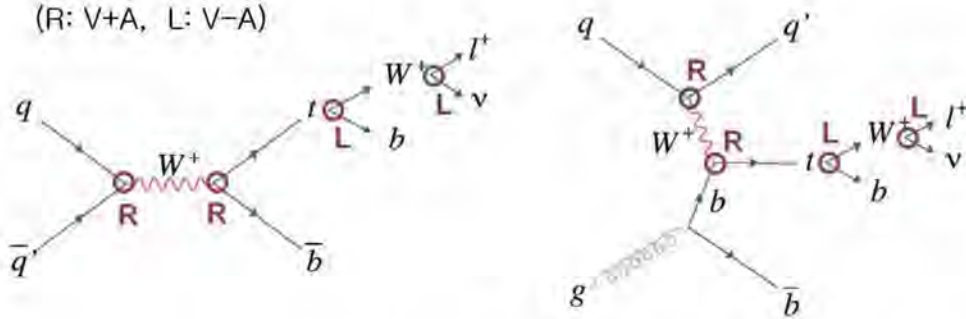
Figure 7.1. The RRLL sample's vertex coupling choices. "R" means $V+\mathbf{A}$ Wtb coupling, while "L" means V-$\mathbf{A}$ Wtb coupling.

leptons with a somewhat wider η distribution than the SM case, and hence the distribution of $\cos\theta_{\ell j}$ is sculpted on the other side as well.

To test Wtb coupling using top polarization, the variable of $\cos\theta_{\ell j}$ is used to fit LLLL and RRLL sample. After applying cut of likelihood function($L_t > 0.9$), signal events become larger compared to background. This histogram is LLLL case, and RRLL will show the mirror image.

In order to measure separately the RRLL and SM signals, we divide the sample into two subsets. One subset is that events are treated in the region of $\cos\theta_{\ell j} > 0$ and the others are $\cos\theta_{\ell j} < 0$. Also two discriminants are used to measure the two cross sections. The $\cos\theta_{\ell j} > 0$ sample is used to measure the SM (LLLL) cross section, and the $\cos\theta_{\ell j} < 0$ sample is used to train a discriminant to measure the RRLL cross section. The basic fitting method is same as the privious likelihood fit. To extract σ_{SM} and σ_{RRLL}, joint fit is carried out and the cross sections of each sample are measured. The correlation between the measured values of σ_{SM} and σ_{RRLL} are expected.

7.2   Search Result

A two-dimensional fit for the SM LLLL and exotic RRLL cross section is performed. The same technique is used as in the SM joint fits for the s- and t-channel production cross sections. The program xsfit2d.C is used, which calls the routine bh_2d_scan in mclimit_csm.C [28]. The same formalism is used as in the SM single top production cross section measurement. a Bayesian posterior is formed using a flat prior in the signal production cross section, and uncertain nuisance parameters are integrated over. In the two-dimensional case, a two-dimensional flat prior is chosen in the $(\sigma_{LLLL}; \sigma_{RRLL})$ plane.

102
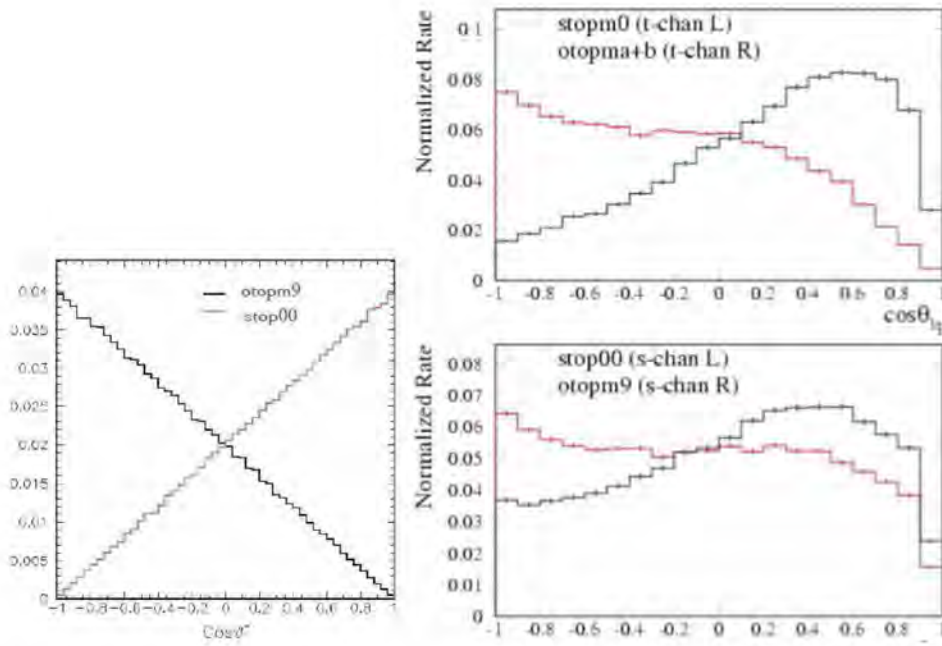
Figure 7.2. Left plot shows the distribution of $\cos\theta_{\ell q_{beam}}$ for the SM (stop00) and RRLL (otopm9) of s-channel. The $\cos\theta$ distributions of the SM and RRLL signal samples at the HEPG level has the opposite direction.

Right upper plot is the distributions of $\cos\theta_{\ell j}$ for t-channel signals of the SM (stopm0) and RRLL (otopma+b) after simulation, reconstruction, and event selection. The right bottom plot shows that the distribution of the s-channel at reconstruction level.

103
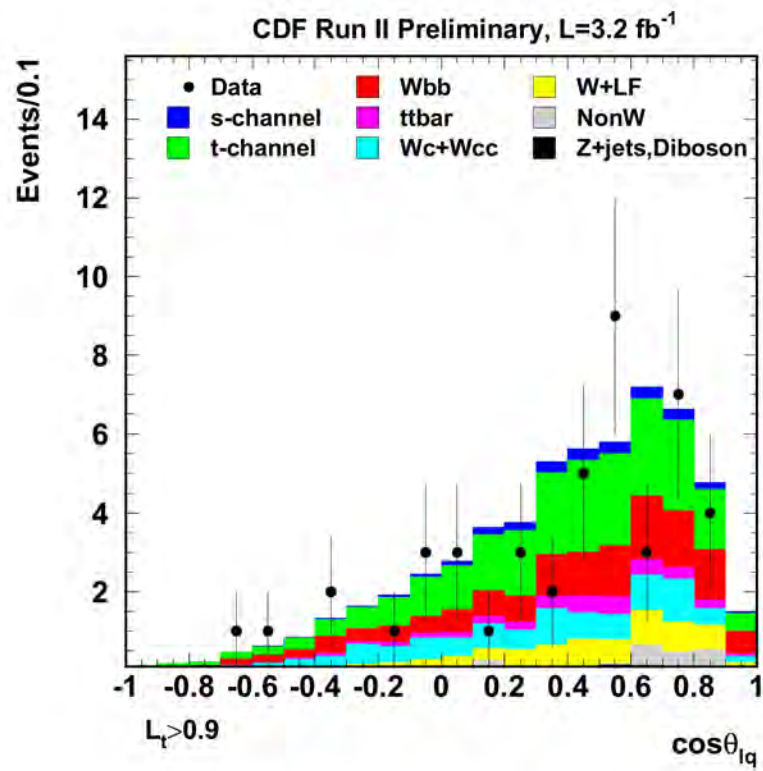
Figure 7.3. $cos\theta_{lq}$ with $L_t > 0.9$ (signal. SM)

104

In the general case, four production cross sections would have to be measured. The s-channel production may have a different polarization fraction from that in the t-channel production. We leave as a future exercise a more thorough exploration of the polarization-cross-section space. For now, we assume that the s- and t-channel production mechanisms have a total rate that is in the SM ratio. We do not constrain the total production rate to the SM rate, however.

We show the results of the 2D fit in Figure 7.4. β means ratio of the measured and expected cross section. The best-fit values are $\sigma_L / 1.43$ pb and $\sigma_R / 0.0$ pb. The green-shaded area indicates the region enclosing 68% of the integral of the posterior, and the yellow-shaded area indicates the region enclosing 95% of the integral of the posterior.

For the test of the anomalous Vtb coupling, the measured fraction of V+A coupling is

$$V + \mathbf{A} \quad . \quad 0 \pm 28 \quad (\%).$$
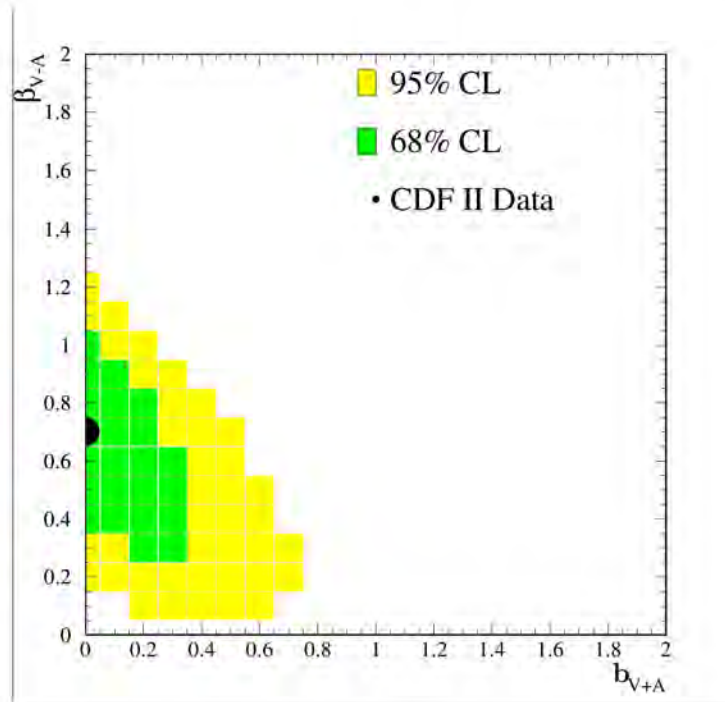
Figure 7.4. 2D Cross-section Fit

105

Chapter 8

Summary of Results and Discussion

The top quark pair is produced via strong interaction and was discoverd in 1995 at the Tevatron. The standard model of elementary particle physics also predicts electroweak single top-quark production; s-channel, t-channel, associated tW production. The s-channel and t-channel process are dominant at Tevatron, so these two channels are considerd in the analysis.

Measuring the cross section of single-top production provides a direct determination of CKM matrix of V_{tb}. It is difficult to measure the single-top cross section because small expected cross-section and dominant background. To distinguish signal from background, likelihood method is used by combining several input variables. The likelihood ouput distribution of expected background process and the simulated SM single top-quark signal is compared to the distribution of observed events using Bayesian maximum likelihood technique.

This thesis describes the result of a measurement of single-top cross-section and a test of anomalous W-t-b coupling using 4.8 f b^{-1} of data collected by the CDF II experiment at the Fermilab Tevatron.

The measured cross-section is

$$1.83 \ ^{+0.49(\text{stat})+0.49(\text{sys})}_{-0.43(\text{stat})-0.41(\text{sys})} \ (\text{pb})$$

we set the limit of

$$V_{\text{tb}} > 0.41 \ \text{at} \ 95\% \ \text{CL}.$$

For the test of the anomalous Vtb coupling, the measured fraction of $V+\text{A}$ coupling is

$$V + \text{A} \ : \ 0 \pm 28 \ (\%).$$

106

The future of precistion top-quark phycics will take place at LHC. Expected single-top cross-section is 6.6pb($\pm$10%) for s-channel, 156b($=$10%) for t-channel and 34pb($\pm$10%) for associated production at 14TeV.

107

Appendix A

Monitoring and Finding of Beam Position

A.1 Fitting Algorithm

Primary Vertex The primary vertex is reconstructed using tracks with the vxprim module [27] . One module produces a vertex collection from svx and the other module produces a vertex from cot. Figure[A.1],[A.2] show beam position and slope in xz-plane and yz-plane fitted by using primary vertexes.
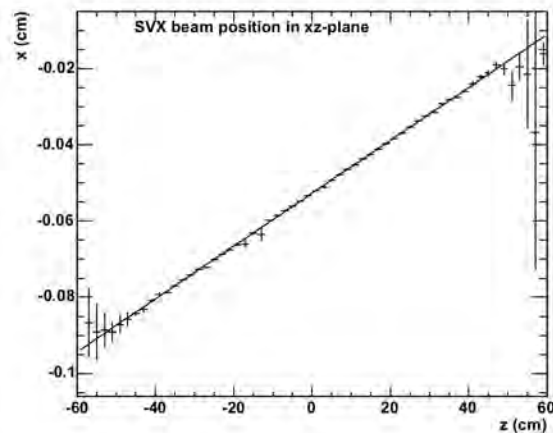
Figure A.1. Fitted SVX beam position in xz-plane using primary vertexes
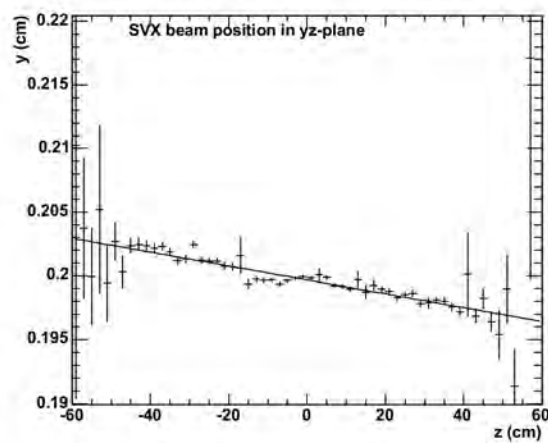
Figure A.2. Fitted SVX beam position in yz-plane using primary vertexes

D-ϕ Correlation The impact parameter D of a track from a primary vertex at $(x_V; y_V)$ can be parameterized.

$$D(x_v; y_v; \phi_0) / -x_v sin\phi_0 + -y_v cos_0$$
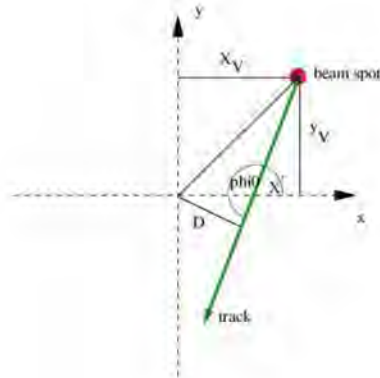
Using the z_0 parameter of the track and the beam line parameters $\vec{x}$ / $(x_0; y_0; x_{slope}; y_{slope})$ x_v and y_v can be written as.

$$x_v / x_0 + z_0 x_{slope} y_v / y_0 + z_0 y_{slope}$$

The impact parameter D can be expressed,

$$D(z_0; \phi_0) / \vec{x} \cdot \vec{g}$$

$\chi^2 / \sum_{i=1}^{n} (\frac{D_i - \vec{x} \cdot \vec{g}}{\sigma_i})$, with $\sigma_i^2 / \sigma_{D_i}^2 + 2\sigma_{Beam}^2$, with $\sigma_i^2 / \sigma_{D_i}^2 + 2\sigma_{Beam}^2$
Minimizing this χ^2, beam position can be obtained as follows.

$$\vec{x} / V \vec{b}$$

with

$$V^{-1} / \sum_{i=1}^{N} \frac{\vec{g_i} \vec{g_i}^T}{\sigma_i^2} \text{ and } \vec{b} / \sum_{i=1}^{N} \frac{D_i \vec{g_i}}{\sigma_i^2}$$

110

A.2 Plots of Beam Position

We studied beamlines for the silicon and cot about run range. Figure **A**.4 shows fit code for SVX and COT. Two constant values are stored; lower number means low statistical run. Figure **A**.5 and **A**.6 show the fitted value of beamline with x-axis and y-axis for SVX and COT. Figure **A**.7 is the value of difference of SVX and COT. We can check the tracking alignment from this plot. Annually, Silicon detector is sinking compared to COT little by little. Figure **A**.8 and **A**.9 are pull distributions of beam position of SVX-COT.

Run range is 222427~223642 (period. 9/1/2007~9/26/2007).
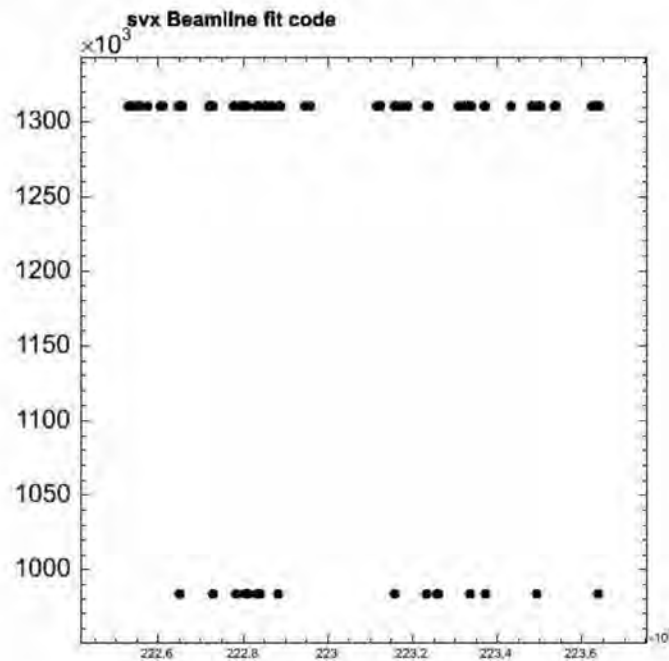
Figure **A**.3. Fit Codes for SVX with run 222427~223642. Two constant values are stored; lower number means low statistical run.
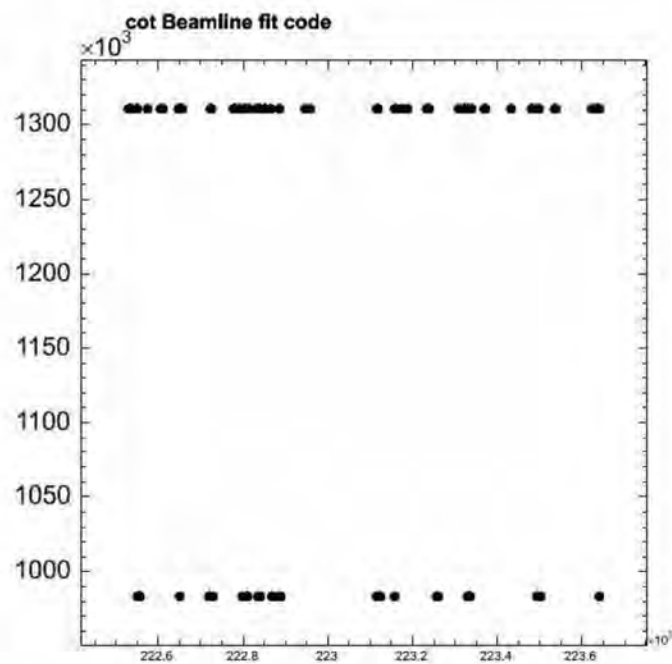
Figure A.4. Fit Codes for COT with run 222427~223642. Two constant values are stored; lower number means low statistical run.

112
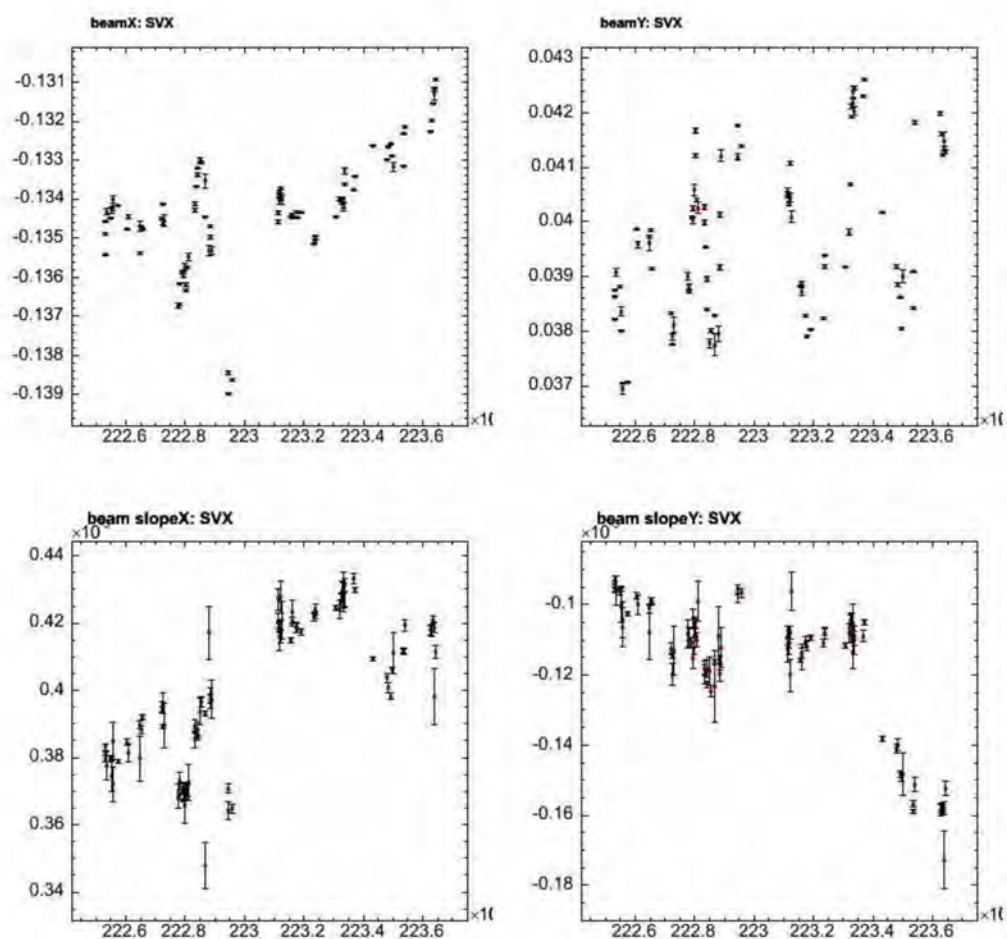
Figure A.5. BeamX Position of SVX with run 222427∼223642

113
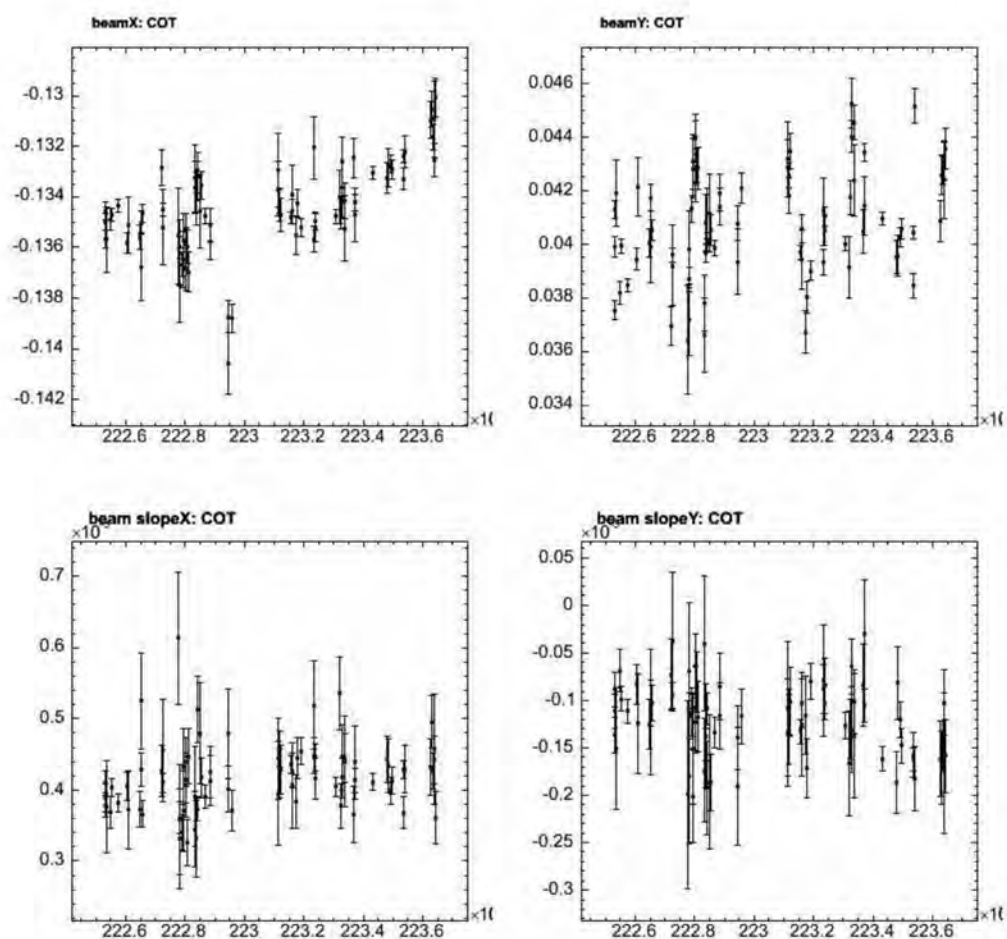
Figure A.6. BeamX Position of COT with run 222427∼223642

114
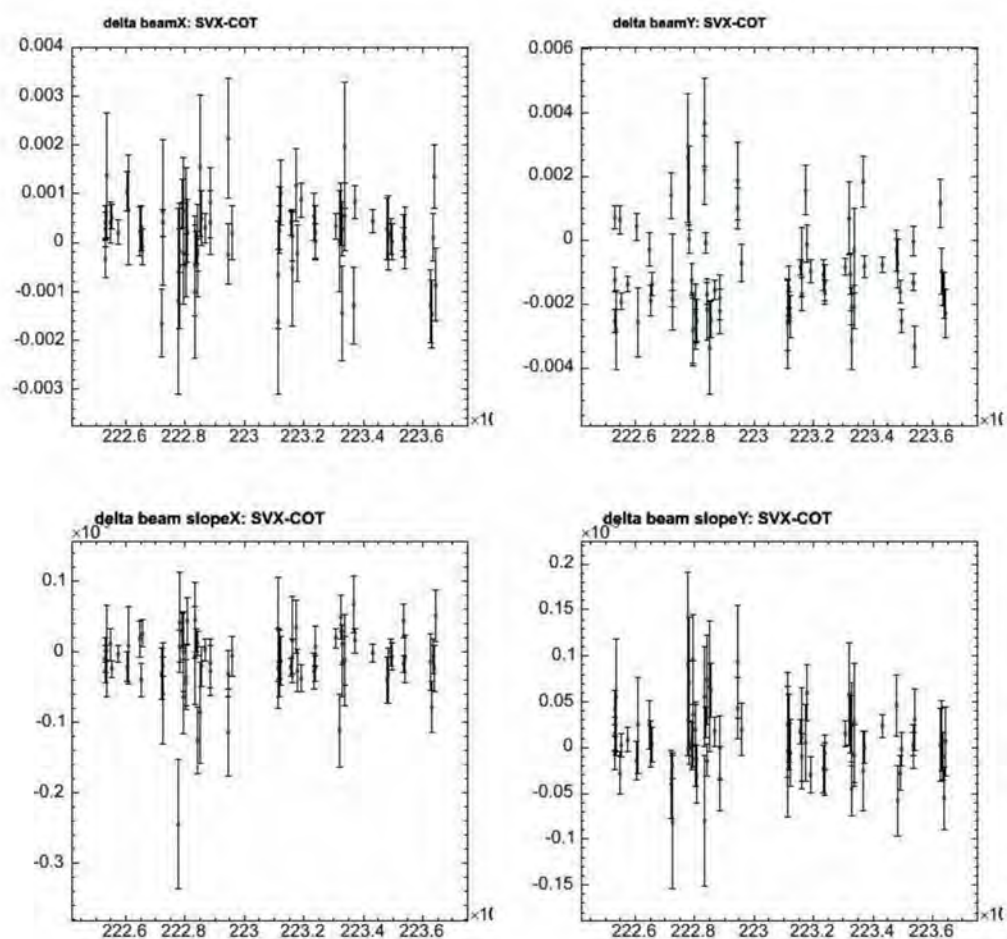
Figure **A**.7. Difference of SVX and COT beamline with run 222427~223642

115
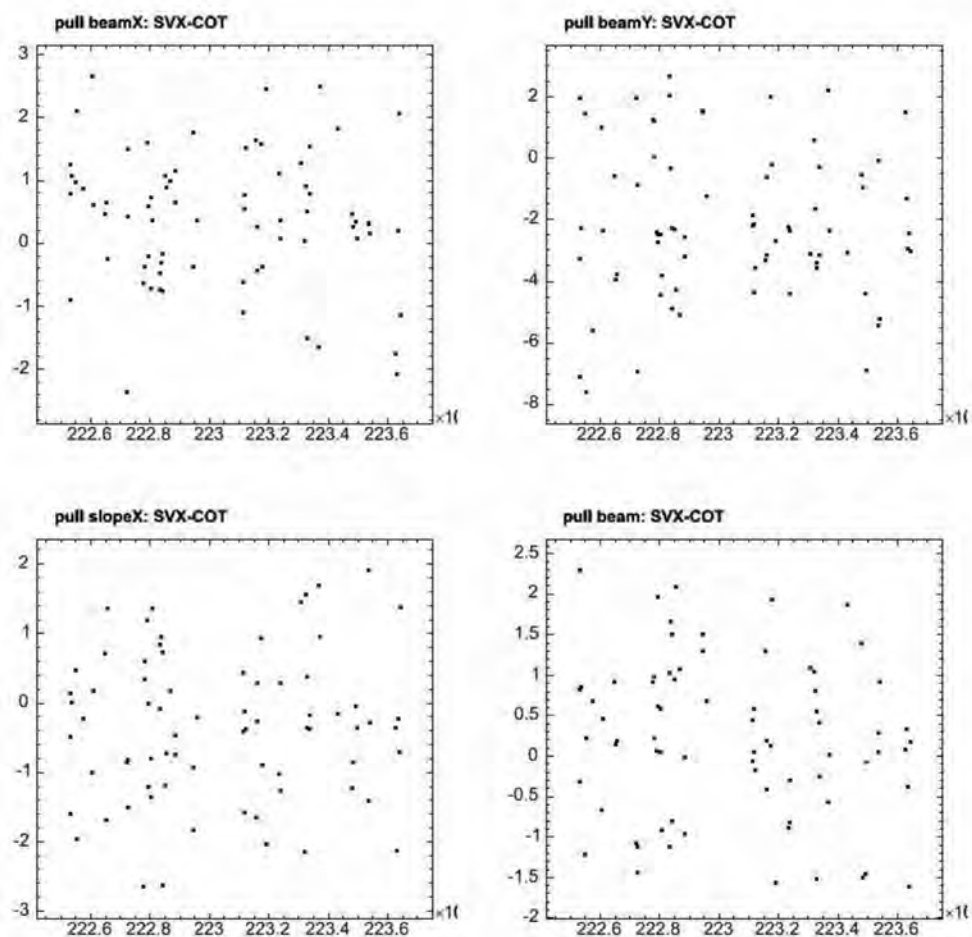
Figure A.8. Pulls of SVX-COT with run 222427∼223642

116
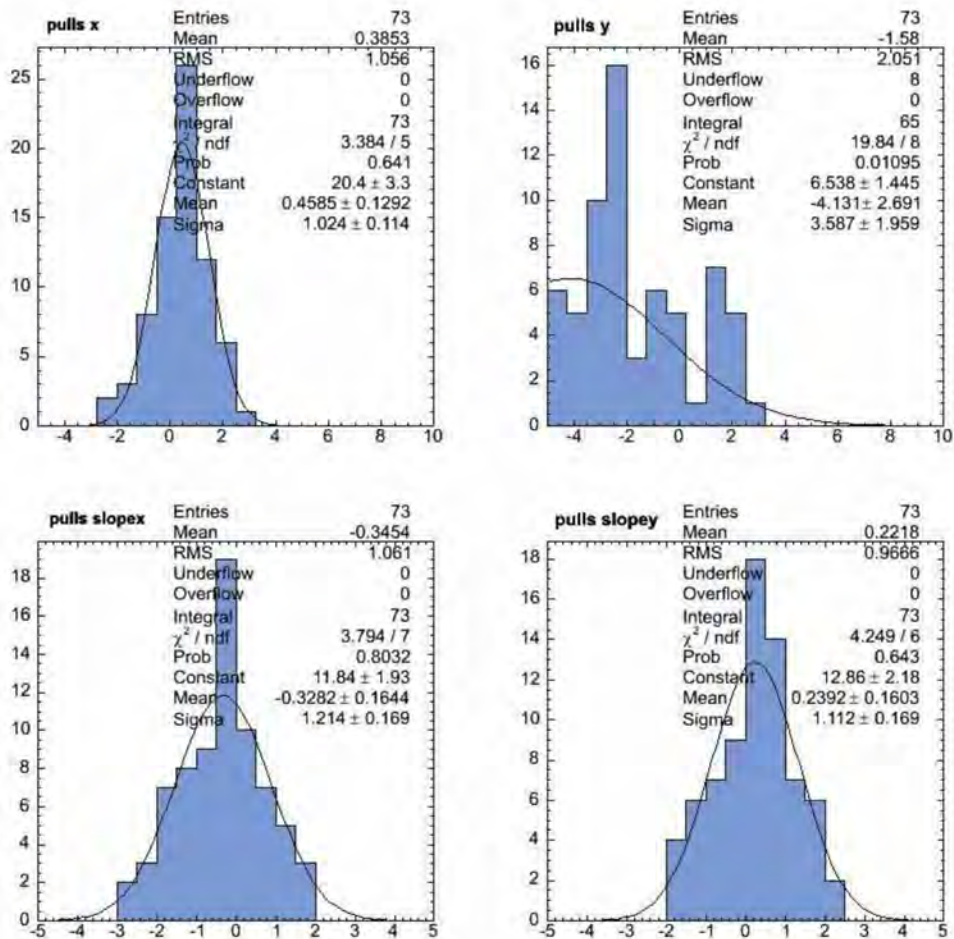
Figure **A**.9. Pull distribution of SVX-COT with run 222427~223642

117

Appendix B

MC Simulation of Single-top Production including NLO effect

We present a comparison between the MC@NLO samples and the official MadEvent samples currently used by the single-top group. In general we find good agreement between the two samples, but there are small number of differences.

The next-to-reading oder(NLO) QCD corrections enlarge the leading-order cross section by about 30% at Tevatron. For the analysis of single-top production, NLO results are important to have a reliable estimate of the number of events expected. The MC@NLO allows to match cross section computed at NLO in QCD with an event generator.

The t-channel LO and NLO process matching is done "by hand" in MadEvent. The two processes are generated separately, then the events from the two samples are combined using a technique of smoothing the P_T distribution of the second b |et. On the other hand, the MC@NLO program has the LO and NLO processes mixed internally to reproduce the theoretical NLO prediction for the single-top production.

In the case of standard MC, a hard kinematic configuration is generated on an event-by-event basis, and it is subsequently showered and hadronized. In the case of MC@NLO. all of the hard kinematic configuration (events)are generated in advance, and stored in a file and then each event is showered and hadronized by HERWIG. We generated event files using MC@NLO 3.3 package. We tell HERWIG that the events should be read from the event file using Les Houches interface by specifying a negative value of the process code IPROC. For the single-top production, IPROC is -2000-IC($H_1H_2 \rightarrow t/\bar{t}+X$), -2001-IC($H_1H_2 \rightarrow t+X$), or -2004-IC($H_1H_2 \rightarrow t+X$) by setting IC/ 10 and IC/ 20 for s- and t-channel pro-

duction. $H_{1,2}$ represents hadrons, p or $\bar{p}$.

We can set IL1CODE/ 1,2,3 for the lepton identification of W-decay. Spin correlation for the decay products are therefore taken into account.

B.1 Generator Level

The MadEvent samples and MC@NLO samples are compared at the hepg level. MadEvent single-top samples are LO s-channel, matched(LO+NLO) t-channel, and LO t-channel (for illustration purposes). The following pairs of samples are compared. (MadEvent LO s-channel, MC@NLO s-channel), (MadEvent LO t-channel, MC@NLO t-channel), and (MadEvent matched t-channel, MC@NLO t-channel). The compared plots of MadEvent and MC@NLO are shown in Figure B.1∼ B.9 ; the top mass and the eta, E, P_t, P_z of lepton, neutrino, b-quark from top, top quark.
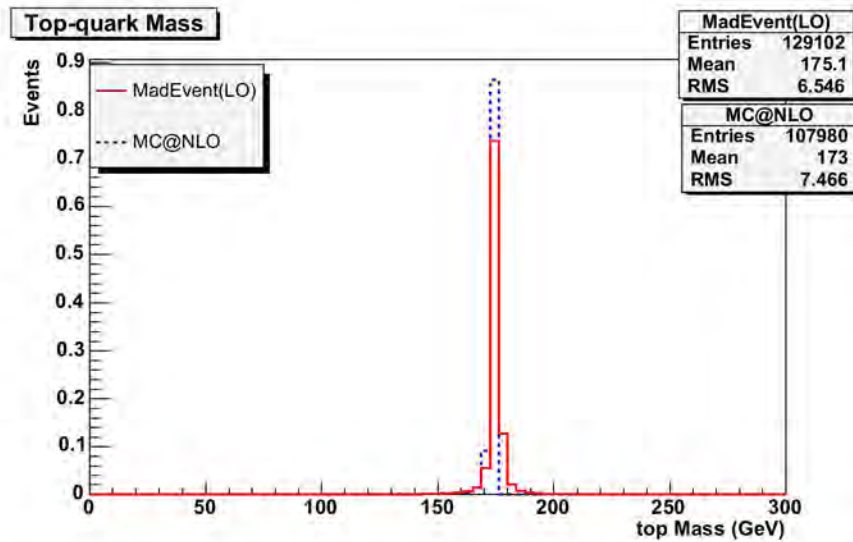
Figure B.1. s-channel sample. Top mass

119
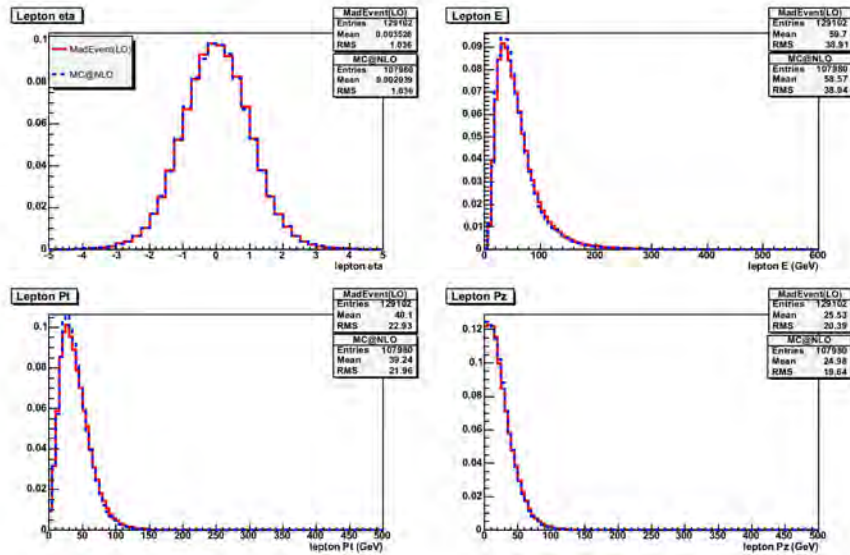
Figure B.2. s-channel sample. Lepton
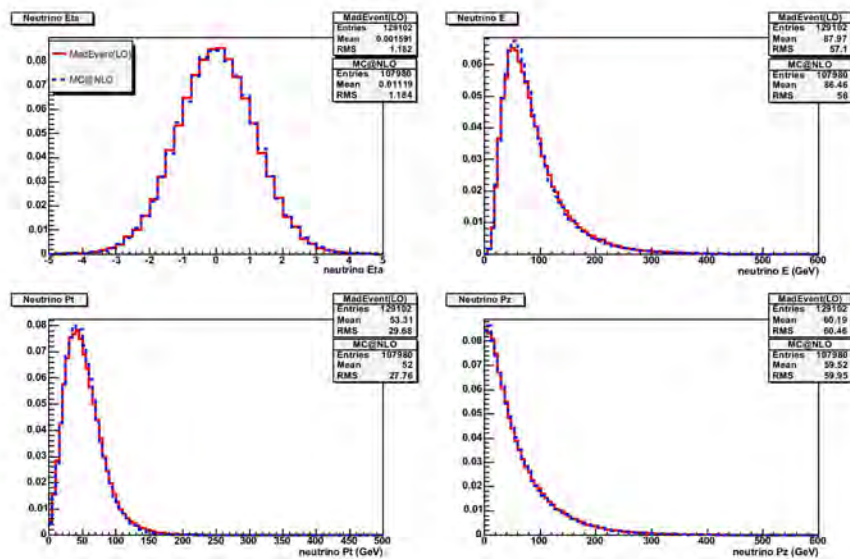
Figure B.3. s-channel sample. Neutrino

120
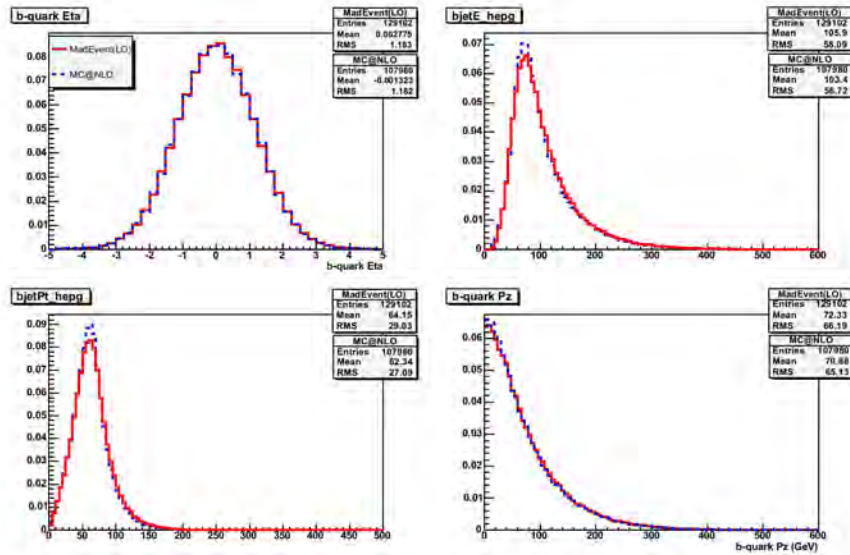
Figure B.4. s-channel sample. b-quark from top decay
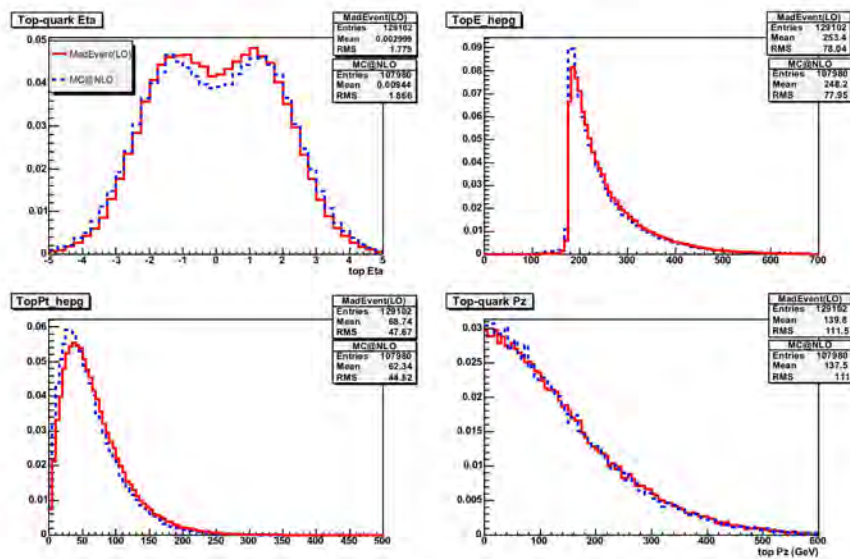
Figure B.5. s-channel sample. Top quark

121
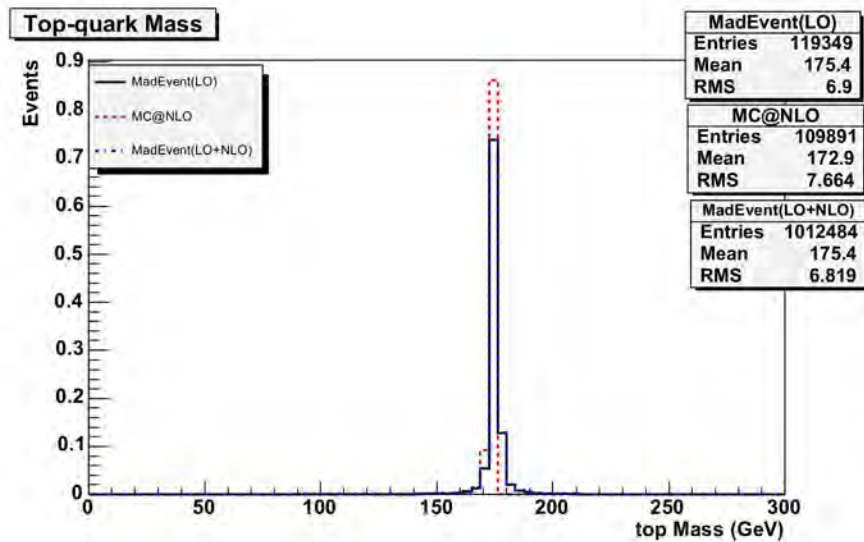
Figure B.6. t-channel sample. Top mass
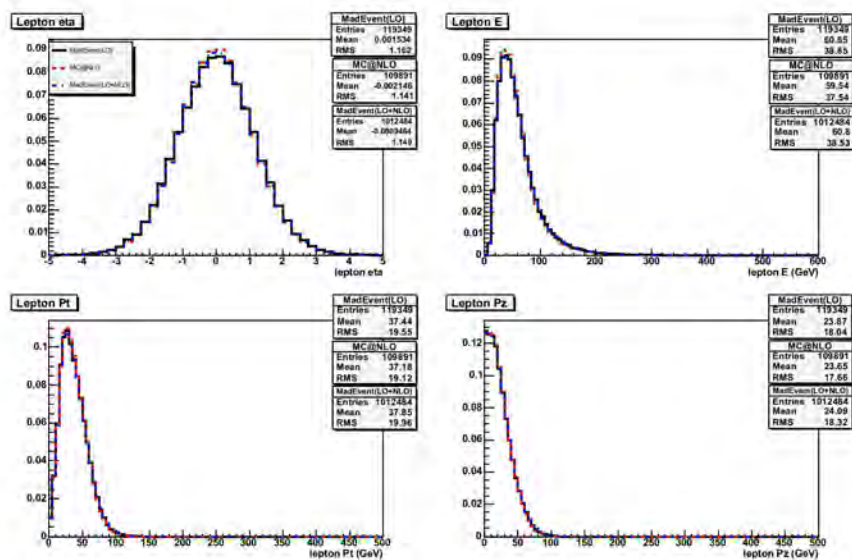
Figure B.7. t-channel sample. Lepton

122
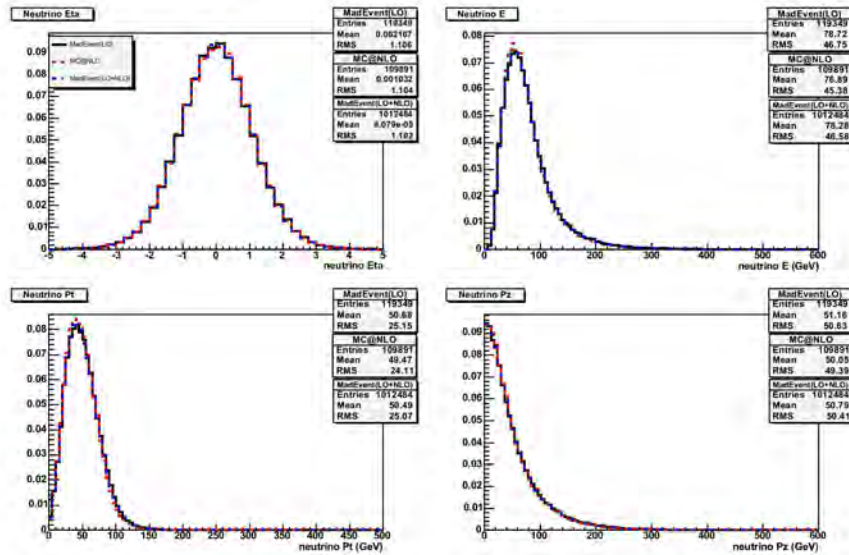
Figure B.8. t-channel sample. Neutrino
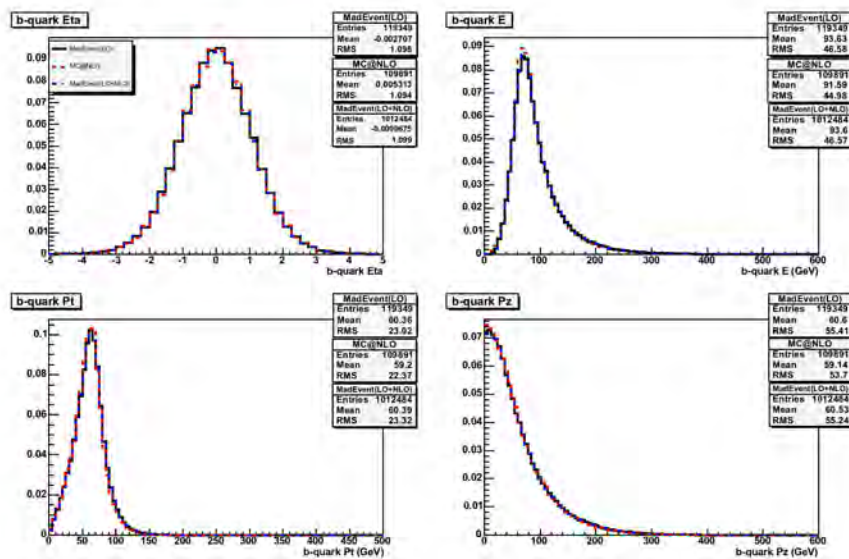
Figure B.9. t-channel sample. b-quark from top decay

123

B.2　Reconstruction level

The comparison of the acceptances for the two generator samples is shown in Table B.1 B.2 B.3 B.4. First two rows show the numbers of events while the following rows show the fraction of events out of the "Good run" total that pass the given sequence of cuts up to that point. For example, in Table 3, the number of 0Jet GoodRun has 4951 events and 0Jet Met has 405 events, which leads to the 8.18016 entry. If we look at the 2-|et channel, the official s-channel sample has a lower acceptance than MC@NLO (by 7%). The 3-|et bin however is more discrepant. For the t-channel samples, the 2-|et bin agreement is excellent, while the overall acceptances (all |et bins) are within 3-4%.

The compared plots of MadEvent and MC@NLO are shown in Figure B.10~ B.21 ; the top mass and the eta, E, P_t, P_z of lepton, neutrino, b-quark from top, top quark.

ALL	0Jets	1Jet	2Jets	3Jets	4+Jets	Total
Initial	5308	73540	235560	149876	52312	516596
GoodRun	4951	69092	220103	137426	47807	479379
Trigger	100	100	100	100	100	100
>/ 1TLep	9.73540	9.45406	8.38925	4.84697	4.24624	7.12797
Met	8.18016	7.84461	6.95356	4.05454	3.66055	5.93517
Iso	8.07917	7.55948	6.53421	3.41638	2.738092	5.42556
Dilep	7.95798	7.47119	6.48787	3.40110	2.72345	5.38446
Z	7.89739	7.42343	6.45652	3.37563	2.70462	5.35338
Cosmic/Chi2	7.89739	7.40461	6.42199	3.20827	2.51009	5.26743
!DiffZ	7.89739	7.40461	6.42153	3.20754	2.50590	5.26660
QCD	7.89739	7.10791	6.04716	2.99142	2.50590	4.98997
SiGoodRun	7.89739	7.10791	6.04716	2.99142	2.50590	4.98999
Taggable	0	5.29583	5.54331	2.83206	2.42014	4.36168
>/ 1+b-tag	0	2.59798	3.42657	1.76240	1.51860	2.60441

Table B.1. Acceptance table. s-channel MadEvent

124

ALL	0Jets	1Jet	2Jets	3Jets	4+Jets	Total
Initial	8152	107816	287748	189116	76172	669004
GoodRun	7751	102614	272697	176993	71001	631056
Trigger	100	100	100	100	100	100
>/ 1TLep	10.12772	9.78813	8.72286	5.76576	4.55204	7.61469
Met	8.51503	8.05055	7.25640	4.84764	3.91966	6.34999
Iso	8.38601	7.80010	6.79215	4.18773	3.02390	5.82119
Dilep	8.24409	7.74748	6.73824	4.15779	2.98869	5.77524
Z	8.19249	7.70070	6.70121	4.13406	2.96052	5.74117
Conv	8.19249	7.69193	6.65867	4.00411	2.78446	5.66510
!DiffZ	8.17958	7.69095	6.65793	4.00298	2.78446	5.66415
QCD	8.17958	7.45414	6.32130	3.77246	2.78446	5.41552
SiGoodRun	8.17958	7.45414	6.32130	3.77246	2.78446	5.41552
Taggable	0	5.63665	5.88932	3.61087	2.69432	4.77738
>/ 1+b-tag	0	2.63609	3.67294	2.24302	1.67462	2.83334

Table B.2. **Acceptance table.** s-channel MC@NLO

ALL	0Jets	1Jet	2Jets	3Jets	4+Jets	Total
Initial	55468	711584	1830872	999340	273284	3870548
GoodRun	52430	674338	1731507	931296	254225	3643796
Trigger	100	100	100	100	100	100
>/ 1TLep	9.24661	8.98970	8.01590	4.30453	3.81119	6.97190
Met	7.80278	7.41571	6.65044	3.61925	3.18497	5.79214
Iso	7.68453	7.21492	6.34274	3.08709	2.46002	5.42047
Dilep	7.57009	7.15650	6.31184	3.06862	2.44350	5.38745
Z	7.52431	7.10148	6.24548	3.03329	2.41360	5.33397
Cosmic/Chi2	7.52431	7.09065	6.20523	2.85140	2.20237	5.25161
!DiffZ	7.52431	7.08947	6.20459	2.85075	2.20119	5.25084
QCD	7.52431	6.86020	5.92085	2.70515	2.20119	5.03636
SiGoodRun	7.52431	6.86020	5.92085	2.70515	2.20119	5.03636
Taggable	0	4.88864	5.19558	2.53829	2.12842	4.17087
>/ 1+b-tag	0	2.13023	2.40518	1.32095	1.26856	1.96328

Table B.3. **Acceptance table.** t-channel MadEvent

125
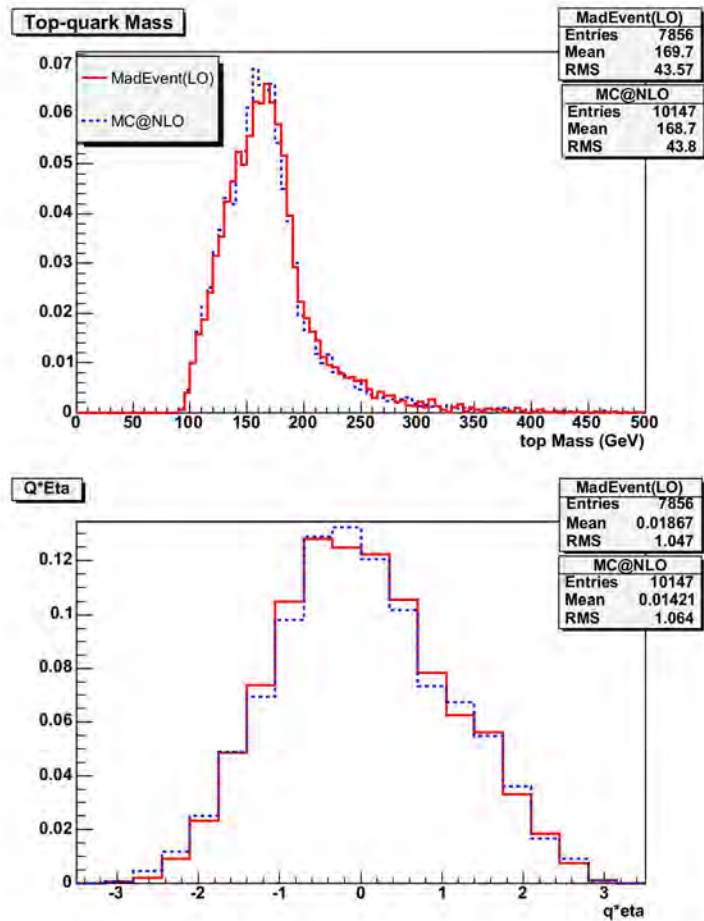
Figure B.10. s-channel sample. Top mass and $Q \times \eta$

126

ALL	0Jets	1Jet	2Jets	3Jets	4+Jets	Total
Initial	10504	130488	308572	173028	49708	672300
GoodRun	9930	123593	291755	161613	46204	633095
Trigger	100	100	100	100	100	100
>/ 1TLep	9.67774	9.31201	8.26960	4.86594	3.68582	7.29179
Met	8.39879	7.69218	6.88077	4.08073	3.17072	6.07744
Iso	8.33836	7.54168	6.60759	3.62408	2.53874	5.75853
Dilep	8.17724	7.46239	6.56304	3.60985	2.52142	5.71509
$\not{Z}$	8.11681	7.40090	6.46569	3.5516	2.47814	5.63928
Conv	8.11681	7.39362	6.42936	3.40628	2.31798	5.57230
!DiffZ	8.10674	7.39281	6.42833	3.40566	2.31798	5.57135
QCD	8.10674	7.16464	6.14385	3.23860	2.31798	5.35306
SiGoodRun	8.10674	7.16464	6.14385	3.23860	2.31798	5.35306
Taggable	0	5.09009	5.33941	3.03193	2.19677	4.38859
>/ 1+b-tag	0	2.20562	2.43491	1.52215	1.21850	2.03018

Table B.4. **Acceptance table**. t-channel MC@NLO
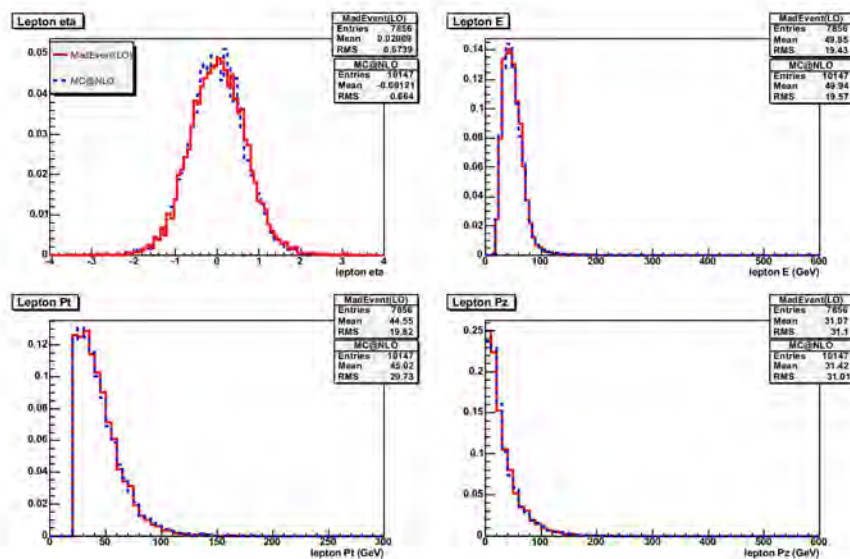
Figure B.11. s-channel sample. Lepton

127
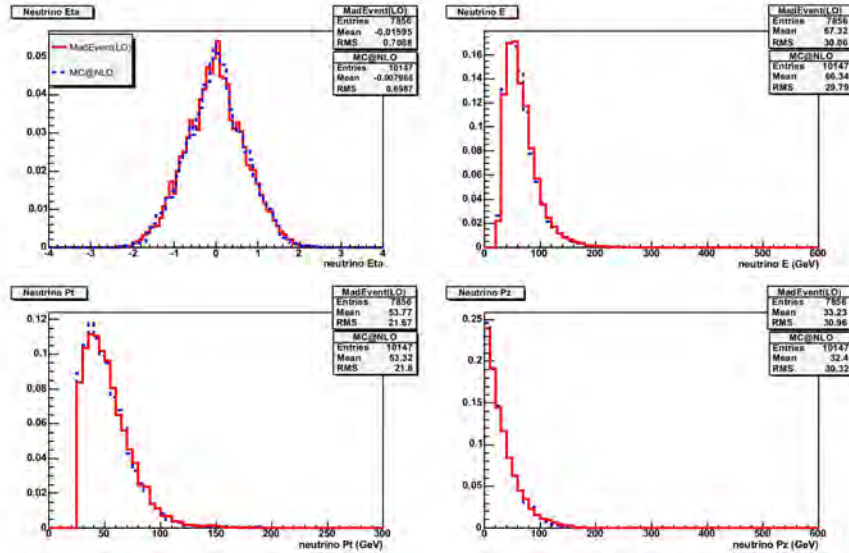
Figure B.12. s-channel sample. Neutrino
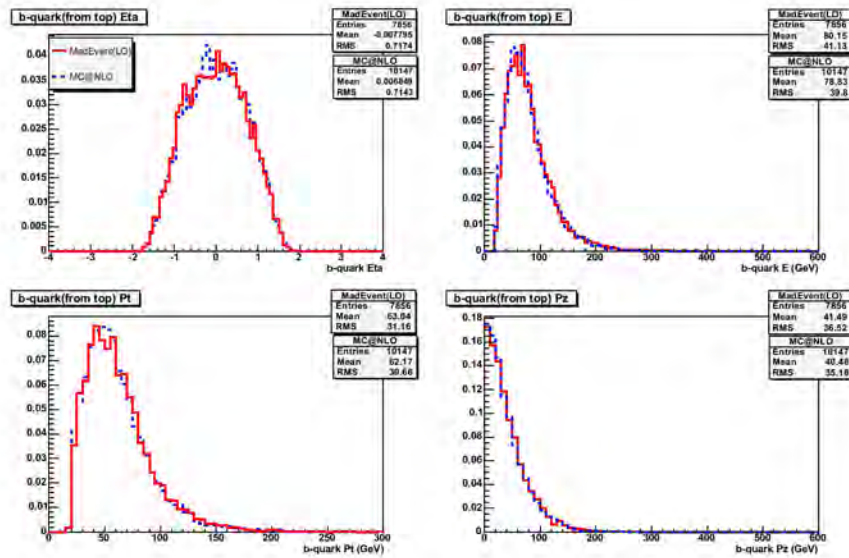
Figure B.13. s-channel sample. b-quark from top decay

128
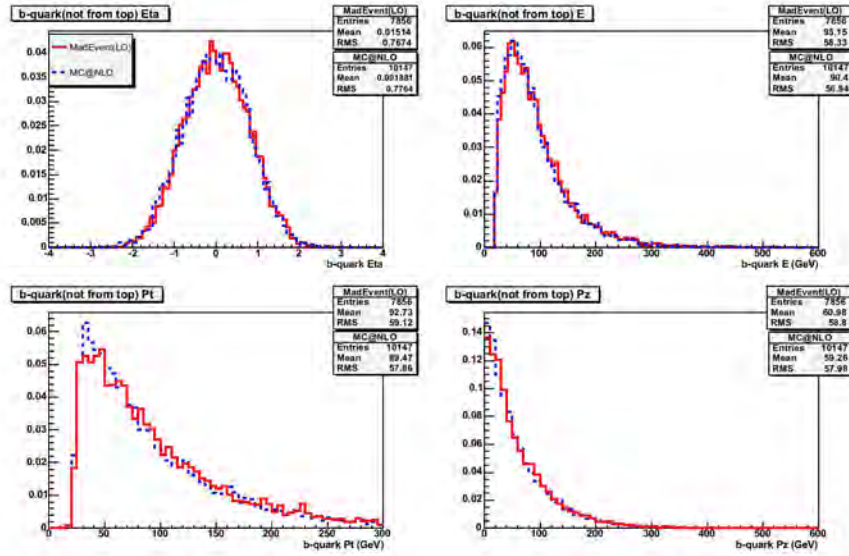
Figure B.14. s-channel sample. b-quark not from top decay
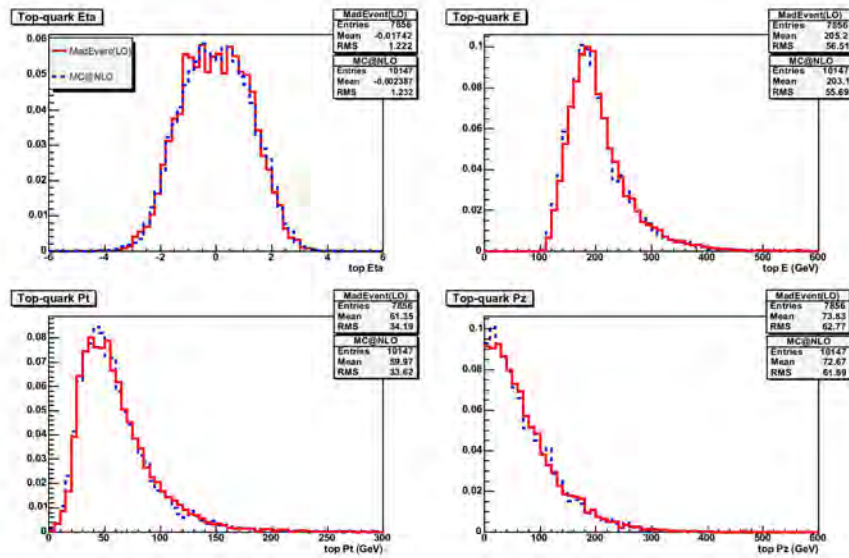
Figure B.15. s-channel sample. Top quark

129
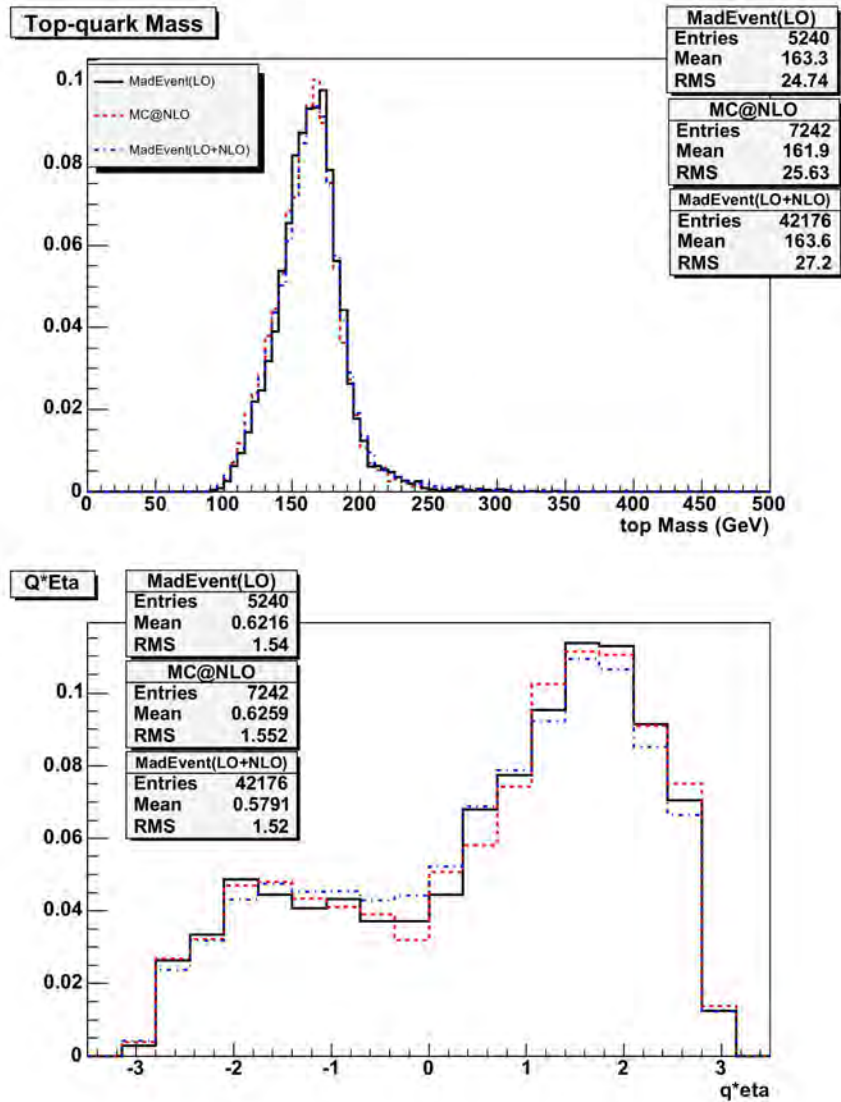
Figure B.16. t-channel sample. Top mass and $Q \times \eta$

130
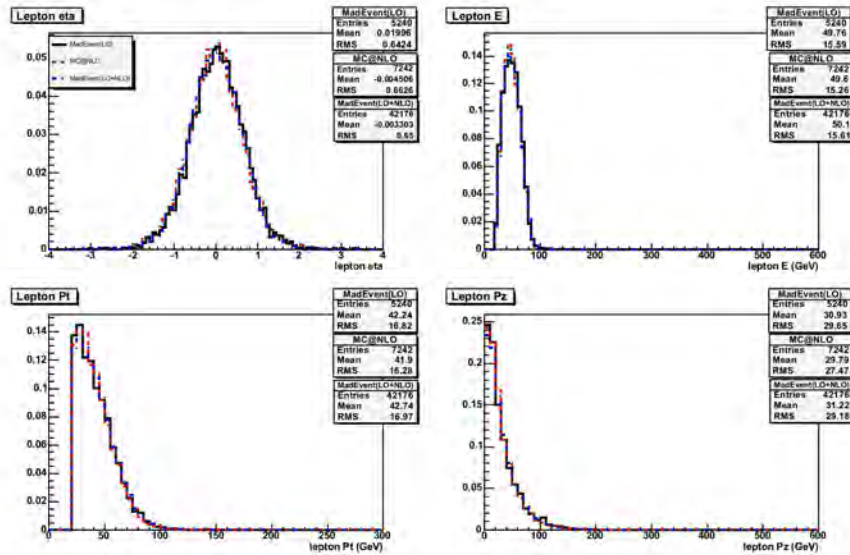
Figure B.17. t-channel sample. Lepton
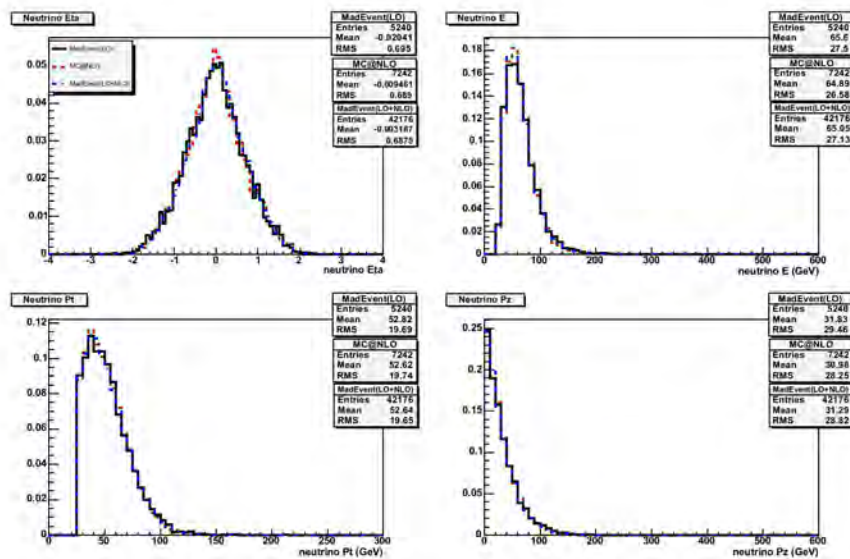
Figure B.18. t-channel sample. Neutrino

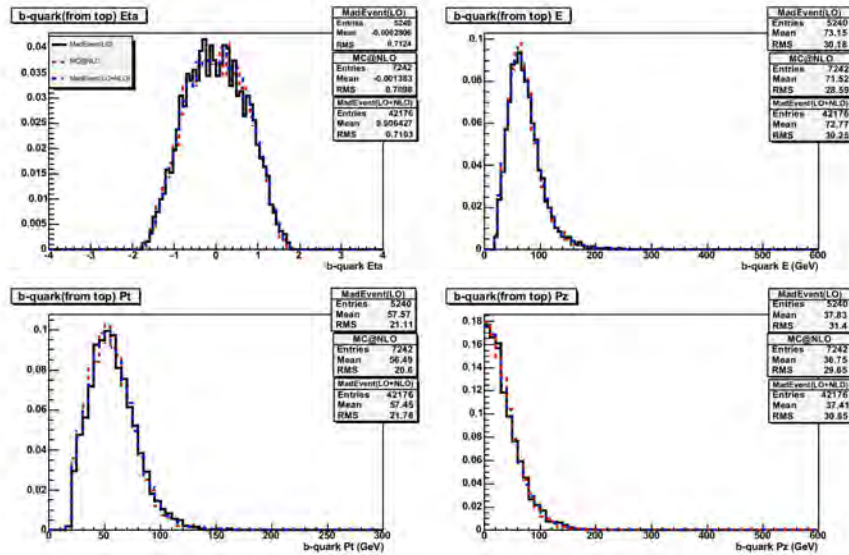131
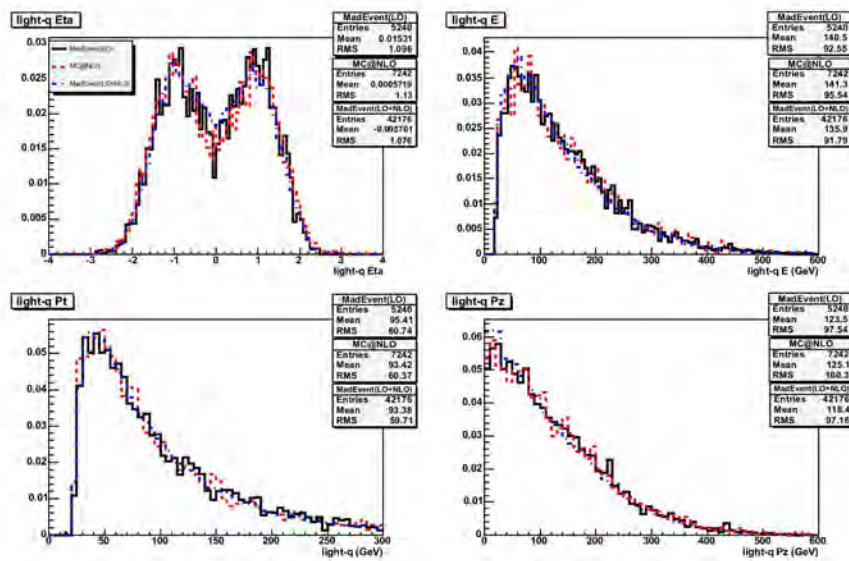
Figure B.19. t-channel sample. b-quark from top decay
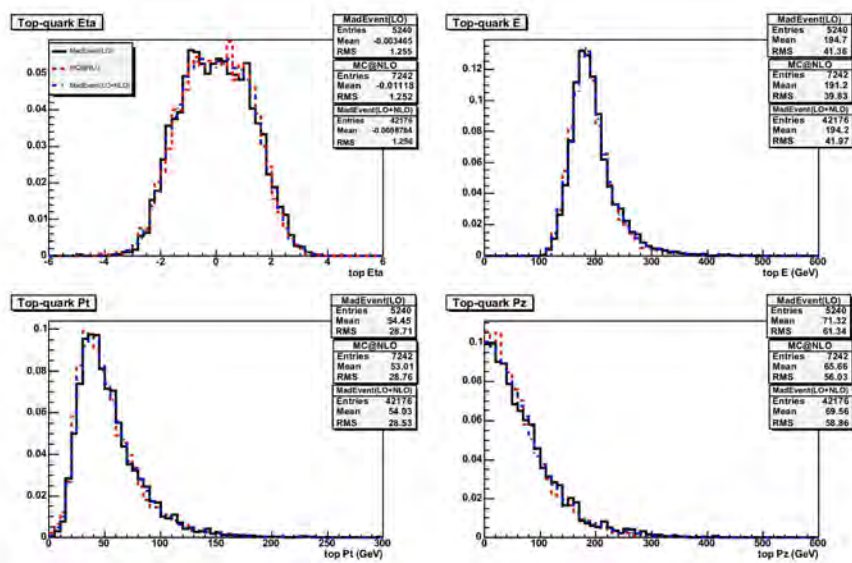

Figure B.20. t-channel sample. Light quark

132

Figure B.21. t-channel sample. Top quark

133

Appendix C

Shape Systematic Uncertainty

C.1 Plots

Compared with rate uncertainties, shape systematic uncertainties are considered as shape distortions of the templates for the signals and backgrounds. All shape uncertainties are median smoothed with five bins except the first and last two bins. The shape systematic sources are JES, PDF, ISR/FSR, Jet Flavor Separator Modeling, Mistag Model, Non-W Flavor Composition, Jet η Distribution, Jet 4 R_{jj} Distribution. Figure C.1~C.18 show compared plot(up) and ratio plot(down) between central and systematic sample.
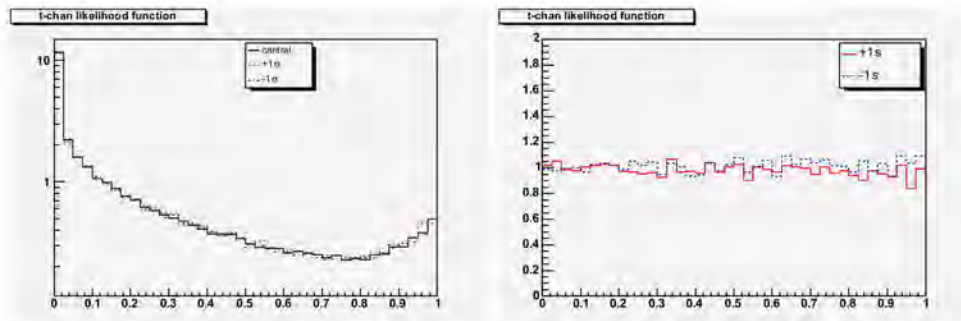
Figure C.1. JES Shape Systematic Uncertainty(s-channel); compared plot(up) and ratio plot(down) between central and systematic sample

134
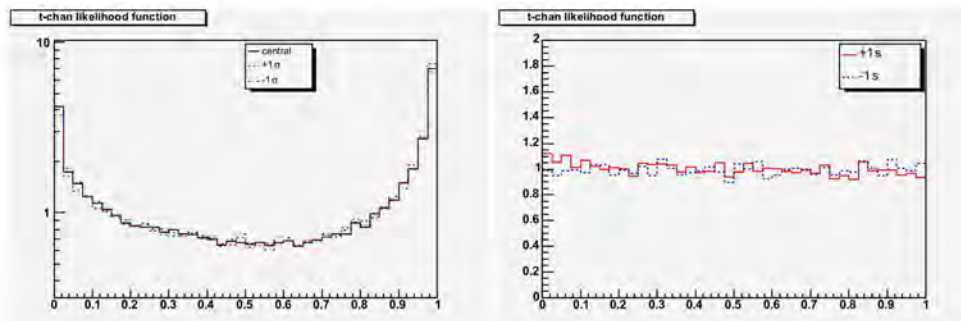
Figure C.2. JES Shape Systematic Uncertainty(t-channel); compared plot(up) and ratio plot(down) between central and systematic sample
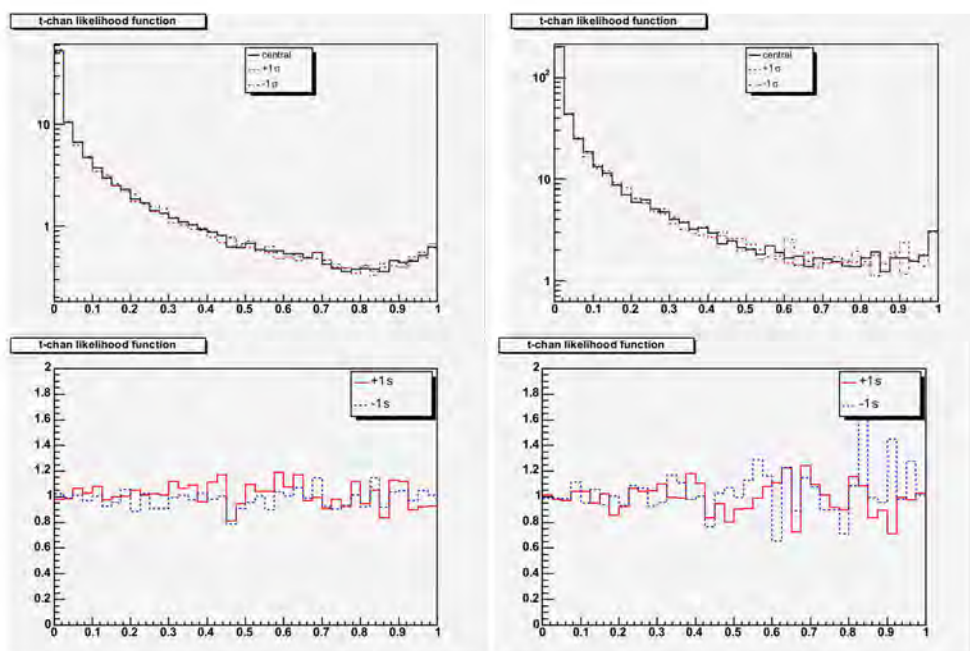
Figure C.3. JES Shape Systematic Uncertainty(ttbar/Wbb); compared plot(up) and ratio plot(down) between central and systematic sample
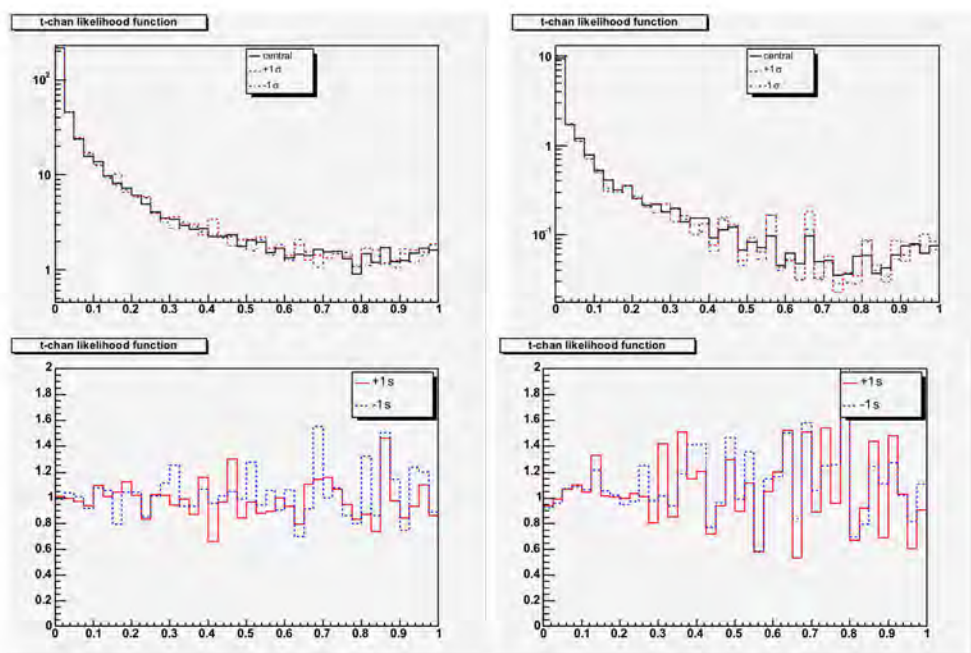
Figure C.4. JES Shape Systematic Uncertainty(WC/Z|ets); compared plot(up) and ratio plot(down) between central and systematic sample
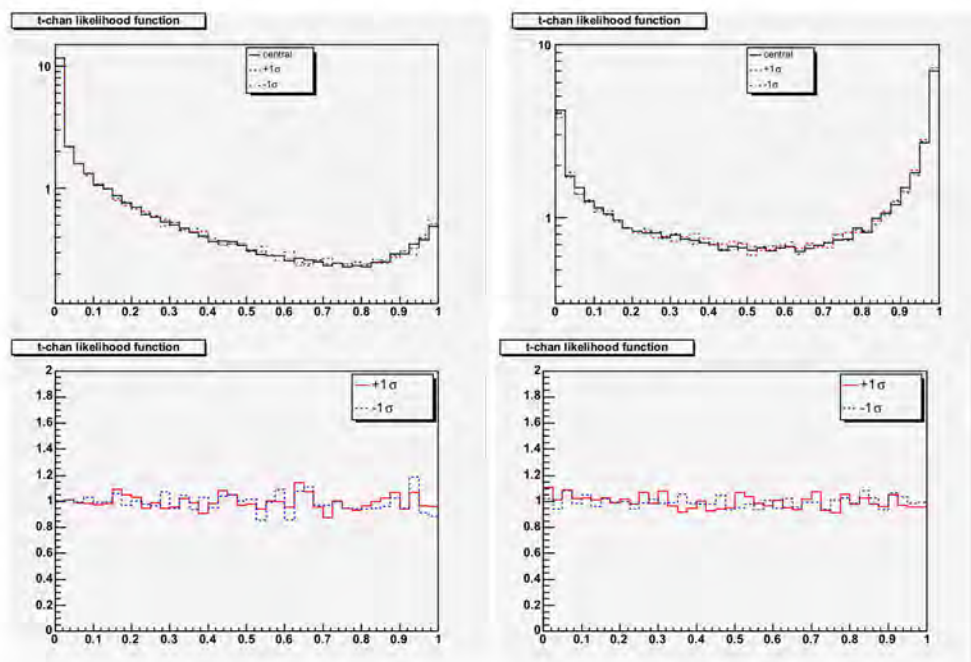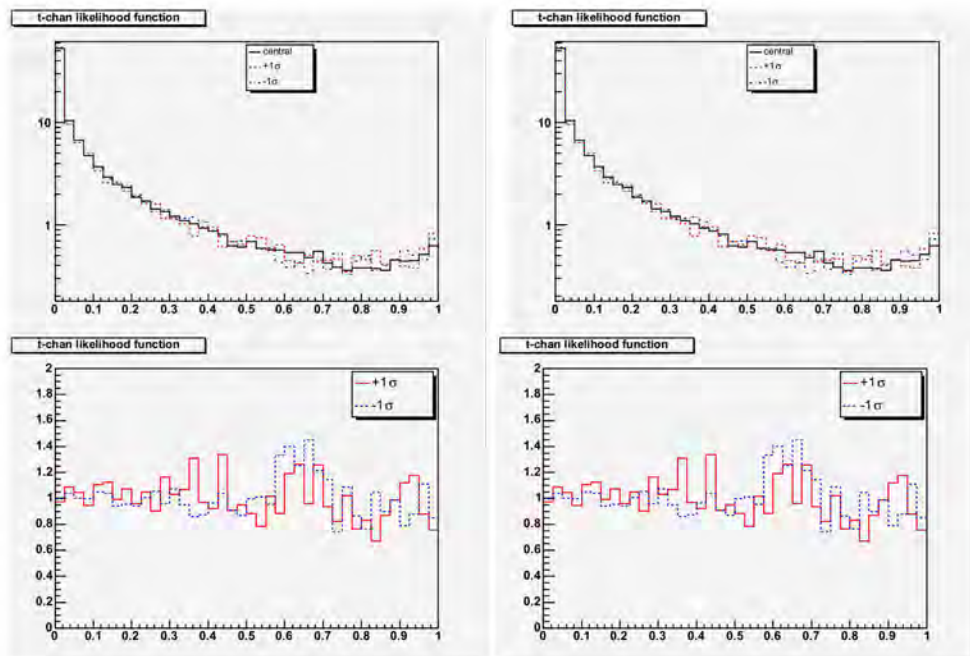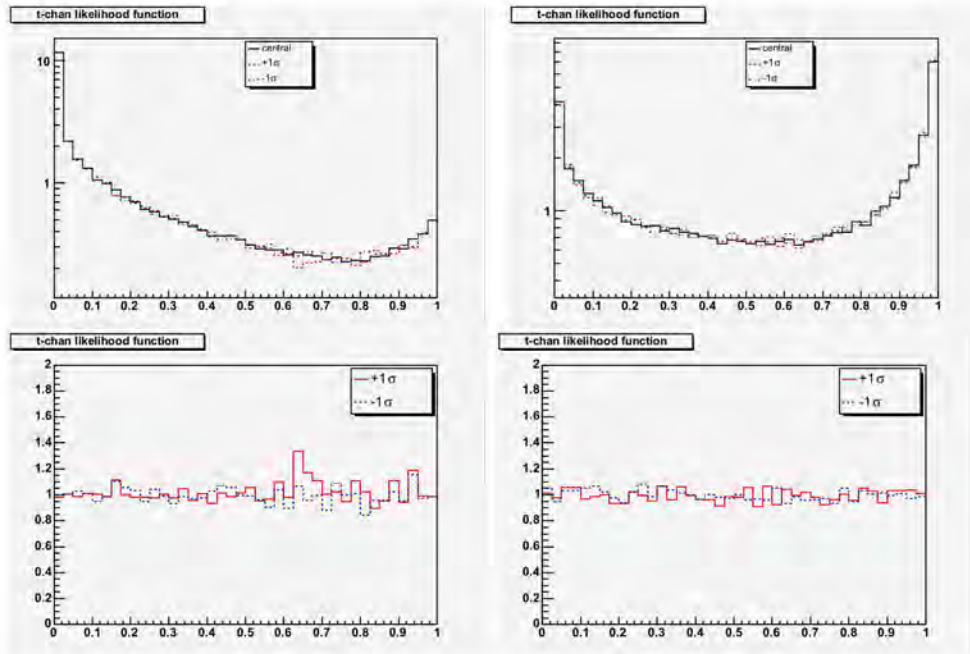
136

Figure C.5. ISR Shape Systematic Uncertainty(s-/t-channel); compared plot(up) and ratio plot(down) between central and systematic sample

137

Figure C.6. ISR Shape Systematic Uncertainty(**ttbar**); compared plot(up) and ratio plot(down) between central and systematic sample

138

Figure C.7. FSR Shape Systematic Uncertainty(s-/t-channel); compared plot(up) and ratio plot(down) between central and systematic sample
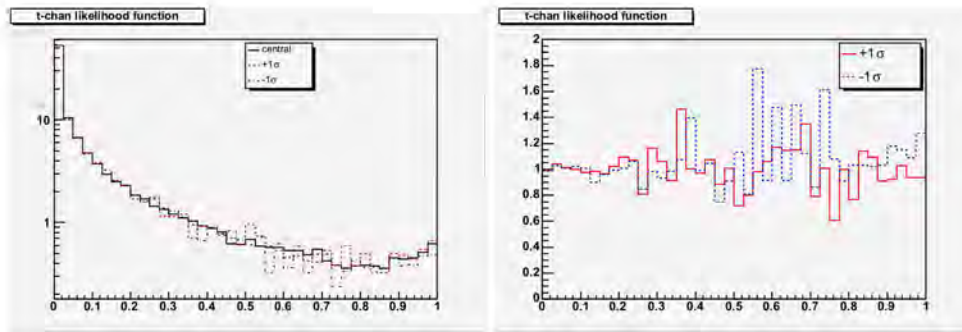

Figure C.8. FSR Shape Systematic Uncertainty(ttbar); compared plot(up) and ratio plot(down) between central and systematic sample
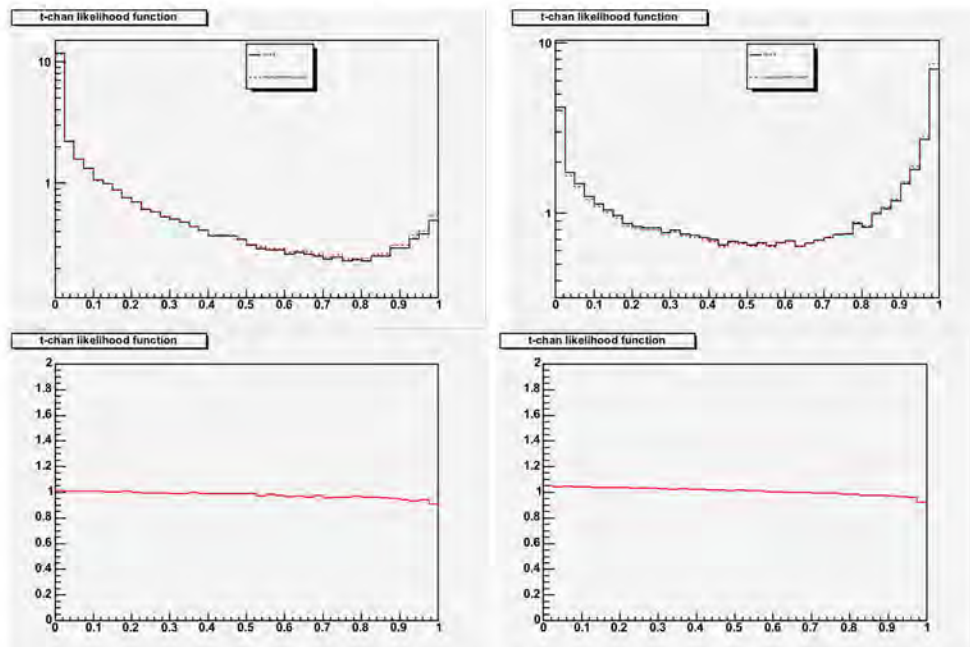
Figure C.9. Eta|2 Shape Systematic Uncertainty(s-/t-channel); compared plot(up) and ratio plot(down) between central and systematic sample
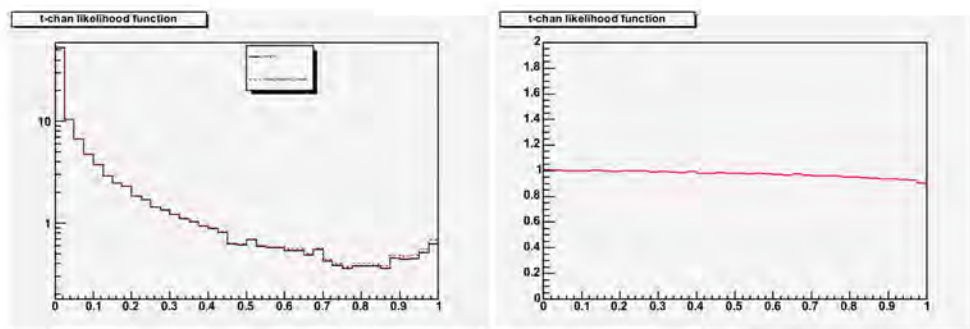

Figure C.10. Eta|2 Shape Systematic Uncertainty(ttbar); compared plot(up) and ratio plot(down) between central and systematic sample
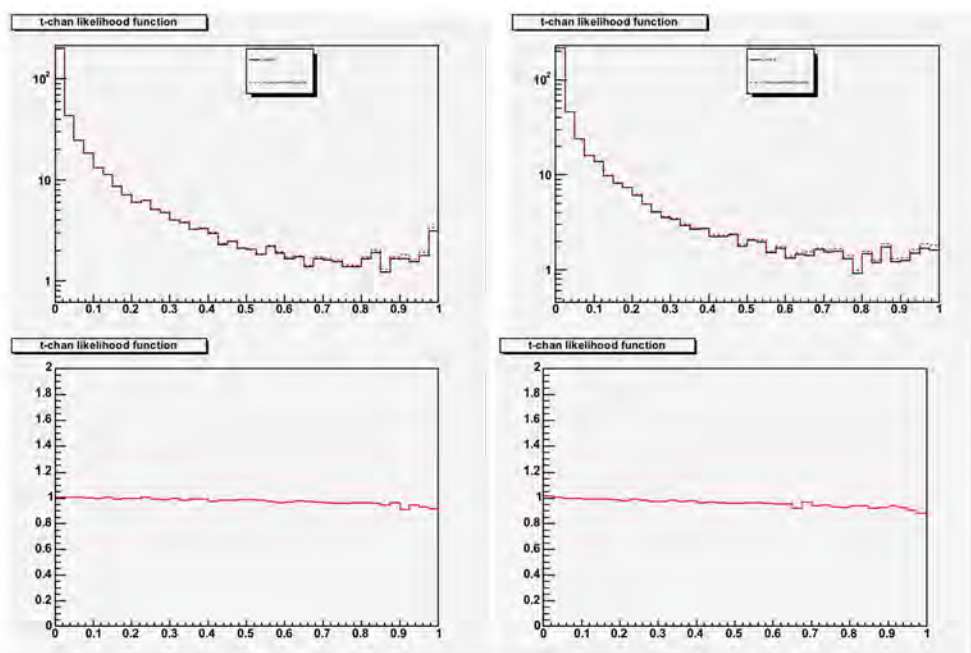
140

Figure C.11. Eta|2 Shape Systematic Uncertainty(Wbb/WC); compared plot(up) and ratio plot(down) between central and systematic sample

141

Figure C.12. Eta|2 Shape Systematic Uncertainty(mistag/Z|ets); compared plot(up) and ratio plot(down) between central and systematic sample

142

Figure C.13. DeltaR|2 Shape Systematic Uncertainty(s-/t-channel); compared plot(up) and ratio plot(down) between central and systematic sample

Figure C.14. DeltaR|2 Shape Systematic Uncertainty(ttbar); compared plot(up) and ratio plot(down) between central and systematic sample

143

Figure C.15. DeltaR|2 Shape Systematic Uncertainty(Wbb/WC); compared plot(up) and ratio plot(down) between central and systematic sample

144

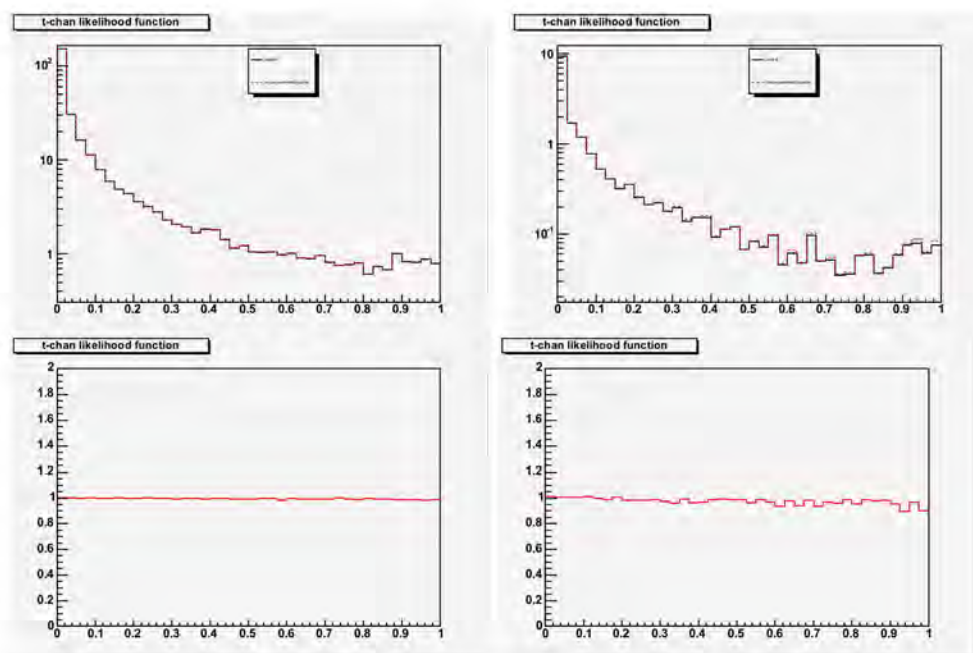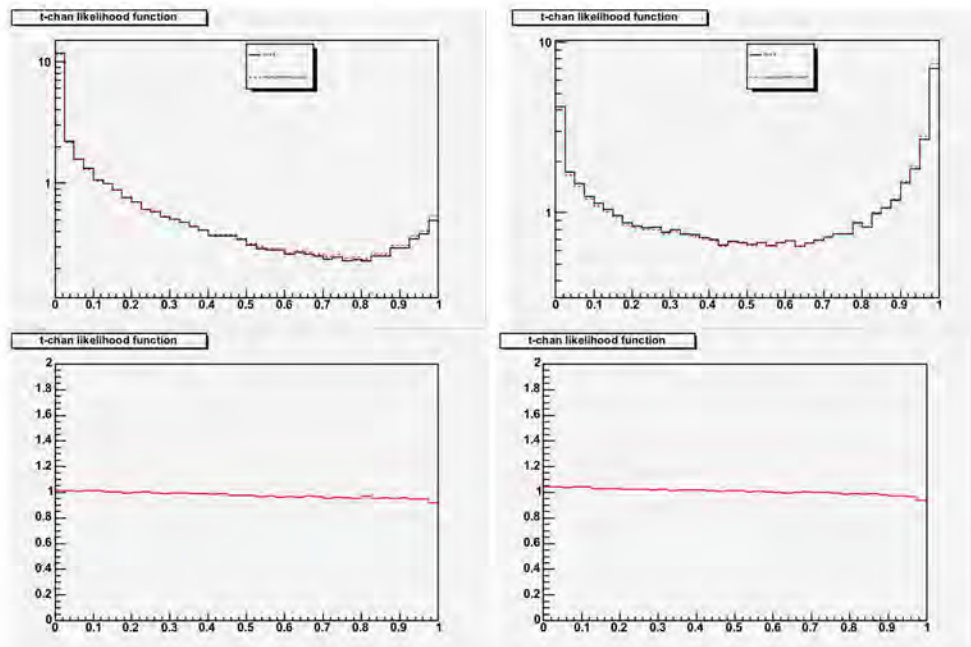Figure C.16. DeltaR|2 Shape Systematic Uncertainty(mistag/Z|ets); compared plot(up) and ratio plot(down) between central and systematic sample

145

Figure C.17. NNbtag Shape Systematic Uncertainty(Diboson/WC); compared plot(up) and ratio plot(down) between central and systematic sample
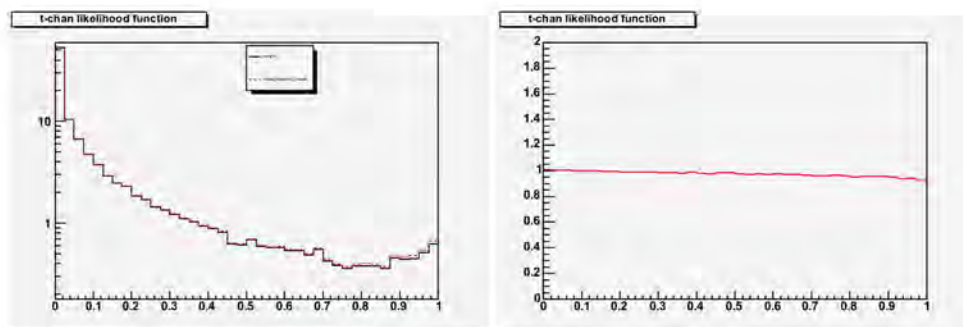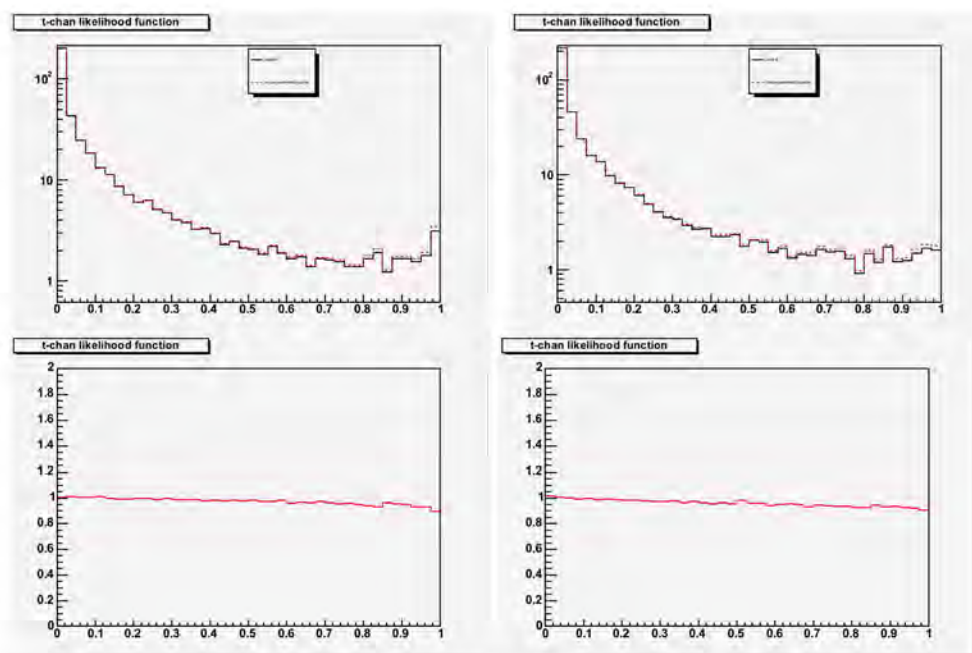

Figure C.18. Nonwflav Shape Systematic Uncertainty(nonw); compared plot(up) and ratio plot(down) between central and systematic sample
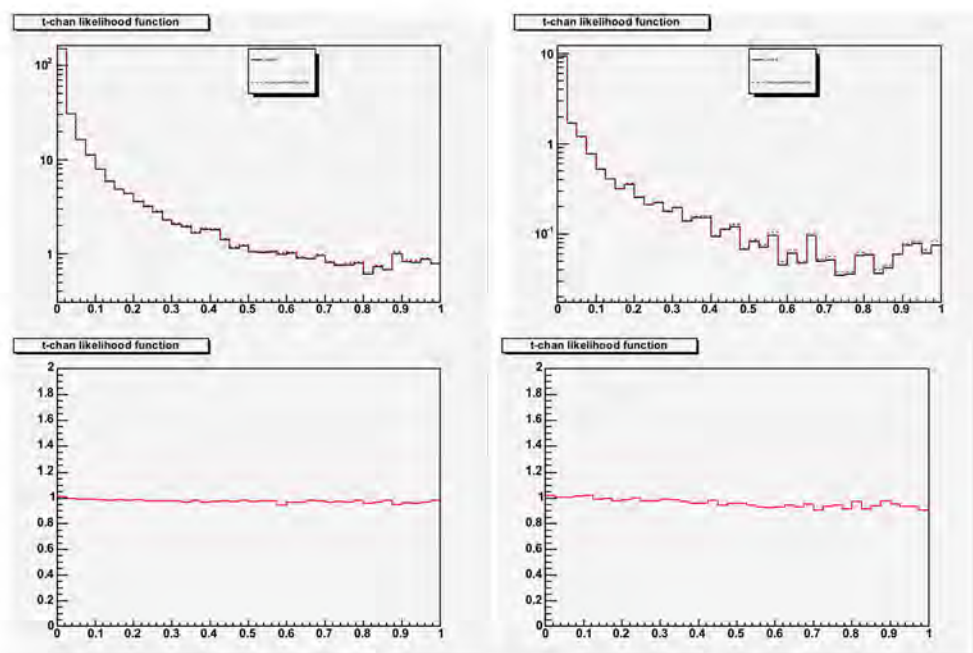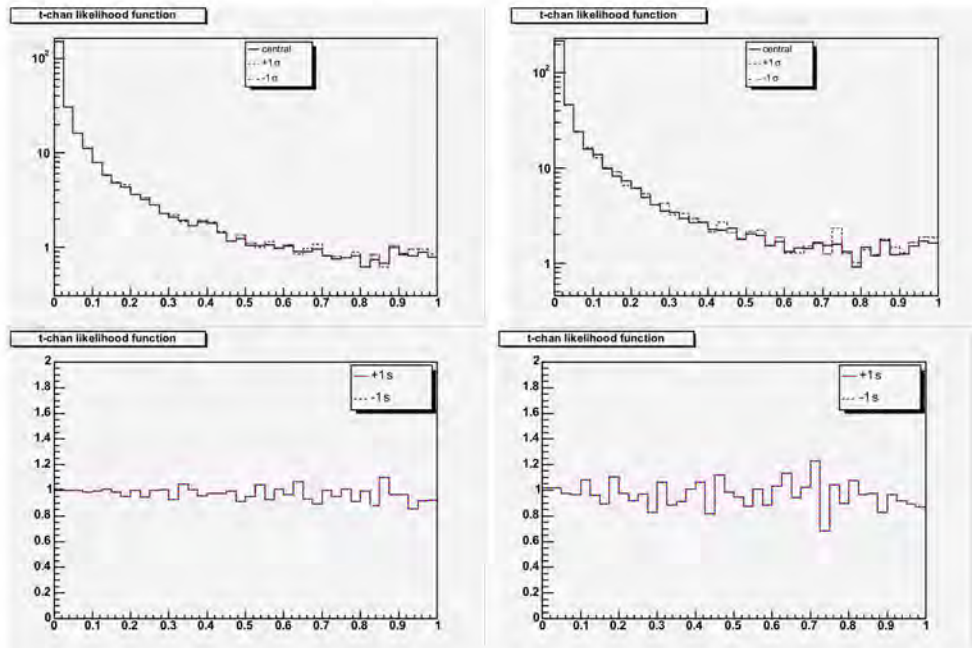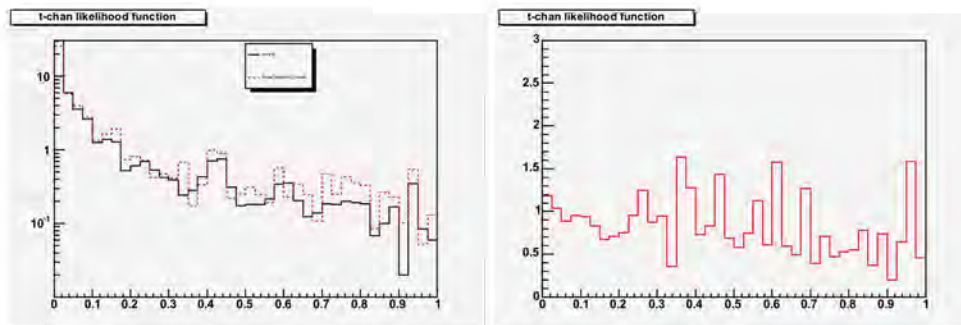
146

Bibliography

[1] D. Acosta et al. [CDF Collaboration], Phys. Rev. Lett. 95, 102002 (2005) [hep-ph/0505091]

[2] V. M. Abazov et al. [D0 Collaboration], arXiv.0801.1326

[3] J. Swain and L. Taylor, Phys. Rev. D58, 093006 (1998) [hep-ph/9712420]

[4] N. Kidonakis "Single top quark production at the Fermilab Tevatron.Threshold resummation and finite-order soft gluon corrections" Phys. Rev. D 74, 114012(2006)

[5] K. Goulianos Diffractive and Total Cross Section at Tevatron and LHC

[6] T. Aaltonen et al.[The CDF collaboration], "First Observation of Electroweak Single Top quark Production" arXiv.0903.0885[hep-ex].

[7] V. M. Abazov et al.[The D0 Collaboration], "Observation of Single Top Quark Production" arXiv.0903.0850[hep-ex].

[8] T. Aaltonen et al.[CDF Collaboration], "Measurement of the Single Top Quark Production Cross Section at CDF" Phys. Rev. Lett 101, 252001 (2008) arXiv.0809.2581[hep-ex]

[9] V. M. Abazov et al.[The D0 Collaboration], "Evidence for production of single top quarks and first direct measurement of $|V(tb)|$" Phys. Rev. Lett 98, 181802 (2007)

[10] V. M. Abazov et al.[The D0 Collaboration], "Evidence for production of single top quarks" Phys. Rev. D 78, 012005 (2008)

[11] G. Mahlon, S. Parke "Improved Spin Basis for Angular Correlation Studies in Single Top Quark Production at the Tevatron" arXiv.9611367[hep-ex]

[12] G. Mahlon "Spin Polarization in Single Top Events" arXiv.9811219[hep-ex]

147

[13] *V. M.* **Abazov** et al.[The D0 Collaboration] "Search for Anomalous Wtb Coupling in Single Top Quark Production" Phys. Rev. Lett 101, 221801 (2008)

[14] T. Stelzer, *Z.* Sullivan and S. Willenbrock, Phys. Rev. D 58, 094021 (1998) [arXiv.hep-ph/9807340].

[15] G. Abbiendi et al. [OPAL Collaboration], Phys. Lett. B 444, 539 (1998) [arXiv.hep-ex/9808006].

[16] T. **Aaltonen** et al. [CDF Collaboration], arXiv.0812.3400 [hep-ex].

[17] T. M. P. **Tait** and C. P. P. Yuan, Phys. Rev. D 63, 014018 (2001) [arXiv.hep-ph/0007298].

[18] S.R. Budd, C.I. Ciobanu, J-E. Jung, T.R. Junk, S-B. Kim, "Measurement of Single Top Production using Likelihood Functions with 3.2 fb^{-1} of **Data**", CDF Note 9695 (2009).

[19] Florencia **Canelli**, Bruno **Casal** Laraña, Peter Dong, Bernd Stelzer, Rainer Wallny "Measurement of Single Top Quark Production in 3.2 /fb of CDF Data Using a Matrix Element Technique", CDF Note 9703 (2009).

[20] D. Hirschbuehl, J. Lueck, Th. Muller, **A.** Papaikonomou, W. Wagner, "Search for single top-quark production with neural networks using 3.2 fb^{-1}", CDF Note 9684 (2009).

[21] B. **Alvarez** et al., "Search for Single Top Quark Production using Boosted Decision Trees i n 3.2 fb^{-1} of CDF Data", CDF Note 9686 (2009).

[22] **A.** Apresyan,D. Bortoletto, F. Margaroli, K. Potamianos"Measurement of the single top production cross section in the met plus |ets sample", CDF Note 9589 (2009).

[23] K. Nakamura and S. Kim, "Single Top Quark s-channel Search Update with3.2 fb^{-1} data", CDF Note 9702 (2009).

[24] B. **Alvarez** et al., Combination of the Single-Top Searches with 3.2 fb^{-1}, CDF Note 9706.

[25] B. W. **Harris**, E. Laenen, L. Phaf, *Z.* Sullivan and S. Weinzierl, Phys. Rev. D 66, 054024 (2002) [arXiv.hep-ph/0207055].

[26] N. Kidonakis, Phys. Rev. D 74, 114012 (2006) [arXiv.hep-ph/0609287].

[27] H. Stadie, W. Wagner, H. Wenzel, and Th. Muller, "Vxprim in Run II", CDF Note 6047

[28] T. Junk, "Sensitivity, Exclusion and Discovery with Small Signals, Large Backgrounds, and Large Systematics", CDF Note 8128.

[29] MadGraph/MadEvent v4. The New Web Generation Johan Alwall, et al, JHEP 0709.028,2007, arXiv.0706.2334.

[30] W helicity in top decay results are summarized at http://www-cdf.fnal.gov/physics/new/top/public_tprop.html

[31] J. Lück, Diplom thesis, University of Karlsruhe, FERMILAB- MASTERS-2006-01 (2006).

[32] H. L. Lai, J. Huston, S. Kuhlmann, J. Morfin, F. Olness. J.F.Owens, J. Pumplin, W. K. Tung "Global QC Analysis of Parton Structure of the Nucleon. CTEQ5 Parton Distributions" [arXiv.hep-ph/9903282]

[33] D. Hare, E. Halkiadakis, T. Spreitzer, "Electron ID Efficiency and Scale Factor for Winter 2007 Analuses", CDF Note 8614.

[34] F. Garberson, J.R. Incandela, C. Neu,"Sec$V$tx B-Tag Efficiency Measurement Using Muon Transverse Momentum for 1.2 f b^{-1} Analyses", CDF Note 8640.

[35] Franklin, Grinstein, Guimarães da Costa, Lannon, Schwarz, Taffard, Zaw, "Heavy-Flavor Content of the W+Jets Sample", CDF Note 8765.

[36] Franklin, Grinstein, Guimarães da Costa, Sherman, Zaw,"Calibration of Heavy-Flavor Production in QCD Data", CDF Note 8768.

[37] Dante Amidei, Clark Cully, Peter Dong, Sebastian Grinstein, Veronica Sorin, Bernd Stelzer, Rainer Wallny, "Calibration of Heavy-Flavor Production in W+1 Jet Data", CDF Note 9187

[38] T. Aaltonen,et al., "First Measurement of W Boson Production in Association with a Single Charm Quark in p$\bar{p}$ Collisions at $^p\bar{s}$/ 1.96TeV", Phys. Rev. Lett. 100, 091803 (2008)

[39] Young-Kee Kim, Un-Ki Yang,"Unitial state gluon radiation studies on Drell-Yan data for top-pair production in hadron collider", CDF Note 6804

[40] T. S|ostrand,et al., "High-Energy-Physics Event Generation with PYTHIA 6.1" (2001) [arXiv.hep-ph/0010017]

149

[41] Franklin, Grinstein, Guimarães da Costa, Sherman, Zaw. "Calibration of Heavy-Flavor Production in QCD Data", CDF Note 8768

[42] Sarah Budd, Top Junk, "SECVTX Mistag Parameterization for Winter 2006", CDF Note 8072

[43] Thomas Junk, "Frequentist Exclusion and Discovery of Signals in Combined Searches with Large Systematic Uncertianties on the Background" CDF Note 6525

[44] Thomas Junk, "Sensitibity, Exclusion and Discovery with Small Signals, Large Backgrounds, and Large Systematic Uncertainties" CDF Note 8128

[45] C. Blocker, J. Conway, L. Demortier, J. Heinrich, T, Junk, L. Lyons, G. Punzi "Simple Facts about P-$Value$"

[46] J. Heinrich, C. Blocker, J. Conway, L. Demortier, L. Lyons, G. Punzi, P. Sinervo. "Interval estimation in the presence of nuisance parameters. 1. Bayesian approach" CDF Note 7117

[47] Joel Heinrich, "Bayesian limit software. multi-channel with correlated backgrounds and efficiencies" CDF Note 7587

[48] J. Adelman et al. "Determination of the Jet Energy Scale at the Collider Detector at Fermilab" [arXiv.hep-ph/0510047]

[49] D. Acosta et al. "A First Look at the CLC Luminosity Measurements" CDF Note 6052

[50] S. Jindariani et al. "Luminosity Uncertainty for Run 2 up until August 2004" CDF Note 7446

[51] Nate Goldschmidt, Ken Bloom, David Gerdes, Dan Amidei. "Measurement of the Helicity of W Bosons Produced in Top-Quark Decay" CDF Note 6617

[52] Christopher Neu, The CDF Collaboration, "CDF b-tagging. Efficiency and Mistag Measurement" CDF Note 8102

[53] Peter Dong, Bernd Stelzer, "Reduction of QCD background in lepton + jets events" CDF Note 8295

[54] J. Charles et al. "CP $Violation$ and the CKM Matrix.Assessing the Impact of the Asymmetric B Factoreis" [arXiv.hep-ph/0406184]

[55] A. Hocker, H. Lacker, S. Laplace, F. Le Diberder, "A New Approach to a Global Fit of the CKM Matrix" [arXiv.hep-ph/0104062]

150